Combined Tension-Torsion Loading of Braided Composite Structures

Abbas Armanfard

A THESIS SUBMITTED TO THE FACULTY OF GRADUATE STUDIES IN PARTIAL FULFILLMENT OF THE REQUIREMENTS FOR THE DEGREE OF MASTER OF SCIENCE

Graduate Program in Mechanical Engineering
York University
Toronto, Ontario

August 2020

Abstract

Braided composites are a class of composite materials. They feature an inter-woven structure that improves structural stability and damage tolerance. Presently, braided composites under tension and torsion loading have been studied individually. Mechanical behaviour of braided composites under combined tension-torsion loading is common, yet no studies have explored this effect. In this study, mechanical properties of carbon fibre, fibreglass and Aramid 2D tubular braided composites (TBCs) were assessed and compared under coupled tension-torsion loading. Failure mechanism of braids was investigated by the plane stress theory. A contact-free three-dimensional digital image correlation (3D DIC) technique was used to derive detailed and continuous strain maps and understand buckling behaviour of TBCs. Benefitting from this research experiment, combined loading as a common and critical loading condition can be analyzed more realistically and accurately in designing elements out of braided composites to prevent structural failures.

Acknowledgements

First of all, I would like to appreciate my supervisor, Dr. Garrett Melenka, who has diligently guided me in the last two years. The door to his office was always open whenever I faced any challenge in my research. He immensely helped me to develop my research and technical skills to build my career foundation. His thorough knowledge in his research field has been a massive power to run our research group.

Secondly, I would like to thank my other committee members, Dr. Leung and Dr. Boalye-Yiadom, for their guidance and valuable suggestions.

Thirdly, I would like to show my appreciation to my wonderful lab mates. They supported my research progress and facilitated amazing teamwork together.

In the end, I would like to dedicate this thesis to my wonderful parents, who have sacrificed and invested 25 years of their lives for me to grow, learn and eventually teach. I would like to thank my brother and sisters for their consistent encouragement in the last two years.

Table of Contents

List of Tables

List of Figures

List of Abbreviations

AIAC	Aerospace Industries Association of Canada
2D	Two Dimensional
3D	Three Dimensional
DIC	Digital Image Correlation
2D DIC	Two Dimensional Digital Image Correlation
3D DIC	Three Dimensional Digital Image Correlation
TBC	Tubular Braided Composite
TBCs	Tubular Braided Composites
ROI	Region of Interest
FOV	Field of View
Std Dev	Standard Deviation
CT	Computed Tomography
μCT	micro Computed Tomography

List of Symbols

D_o	Outer diameter
D_i	Inner diameter
m_f	Fibre mass
m_m	Matrix mass
m_b	Braided composite mass
V_f	Fibre volume
V_m	Matrix volume
ρ_f	Fibre density
ρ_m	Matrix density
v_F	Fibre volume fraction
ρ	Density
σ_{UTS}	Ultimate Tensile Strength
θ_b	Braid angle
A	Cross-sectional area
W_y	Yarn width
ϵ_{xx}	Transverse strain
ϵ_{yy}	Longitudinal strain
σ_{yy}	Axial stress
σ_z	Stress in z-direction
τ_{zx}	Shear stress perpendicular to z and along x-direction
τ_{zy}	Shear stress perpendicular to z and along y-direction
σ_y	longitudinal stress in y-direction
τ_{xy}	Shear stress perpendicular to x and along y-direction
θ_{P_1}	First principal plane angle
θ_{P_2}	Second principal plane angle
σ_1	Principal stress in direction 1
σ_2	Principal stress in direction 2
σ_x	Transverse stress
T	Torque
θ_T	Torsional angle
τ_{max}	Maximum shear stress
u	Displacement vector field in x-direction
v	Displacement vector field in y-direction
ϵ_{xy}	Shear strain perpendicular to x and along y-direction
ϵ_{yx}	Shear strain perpendicular to y and along x-direction

$\theta_{P_{max}}$	Maximum principal plane angle
T_{max}	Maximum torque

Chapter 1 Introduction

1.1 Motivation

According to the Aerospace Industries Association of Canada (AIAC), there are more than twenty companies in Canada, including Airbus and Bombardier, that are investing in composite bonding, ducting, fairings, and fabrications [1]. High strength to weight ratio is the main feature of composite materials that have qualified them to be extensively used in industries that require high-performance elements, such as aerospace [2]–[4]. The Boeing 787 has saved approximately 20% in weight compared to conventional aluminum airframes by having an airframe design comprising about 50% composite materials [5]. Over the years, however, it is realized that conventional composite laminates have several limitations. They suffer from relatively low toughness, delamination, high cost and time-consuming laminate manufacturing process [6], [7]. Other composite manufacturing methods are required to overcome these limitations.

On the other hand, braided composites have improved qualities that prevail over technical challenges created by conventional laminated composites. Braided composites consist of continuously interwoven fibres in a resin epoxy matrix. Braided preforms are produced with an automated braiding process using two-dimensional (2D) and three-dimensional (3D) braiding machines such as maypole, rotary and cartesian braiders. The interwoven nature of braided composites results in damage tolerance and structural stability [2], [8]. Utilizing lightweight fibres and benefiting from braiding technology as a time and cost-efficient manufacturing method reduces carbon dioxide emissions and answers the increasing demand for high-performance structures such as jet engine stator vanes, fan blades and shafts [2], [9]–[13].

Since braided composites are generally manufactured in tubular cross-section to produce axisymmetric parts, the evaluation of braided composites in the tubular configuration is required under loading [14], [15]. 2D braid preforms are formed from the interlacement of fibre tows around a mandrel using Maypole or radial braiding machines [9], [16]. Braids are formed by different repeating patterns of yarns. These patterns are called braiding patterns. Common braid patterns are diamond (1/1), regular (2/2) and Hercules (3/3) [16], [17]. Regular (2/2) braiding patterns are the most common pattern used for manufacturing braids [18]. Various types of fibres have been utilized for manufacturing braided composites [2]. The most common fibres for producing braided composites are carbon fibre, fibreglass and Aramid [19].

Braided composites are becoming more widely adopted for industrial applications; therefore, understanding their mechanical behaviour under various kinds of stress states is crucial to avoid premature failure [14]. Independent studies of 2D tubular braided composites (TBCs) under tension and torsion loadings have been investigated by several researchers [7], [8], [20]–[24]. Tension and torsion loadings are typical loads that a braided composite part experiences in operation. However, combined tension/torsion loading is another type of loading, which is also common in braided composites applications such as fan blades, yet few studies have explored this effect.

1.2 Thesis objectives

The objective of this thesis is to evaluate the mechanical behaviour of carbon fibre, fibreglass and Aramid TBCs under combined tension/torsion loading experiments. Braided preforms with regular (2/2) braiding patterns, as the most common braiding pattern, were used for all three types of braids. The three-dimensional digital image correlation (3D DIC) technique is used to investigate elastic and failure strain fields and buckling behaviour of TBCs. More importantly, the failure mechanism of braids is investigated by the plane stress theory of mechanics of material. Moreover, stiffness magnitudes are compared for different braids with different types of fibre.

For designing a combined loading experiment, mechanical properties of test specimens in tensile loading is required. Therefore, prior to conducting combined loading experiments, similar carbon fibre, fibreglass and Aramid samples of TBCs are tested in static tensile loading experiments. Tensile loading experiment on different fibres is also unique; there is no similar study in the literature focusing on comparing TBCs manufactured using different fibres in tensile loading. Therefore, the study on TBCs in tension is completed comprehensively in a separate chapter to fill the mentioned gap in the literature. To study the tensile loading of TBCs, a 3D DIC measurement technique was used. By analyzing the 3D DIC results, elastic and failure strain fields, elastic mechanical constants, necking process, failure modes and manufacturing consistency of carbon fibre, fibreglass and Aramid braids are studied and compared.

The experimental results and discussions presented in this thesis can be used for evaluating numerical and analytical models for predicting carbon fibre, fibreglass and Aramid TBCs mechanical behaviour under tension and combine tension/torsion loadings.

1.3 Thesis outline

This thesis is organized in five chapters. An introduction to braided composites, braids common terminology, common materials used in braids is provided in Chapter 2. Moreover, in Chapter 2, a literature review of deformation measurement techniques on braided composites and a review of studies that have performed mechanical tests on TBCs is included. Chapter 3 presents the study on carbon fibre, fibreglass and Aramid TBCs in the tensile loading experiment. In this chapter, the manufacturing procedure of TBC used for this thesis experiments is fully elaborated. Chapter 4 focuses on a combined loading experiment on carbon fibre, fibreglass and Aramid TBCs. A summary of results and a future work for mechanical testing of TBCs is presented in Chapter 5.

Chapter 2 Background and literature review

2.1 Introduction to composite materials

Development in technology relies on advances in materials. Without adequate materials that can bear intense loading conditions, most advanced turbine and aircraft designs would not be manufactured and operating now. Composite materials have been a gigantic step toward optimizing material for the demands of industries for high-performance materials. Egyptians began the significant use of composites by using bamboo shoots as a reinforcement of mud walls in 1500 B.C. By reinforcing resins with glass, a new generation of the composite application was introduced in the 1930s. Boat and aircraft are example products of the glass composites in the 1930s [25].

Composite materials are the combination of two or more materials that, when combined, have improved mechanical properties than the individual constituents. The resulting composite material usually has a phase named reinforcement, which may be in the form of fibres, particles or flakes and a phase named matrix in which reinforcements are embedded. Figure 2-1 simply shows a composite structure and its matrix and reinforcement phases. Concrete reinforced with steel bars and epoxy reinforced with carbon fibre are some common examples of composite structures [26], [27]. Properties such as strength, stiffness, weight, fatigue life, corrosion resistance, thermal conductivity and thermal insulation can be enhanced by producing composite materials [28].

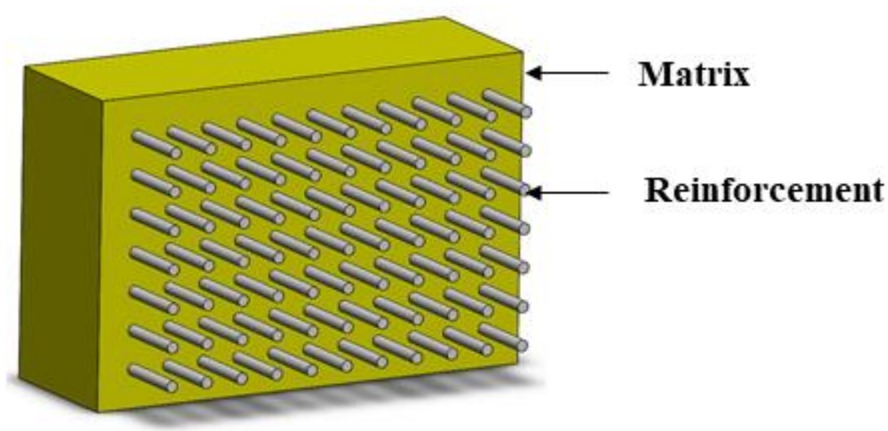

Figure 2-1: Illustration of a composite material structure. The constituents of the composite structure are matrix and reinforcement.

Composites materials are utilized for their high strength to weight ratio in industries that require high-performance components [2]–[4]. Aerospace, military, automotive, and marine are example industries that widely use the composites for their components [29]. However, conventional composite laminates (Figure 2-2) suffer from relatively low toughness and delamination due to its layer by layer structure [7]. Furthermore, the process of laminate manufacturing is costly and time-consuming [30]. On the other hand, textile composite, as a category of composite materials, are more attractive than conventional composites. Textile composite is a category of composite materials that combines a textile structure into a resin matrix. Textile composites have an interwoven structure that results through the thickness reinforcement. Compared to conventional composite laminates, textile composites have higher production rates, higher strength to weight ratio, through-thickness reinforcement, structural stability, and damage tolerance [6], [30], [31]. Because of these advantages, textile composites are becoming more common in aerospace, sporting, automotive and marine industries [30], [32]–[34]. Textiles have interwoven structures with yarns perpendicular to each other. An example illustration of a textile structure is shown in Figure 2-3. Textile composites, according to their fabrication methods, are grouped into woven, knitted stitch-bonded, non-woven and braided composites [7].

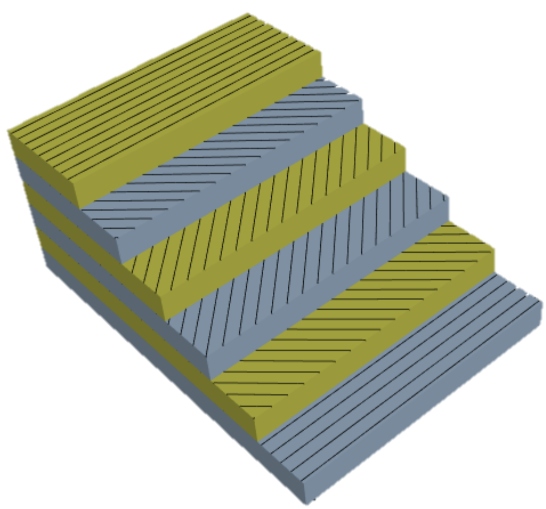

Figure 2-2: demonstration of a laminate with six layers oriented in different angles.

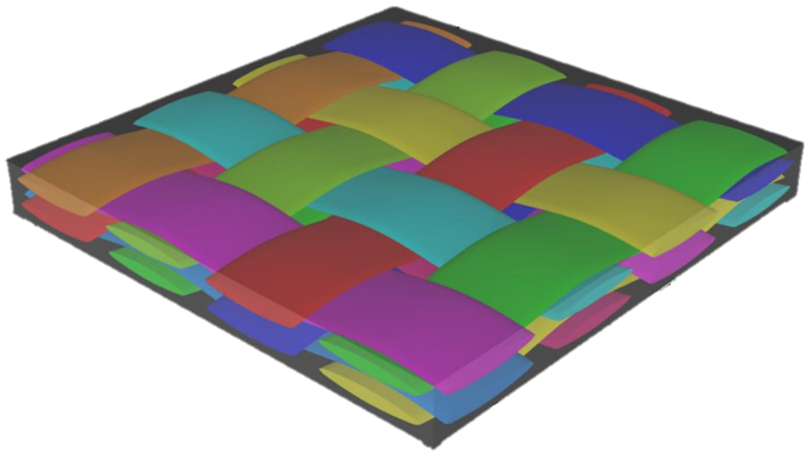

Figure 2-3: An illustration of a textile material. Textiles have interwoven structures with yarns perpendicular to each other.

Braided composites, as a category of textile composites, are a composition of continuously interlaced fibres in a resin epoxy matrix. The interlaced fibre makes a braided preform and is produced using a braiding. In Figure 2-4, the schematic simply illustrates how a braided preform is made using a braiding machine. A braid preform is shown from two different views in Figure 2-5. The interwoven nature of braided composites results in damage tolerance and structural stability [2], [8]. Utilizing lightweight fibres and benefiting from braiding technology as a time and cost-efficient manufacturing method reduces carbon dioxide emissions and answers the increasing demand for high-performance structures such as jet engine stator vanes, fan blades and shafts [2], [9]–[13]. Braided composites are getting widespread applications in industries; therefore, understanding their mechanical behaviour under various kinds of stress states is crucial to avoid premature failures [14]. This chapter initially focuses on defining braided composites and explaining how these composites are manufactured in section 2.2. Then, in section 2.32.3, there is a literature review on publications that have performed mechanical tests on braided composite. Literature that is discussed in sections 2.4 includes studies on tubular braided composites (TBCs) that experienced tensile and torsion loadings and excludes studies on all other types of loading on TBCs. In section 2.4, deformation measurement techniques that have been utilized for assessing tubular braided composites under mechanical loading are discussed. Finally, in section 2.5, the proposed case study for this research work is represented in detail. The literature presented in this chapter is required to support the proposed case study for this thesis.

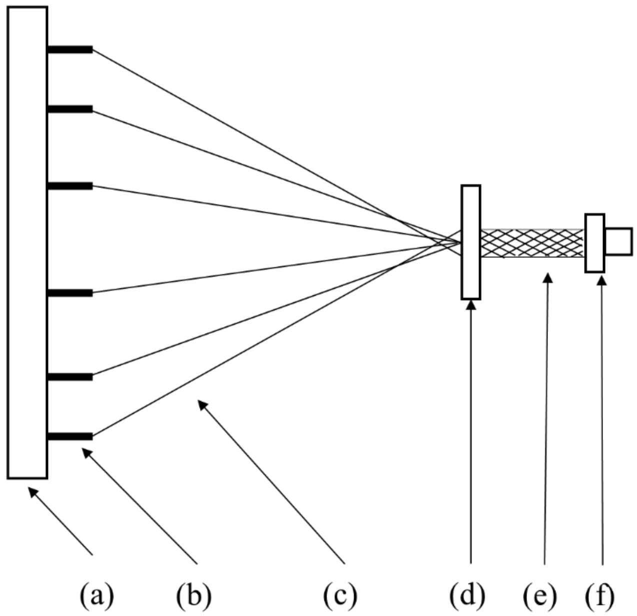

Figure 2-4: A schematic of a braiding machine showing how the braided preform is produced. Components of the machine are a) trach plate, b) yarn carrier, c) yarn, d) forming plate, e) produced braid preform, and f) take-up mechanism of the braider.

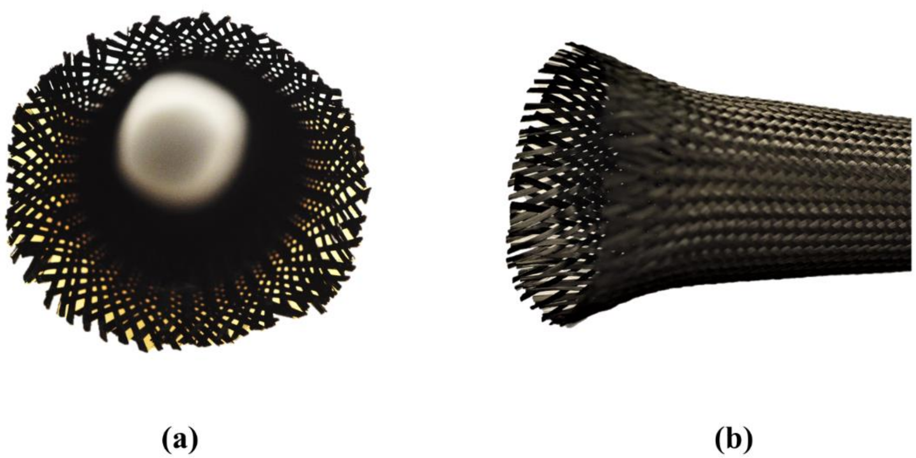

Figure 2-5: Sample braid preform. (a) shows the front and inner view of the braided preform and (b) shows the side view of the same braid preform shown in (a).

2.2 Braided composite

2.2.1 What are braided composites

Braided composites (Figure 2-6) are a category of composites which features an interwoven structure [2]. Braided composites belong to the family of textile composites [35]. Textile composites comprise textile structures impregnated by a resin matrix. There have been several studies on braided composites in the literature. Following influential works done by Ko and Pastore, such as their contributions to handbooks in braiding [36], [37], composite braids became a subject to undergo an intense examination. Akkerman, van Ravenhorst, Du and Popper were mainly working on the kinematics of the braiding process [38], [39]. Alternatively, Hamanda and Nakai[40], [41], [50]–[52], [42]–[49], Potluri [6], [31], [53]–[57] and several others [19], [58]–[63] worked on mechanics of braided composites.

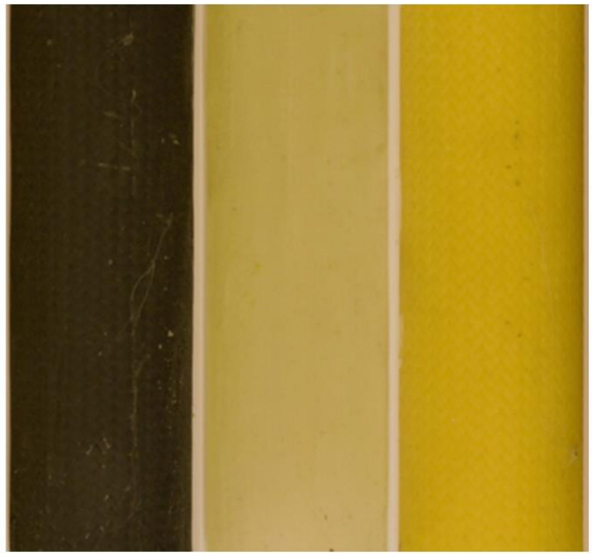

Figure 2-6: sample representation of three manufactured braided composites out of (a) carbon fibre, (b) fibreglass and (c) Kevlar braid preforms.

Braided composites have several unique features. They have a high rate of production, and due to the interlacement of braid yarns, they have structural stability and damage tolerance. These features distinguish braided composites from conventional composites [64]. Due to specific toughness and strength, braided composites have a variety of applications. They are used for manufacturing structural components, sports equipment, aircraft fan blades, air ducts, over braided fuel lines and reinforced automobile shafts[9], [65]. Additionally, their application has been investigated for biomedical objectives such as orthopedic treatment[66] and prosthetic intervertebral disc [67], [68].

Braid preforms (Figure 2-7) are produced with an automated braiding process using two-dimensional (2D) and three-dimensional (3D) braiding machines such as maypole, rotary and cartesian braiders. Braids can be manufactured in flat, tubular and three-dimensional shapes [69]. Since braided composites are generally manufactured in tubular cross-section to produce axisymmetric parts, the evaluation of braided composites in the tubular configuration is required under loading [14], [15]. Braid preforms are either biaxial- bias interlacement of yarns or triaxial braid with a set of introduced axial yarns [70]. Depending on braid manufacturing methods, the structures of braid preforms are either two- (2D) or three dimensional (3D) [71].

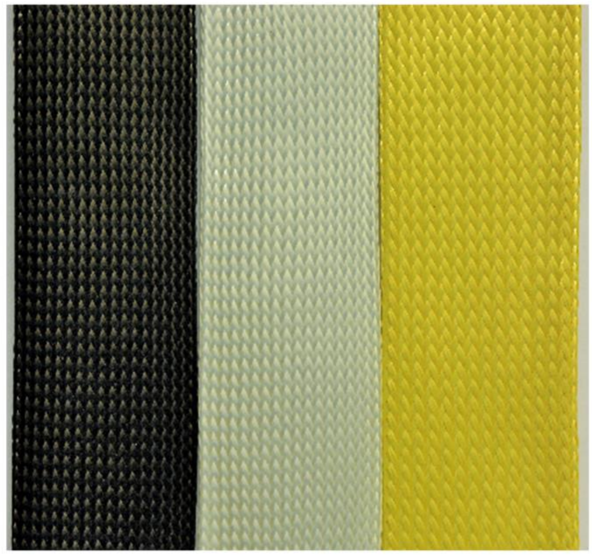

Figure 2-7: sample representation of (a) carbon fibre, (b) fibreglass and (c) Kevlar braid preforms.

2D braid preforms are produced from the interlacement of yarns around a mandrel with Maypole or radial braiding machines [9], [16], [72]. 2D braids can be produced in flat and tubular forms [2]. 2D braided composites are manufactured in two forms of closed mesh and open meshed structures. To use 2D braids in applications that require high stiffness and strength such as pressure vessels and sports equipment, 2D braids require closed mesh structures since they have better elastic properties than open meshed braids [19], [73].

3D braided composited are grouped into different categories such as solid, two-step, four-step and multistep [74], [75] and are described by interplay or through-the-thickness interlacing [9]. There are significant differences between 2D and 3D braided composites structures. 2D braided composites are typical for applications that require low stiffness as well as structural confinement and pressure vessels. However, 3D braided composites are designed for high strength and stiffness purposes; for example, near net-shaped I beams [2]. This thesis is focused on evaluating 2D braided composites.

2.2.2 Braids common terminology

Braided composites are manufactured from preforms with undulating yarns impregnated in a resin matrix. Yarn is a bundle of fibres. Exaggerated fibre and yarn configuration are shown in Figure 2-8. Braids are formed by different repeating patterns of yarns. These patterns are called braiding patterns. Common braid patterns are diamond (1/1), regular (2/2) and Hercules (3/3) [16], [17] and are shown in Figure 2-8 (a)-(c) respectively. The yarns in the diamond pattern have one-over-one overlap, in the regular pattern have two-over-two overlaps, and in Hercules pattern have three-over-three overlaps [16]. Regular (2/2) pattern is the most common pattern used for manufacturing braids and is similar to a twill weave, though, in bias direction [18]

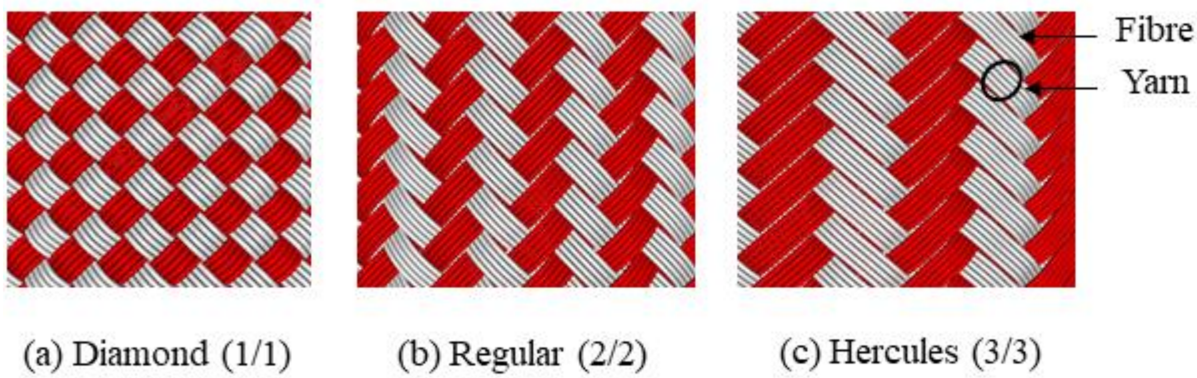

Figure 2-8: Illustration of (a) diamond, (b) regular and (c) Hercules braiding patterns. (i) shows an exaggerated fibre of braid yarn and (ii) shows the yarn of braid, which is a bundle of fibre filament.

Figure 2-9 represents the braid unit cell for an example regular (2/2) braid. The braid's unit cell shows the architecture of the entire composite which is a repeating pattern in a braided structure [9], [76]. Braid unit cell has several geometrical properties that affect the mechanical properties of the braid structure. Braid angle, θ_b, shown in Figure 2-9, is the angle between longitudinal and fibre direction of braid. Braid angle is a parameter that significantly affects the mechanical properties of braided composites [77]. Yarn width, W_y, shown in Figure 2-9, is a geometric factor that affects the geometry of braided composite [78]. Braid angle and yarn width are two geometrical parameters of braid that are commonly measured and reported in studies on braided composites [8], [14], [79], [80].

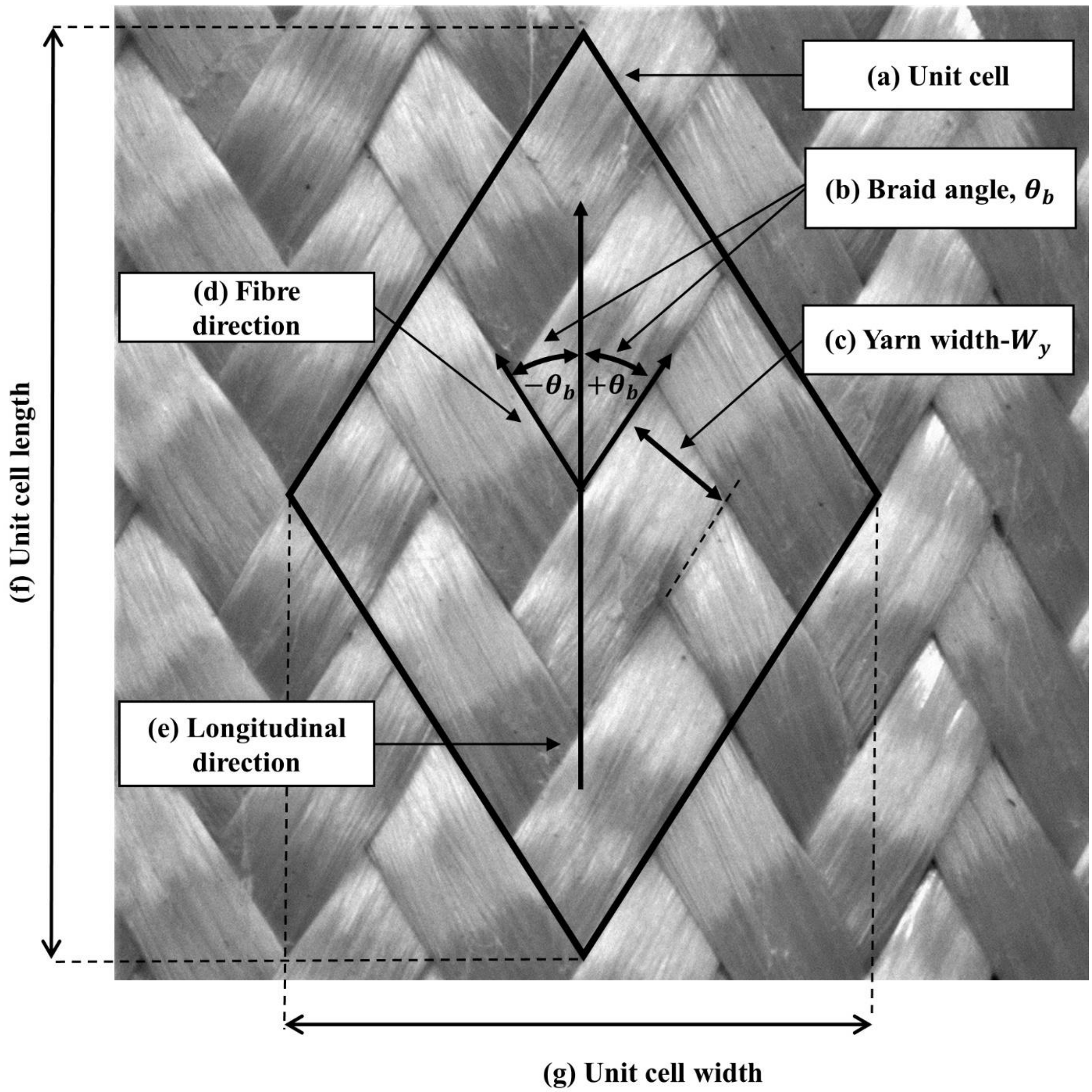

Figure 2-9: Schematic illustration of braid's unit cell and its geometrical parameters. This figure shows a) unit cell of a regular braid, b) braid angle, c) yarn width, d) fibre direction, e) longitudinal direction of braid, f) unit cell length and g) unit cell width.

2.2.3 Braid materials

Fibres are used to manufacture braided composite. The advantages of fibres are that they are strong, stiff, and light compared to other customary materials. On the other hand, fibres have different drawbacks. They can be brittle, have surface defects, and degrade over time due to improper storing techniques. Hence, fibres are impregnated by resins to overcome their weakness and improve their properties [2]. Therefore, braided composites are a combination of fibres and resins. Different types of fibres have been used for braided composite manufacturing [2]. The most common fibres for manufacturing braided composites are carbon fibre, fibreglass and Aramid [19].

Carbon fibres are developed from different precursors such as polyacrylonitrile as one of the most common ones. Carbon fibres have superior properties; they have high modulus (200–500 GPa), high strength (3–7 GPa), and low density (1.75–2.00 g/cm^3) [81]. Due to their exceptionally high specific strength and stiffness, they are widely used in the aerospace industry, where high strength and light structures are required [2]. The use of carbon fibre is getting more common in other industries, such as automotive, as they are getting less expensive [81]. Furthermore, carbon fibre can endure very high temperatures. When carbon fibre is used as a composite reinforcement, composite structure performs well in high temperatures unless the matrix melts and fails [2].

Fibreglass is widely used in composites structures that are designed for various small- and large-scale applications. Fibreglass composites give high strength to weight ratio and good environmental resistance. The glass fibre composites are good electrical insulators, and their fabrication is easy and low in cost relative to other fibre composites [2]. There are several types of glass fibres ,however, the most common one is E-glass (an alumino-borosilicate glass with a mass fraction of alkali ≤ 1%), which is used in all fields of industry and everyday life [82]. E-glass fibre has a modulus of 72 GPa, strength of 3.5 GPa and density between 2.54 g/cm^3 and 2.60 g/cm^3 [2].

Aramid fibres have high tenacity and modulus of elasticity. Furthermore, due to para-phenylene terephthalamide chemical structure, they are thermally resistant, non-flammable and also dimensionally stable[83]. Aramid fibres are used in various applications such as flak jackets [84], aerospace, marine cordage and marine hull reinforcement [83]. Aramid fibre applications are also investigated for concrete reinforcement [85], rebar design [86] and biomedical purposes [87]. Kevlar 49 is a high modulus Aramid fibre that has a modulus between 112 GPa and 138 GPa, strength of 3.6 GPa and density of 1.44 g/cm^3 [2]. Table 2-1 demonstrates the properties of three types of regular (2/2) 2D biaxial carbon fibre, fibreglass and Aramid braided preforms used in this project. Table 2-2

Table 2-1: Typical reported properties of braid preforms used in this research project [2], [88]

	Tensile Modulus $\boldsymbol{E_t}$ (GPa)	Tensile Strength $\boldsymbol{\sigma_t}$ (GPa)	Density $\boldsymbol{\rho}$ (g/cm^3)	Yield (kg/m)	Denier (g/9000m)	Fabric Weight (g/m^2)
Carbon fibre	236.14 ± 4.5	4.3 ± 0.1	1.75	24.7 ± 0.7	363953.1	254.3 ± 6.8
Fibreglass	72	3.5	2.57 ± 0.3	26.5 ± 0.7	505414.2	352.6 ± 10.2
Aramid (Kevlar 49)	125 ± 13	3.6	1.44	18.7	481779.7	336

Fibres are held and loaded through matrices. Matrices reinforce fibres and preserve them from the environment and damages. Different types of matrices are utilized for composites, such as polymers, metals, or ceramics. Polymer matrices are commonly used in braided composites and are either thermoset resin or thermoplastic resin [2].

Thermoset resins are polymers cured with a chemical reaction. These resins are formed permanently so that they either degrade or burn off as the temperature increases without any melting process. Since thermosets such as epoxies have relatively low viscosity, they are the matrix target for manufacturing braided composites, because fibres in braids need to be thoroughly impregnated by resin. Table 2-2 provides mechanical properties of a thermoset resin used in this study to manufacture braided composites. Unlike thermoset matrices that generate covalent bonding, thermoplastic matrices form relatively weak intermolecular forces; therefore, thermoplastics are easily softened when the heat is applied to them. They are suitable only for operations that are cooler than this melting temperature. Thermoplastic polymers have applications where injection molding and extrusion processes are required. Resin selection for composites is mainly according to the final desired application of the composite. The environment and operating temperature of composite must also be measured when choosing the resin for manufacturing [2].

Table 2-2. Mechanical properties for cured resin-hardener (2000 series resin with 2060 hardener, FibreGlast)

Mechanical Properties	Reported data
Tensile Modulus $\boldsymbol{E_t}$ (GPa)	2.9
Tensile Strength $\boldsymbol{\sigma_t}$ (MPa)	67.7
Density $\boldsymbol{\rho}$ (g/cm^3)	1.11

2.2.4 Manufacturing of braided composites

One of the challenges that limit the applications of composites is their inconsistent mechanical properties due to the impregnation process. During manufacturing composite materials, non-homogenous impregnation of fibres causes voids in the structure that affects the mechanical characteristics of the manufactured part. Fibre impregnation for manufacturing braided composites is as crucial as producing braid preform [9]. There are different methods for manufacturing braided composites.

2.2.4.1 Manual impregnation

The easiest and the cheapest technique for impregnating a braided preform is manually by doing brushing or messaging resin into preform [89], [90]. For example, researchers in [16] and [82] massaged and in [7] and [21] brushed resin for the impregnation purpose. For manual impregnation, a resin with longtime pot life is required to prevent premature cure. This impregnation technique highly depends on the operator's skill level for applying the resin into the preform [9].

2.2.4.2 Shrink tape wrapping

One of the techniques to manufacture composite tubes is the shrink tape wrapping technique [91]. Several researchers have used this technique to produce composite [92]–[94] and braided composites [95], [96]. This technique gives improved interfacial bonding between composite layers [92], high fibre volume fraction, low void fraction and better surface finish [95], [96]. For manufacturing braided composite using shrink tape, when the preform is impregnated with resin, the tape is wrapped on its surface under sufficient stress. This stress helps to achieve high fibre volume and low void content [95]. When the tape is wrapped, heat is applied to the taped part. Due to shrinkage of tape, stress is applied to the composite part, extra resin penetrates, and better bonding between composite components is achieved [92].

2.2.4.3 Resin Transfer Molding (RTM) and Vacuum Assisted RTM (VARTM)

To increase the consistency in mechanical properties of braided composites, impregnating braid preforms can get automated by using the resin transfer molding (RTM) technique. This technique allows for high fibre volume products with very low void content. Using RTM, products can be manufactured to the near net shape and with a homogenous structure. The products need minor machining; therefore, the end cost of composite products is decreased using RTM procedure [9].

For producing composites using the RTM technique, a braided preform is placed in a mold or tool. The whole mold-preform assembly with the resin is heated to a proper temperature for the resin to minimize its viscosity. Then, the resin is transferred to preform by applying pressure.

Different types of frames, such as keel and window frames, are manufactured using this method by braided composites [9]. Uozumi *et al* [97] manufactured carbon fibre braided composites for I-beam frames and panels using the RTM technique to investigate their mechanical performance and production cost. They argued that the mechanical properties of their manufactured composites were better than similar products made with aluminum. Moreover, they stated that the end cost of braiding and RTM process for making the products cost about 34% less than manual hand-lay-up/autoclave process.

Vacuum-assisted resin transfer molding (VARTM) is another impregnation technique used in several studies for braided composite manufacturing [6], [31], [70], [98]. This technique is suitable for manufacturing large and complex shape composites. VARTM has a low cost for mass production and produces composites with high fibre volume fractions relative to the hand-lay-up technique [99]. For the VARTM technique, the dry braid preform is placed in a mold or tool, and then low viscous resin is transferred to braid using a vacuum system. This technique produces good quality surface finish composites [9].

2.3 Mechanical tests on braided composites

Industries are extensively turning into the use of braided composites; therefore, understanding their mechanical response under different kinds of stress states is necessary to avoid failures [14]. 2D TBCs in tension and torsion loadings have been investigated by several researchers [7], [8], [20], [21], [23], [24]. For example, Harte and Fleck investigated fibreglass TBCs to understand and model their deformation and fracture responses in various braiding angles under tensile loading [7]. In another work by Harte and Fleck, they studied a regular fibreglass TBC to explore the failure modes for different braid angles under various types of loadings with a minor focus on combined tension/torsion loading [21]. Melenka *et al.* examined the effect of braid angle and braid pattern on the mechanical properties of Aramid TBCs under tension and torsion loadings [8]. Presently, 2D TBCs under tension and torsion loading have been studied individually. There are studies that have examined other types of composites under simultaneous tension and torsion loading [100], [101]. Yu *et al*. experimentally explored a needled composite under coupled tension-torsion loading [100]. Amijima *et al.* performed static and fatigue mechanical tests for woven glass fabric composite under biaxial tension-torsion loading [101]. Braided composite components frequently experience combined tension-torsion loading while in operation, for example, over braided fan blades under airflow loads in various directions. However, no studies have investigated the mechanical properties of braids due to the effect of combined loading.

2.4 Deformation measurement technique for braided composites

Deformation measurements of braided composites under loading have been performed using different techniques. Many researchers have used conventional techniques such as strain gauges and extensometers for evaluating deformations [6], [7], [21], [100]. These techniques are limited to measure the deformation of specific locations on the specimen and require direct contact with samples. As mentioned earlier in this chapter, braided composites have an interwoven structure that is inhomogeneous due to the interlacement of yarns. Hence, to accurately measure braided composite deformation under loading, the measurement technique should be independent of the material structure and its surface finish. Recently scholars [98], [102]–[105] have turned into the use of digital image correlation (DIC) as a contact-free full-field measurement technique that does not have the limitation regarding material type and specimen size [106]. This technique is called either 2D DIC if the measurement is performed using a single camera or 3D DIC if multiple cameras do the imaging for measurements. 2D DIC is applicable for full-field strain measurements for flat specimens [107], [108]. For TBCs, 3D DIC is preferred as the braids have wavy and curved structures; therefore, in-plane and out of plane displacement measurement are required [14]. 3D DIC measurement technique is preferred over conventional discrete measurement methods such as strain gauges since it can process strains over multiple unit cells [8], [20]. Leung *et al.* used 3D DIC to see how nominal diameter and braid angle changes during tensile test stroke by examining full-field unit cell strain and surface reconstruction of Aramid TBCs [20]. Melenka *et al.* thoroughly used the 3D DIC technique to examine the effect of braid angle and pattern on the mechanical properties of Aramid TBCs [8]. Bruni-Bossio *et al*. used the 3D DIC technique to study the effect of braid angle on tensile properties of TBCs manufactured by cellulose fibres with bio-based resins [24]. 3D DIC technique is also used for studying TBCs under bending. Can *et al.* conducted a novel study on flexural properties of natural fibre TBCs under a three-point bending load. They used 3D DIC for strain measurements. The following section briefly describes the method of digital image correlation.

2.4.1 Digital image correlation (DIC)

Digital image correlation (DIC) is an optical full-field displacement measurement technique. This technique uses random contrast patterns on the specimen to measure deformation. The measurement setup of the DIC technique is relatively simple. It requires CCD (charged coupled device) camera, a computer to recorded and process the digital images, and a light source if the ambient light is not enough. Depending on the number of cameras, DIC can have two configurations: 2D DIC, which goes for DIC setup with a single camera that allows for in-plane displacement measurement, and 3D DIC, which is the setup including two cameras having a stereo angle that measures in-plane and out of plane displacements. Figure 2-10 illustrates a complete 3D DIC experiment configuration, including a test specimen under loading, two CCD cameras, light sources, and a DIC processing computer.

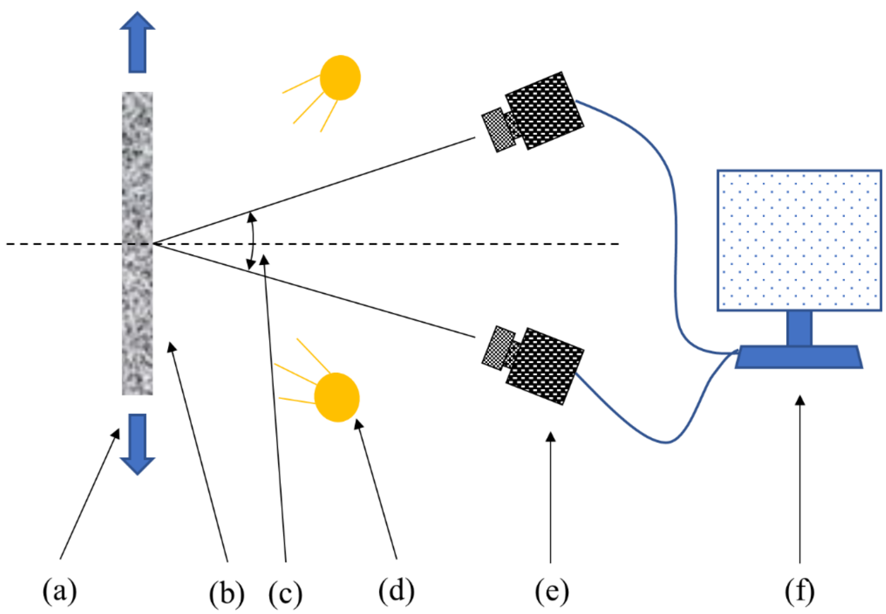

Figure 2-10: Configuration of 3D-DIC displacement measurement technique including (a) loading system, (b) test specimen under loading (c) stereo angle between cameras, (d) light sources, (e) CCD cameras, and (f) DIC processing computer.

Specimen deformation is measured by tracing contrast features between the stack of images captured from the specimen surface during loading stroke [109]. For this purpose, each captured image is segmented subsets equally spaced, and an image correlation algorithm analyzes each subset. Then, by averaging each subset's displacement, a displacement vector is generated. By putting all displacement vectors of all subsets together, the full-field deformation of the test specimen is generated. An example processed 3D DIC result of a TBC is shown in Figure 2-11. This figure shows how the braid is deformed and demonstrates how 3D DIC can measure the strain at every single spot of the braid. More information on DIC fundamentals can be found in DIC reference books [110] and [106] and is also provided in the following chapters on individual studies.

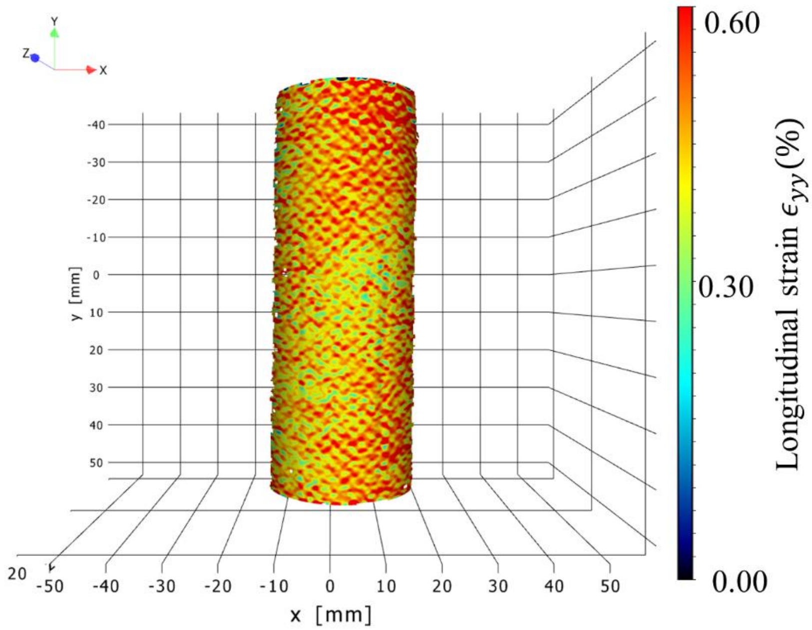

Figure 2-11: Example processed DIC result of a TBC.

2.5 Proposed study on tubular braided composites (TBCs)

This study aims to investigate the mechanical behaviour of 2D regular (2/2) pattern TBCs under combined tension/torsion loading. For this purpose, carbon fibre, fibreglass and Aramid TBCs are manufactured manually using shrink tape wrapping technique. Before conducting combined loading experiments, tensile experiments are performed on similar TBCs to investigate and understand the elastic and failure behaviour of manufactured braids, which is essential for designing a combined loading experiment. The tensile study of the braids is presented separately in Chapter 3. In this chapter, elastic and failure strain fields, elastic mechanical constants, necking process, and fracture modes of manufactured TBCs under tensile loading are studied. Chapter 3 also elaborately explains the manufacturing process of 2D TBC test specimens. Mechanical properties of carbon fibre, fibreglass and Aramid TBCs are assessed under combined loading in chapter 4. In this chapter, strain behaviour, failure mechanism, buckling trend and stiffness characteristic of TBCs are investigated. 3D DIC, as a contact-free full-field measurement technique, is utilized to study the deformation of TBCs for both tensile and combined loading experiments. The results presented in these studies can be used for evaluating numerical and analytical models for predicting the mechanical behaviour of 2D TBCs under tensile and combined loading.

Chapter 3 Tensile loading experiment on tubular braided composites

3.1 Introduction

This chapter explores the tensile mechanical behaviour of the tubular braided composites (TBCs) that will be studied in chapter 4 under combined loading. As explained earlier in chapter 2, in order to design experiments on TBCs under combined loading, the mechanical response of the braids under tensile loading needs to be studied. For combined loading experiments, samples will be preloaded to specific tensile stress safely within the elastic limit of carbon fibre, fibreglass and Aramid braided composites. Therefore, to determine the elastic limit for all three types of braids, similar specimens with exactly similar manufacturing procedures are studied under static tensile loading. The investigation on the tensile response of TBCs in this chapter will not be limited to the determination of the elastic range of deformations; but also elastic and failure strain fields, elastic mechanical constants, necking process, failure modes and manufacturing consistency of carbon fibre, fibreglass and Aramid braids are studied and compared.

Mechanical properties of TBCs in tension loading have been investigated by several researchers [7], [8], [20], [24], [111], and they have used different techniques for deformation measurements. For example, Harte and Fleck investigated fibreglass TBCs to understand and model their deformation and fracture responses in braiding angles between 23° and 55° [7]. They found that for TBCs, failure occurs due to fibre fracture for small braid angles, and braid fails because of neck propagation for large braid angles. They used conventional strain gauges to measure deformations for their manufactured TBCs.

Carey *et al.* developed an analytical model for the prediction of longitudinal elastic modulus of 2D TBCs. They compared the accuracy of the model with their manufactured Kevlar 2D TBC with two different braiding angles [111]. The comparison between analytical and experimental results was promising and error was less than 10%. They used an extensometer for doing strain measurement on test specimens.

Ayranci and his colleagues studied tensile tests on open meshed carbon fibre, fibreglass, and Aramid TBCs to validate an analytical model. [19], [112]. According to their experimental results, the average longitudinal elastic modulus for carbon fibre and Aramid braids was close and about 2.95GPa, and for fibreglass braids, were about 1.44 GPa. They used conventional extensometer to do strain measurements on braided composites.

Leung *et al.* studied Aramid TBCs using a stereomicroscope. They utilized a three-dimensional digital image correlation (3D DIC) method for strain measurement to see how nominal diameter and braid angle changes during tensile test stroke [20]. According to their investigations, by examining full-field unit cell strain and surface reconstruction of Aramid TBCs, the changes in braid angle and braid radius in the tensile experiment could affect the calculated elastic modulus by about 10%.

Melenka *et al.* published an elaborated study on the mechanical behaviour of 2D tubular Kevlar braided composites in different braiding angles and patterns under tensile loading using 3D DIC [8]. Their experimental results demonstrated that, for the same braiding pattern, longitudinal elastic modulus and maximum stress values for specimens with smaller braiding angles are significantly higher than of values for larger braiding angles. Moreover, for the same braiding angle, the longitudinal elastic modulus and maximum stress magnitude for regular braiding patterns were higher than the values for braids with diamond patterns.

Bossio *et al.* studied the effect of braid angle on tensile properties of TBCs manufactured by cellulose fibres with bio-based resins using the 3D DIC technique [24]. They compared the elastic modulus of their samples to the moduli of similar braids with synthetic materials. They suggested that their manufactured cellulose fibre braids and Ecopoxy resin could be a suitable replacement for E-glass braids for high stiffness to weight ratio applications.

Presently, although experimental studies have been completed in braided composites, there has been no detailed investigation on the mechanical response of TBCs manufactured using different fibres under tensile loading. This chapter aims to fill this gap by showing detailed analysis and comparison on carbon fibre, fibreglass and Aramid regular (2/2) pattern TBCs manufactured using a single manufacturing procedure. The results presented in this chapter can be used for evaluating numerical and analytical models for these three different braided composites.

3.2 Experimental methods

3.2.1 Sample manufacturing

Braid samples were manufactured using carbon fibre (2", 7.5 oz/sq yd, 3K, FibreGlast Developments CORP, Brookville, Ohio), fibreglass (2", 10.4 oz./sq yd, 0.011" Thick, FibreGlast Developments CORP, Brookville, Ohio) and aramid (2", 9.9 oz./sq yd, 0.018" Thick, FibreGlast

Developments CORP, Brookville, Ohio) biaxial sleeves in Regular (2/2) braiding pattern. Figure 3-1 shows braid preforms for carbon fibre, fibreglass and Aramid.

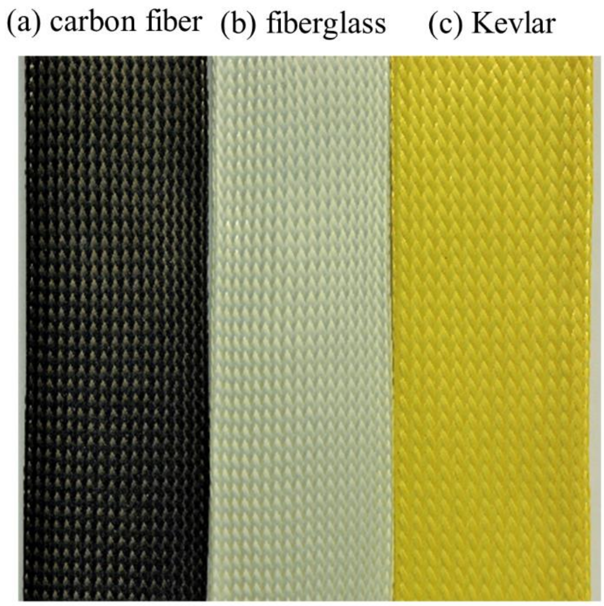

Figure 3-1: Three types of braid preforms used in this study (a) Carbon fibre (b) Fiberglass (c) Aramid.

Braid preforms were manually impregnated with an epoxy resin system (2000 epoxy resin with 2060 hardener, FibreGlast Developments CORP, Brookville, Ohio). Each sleeve was pulled over a steel mandrel (1566 Carbon Steel McMASTER-CARR, Elmhurst, IL) of 38.08 mm (1.5") diameter coated with mold release (LOCTITE® FREKOTE 770-NC™, Henkel Canada Corporation, Mississauga, Ontario) and then impregnated by resin-hardener with a weight mixing ratio of 100:27. Averaged properties of braid preforms and resin-hardener used for manufacturing braided composites are listed in Table 3-1 and Table 3-2, respectively.

Table 3-1. Reported averaged properties of braid preforms used for manufacturing braided composites [2], [88]

	Number of yarns in the braid	Longitudinal elastic modulus (GPa)	Ultimate Tensile Strength σ_{UTS} (GPa)	Density ρ (g/cm^3)	Yield (kg/m)	Fabric weight (g/m^2)
Carbon fibre	144	236.14	4.3	1.75	24.7	254.3
Fibreglass	144	72	3.5	2.57	26.5	352.6
Aramid (Kevlar 49)	120	125 ± 13	3.6	1.44	18.7	336

Table 3-2. Mechanical properties for cured resin-hardener (2000 series resin with 2060 hardener, FibreGlast)

Mechanical Properties	Reported data
Longitudinal elastic modulus (GPa)	2.9
Ultimate tensile strength $\boldsymbol{\sigma_{UTS}}$ (MPa)	67.7
Density $\boldsymbol{\rho}$ (g/cm^3)	1.11

For resin impregnation of the braided samples, the impregnated preform was covered with a release fabric ply (Airtech Bleederlease, Composites Canada, Canada) and then wrapped with 31.75 mm (1.25") heat shrink tape (Airtech Dahlar A575RC Shrink Tape**,** Composites Canada, Canada) while the mixture of resin-hardener was still in its pot life. Using a heat gun (Model No. HG1300, Black & Decker, China), the tape wrapped over the braided preform was shrunk, and excess resin squeezed out of the braid without leaving any trace of tape due to the use of release fabric. The schematic of the manufacturing process is demonstrated in Figure 3-2. The impregnated braids were cured at room temperature after 24 hours. This manufacturing technique was used to ensure even compaction of the braid samples and to produce a relatively even surface finish. A total of nine samples were manufactured, three of each type of preforms. Braided composites were cut into 317.5mm (12.5") as the final length using a cut-off saw (Mecatome T260, PRESU, France). While cutting, a 38.1mm (1.5") diameter 3D printed bushing was temporarily inserted in the specimen to facilitate a right-angle end and compensate for the radial flexibility of braid.

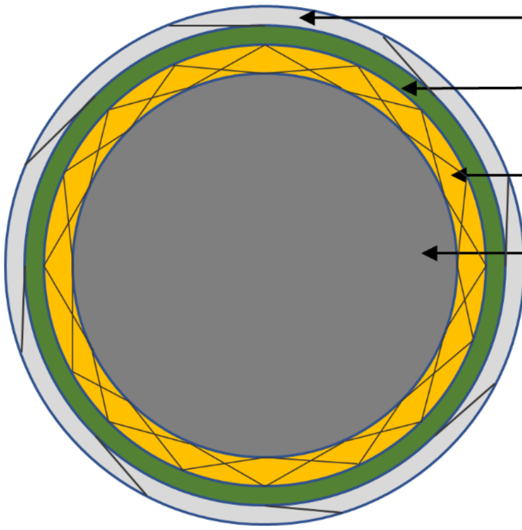

Figure 3-2: Schematic illustration of the manufacturing process. Steps of manufacturing are: 1) coating steel mandrel with mold release. 2) overlaying preform on the mandrel and impregnating it. 3) applying release fabric. 4) wrapping the shrink tape over the braid.

3.2.2 Specimen geometry measurement

The outer diameter, D_o, of braided composite samples were measured at five equally spaced locations along the longitudinal direction on braid using a micrometer (25.4–50.8 mm Micrometer, Starrett 3732XFL-2 Inch, Athol, MA). The inner diameter, D_i, was considered the same as the outer diameter of the steel mandrel. The braid unit cell, shown in Figure 3-3, represents the architecture of the entire composite [76]. Braid angle, θ_b, is the angle between longitudinal and fibre direction of braid. Braid angle is a parameter that significantly affects the mechanical properties of braided composites [77]. Yarn width, W_y, is a geometric factor that affects the geometry of braided composite [78]. Braid angle and yarn width illustrated in Figure 3-3 are two geometrical parameters of braids that are commonly measured and reported in studies on braided composites [14], [22], [79], [80]. Braid angle and yarn width were measured on digital images captured from braids in five locations along the longitudinal direction of the braid using an image processing software (ImageJ, National Institutes of Health, Bethesda, MD). For this purpose, each braid was photographed five times using a high-resolution camera (Ace acA2440-35um Monochrome USB 3.0, Basler Inc., Exton, PA) equipped with a macro lens (Model No. MLM-3XMP, 2/3" 3.3X Macro Zoom, Computar, US). For the purpose of fibre volume fraction (v_F) measurements, initial fibre mass and the braided composite mass were weighed using a high accuracy scale (Model No. ML304T/00, METTLER TOLEDO, Canada). Then the matrix mass was determined from 3-1. In this equation, m_m, m_b, and m_f are matrix mass, braided composite mass and fibre mass, respectively.

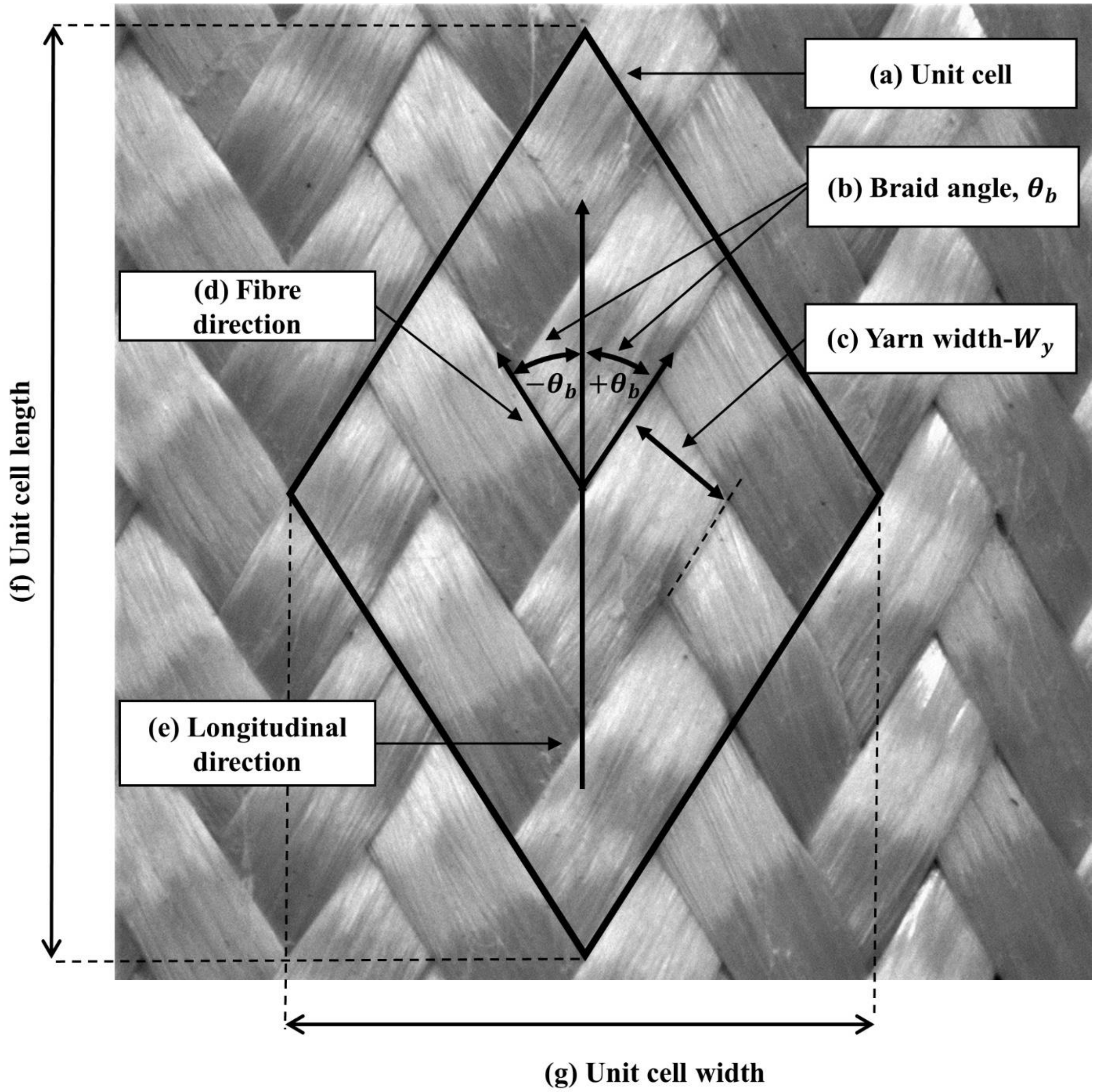

Figure 3-3: Schematic illustration of braid's unit cell and its geometrical parameters. This figure shows a) unit cell of a regular braid, b) braid angle, c) yarn width, d) fibre direction, e) longitudinal direction of braid, f) unit cell length and g) unit cell width.

$$m_m = m_b - m_f \qquad 3\text{-}1$$

3.2.3 Mounting specimens on tabs

The braids were bonded to end tabs (Figure 3-4) made of cold-rolled steel C1045 using a high strength two-part epoxy (Loctite E- 20HP; Hysol, Henkel, Rocky Hill, Co.). End tabs were used to avoid stress concentration and radial deformation on specimens due to the test frame's grips. The end tabs had a 1.5° tapered portion to provide a sufficient gap for the epoxy, similar to methods in [22], [113]. After placing tabs in the braid, 203.2 mm (8") of braids remains contact-free, which will experience evenly distributed loading in mechanical tests. Bonded tabs were rested on an angle steel bracket and fastened at both ends for 24 hours until the high strength epoxy cures. The use of angle brackets and fasteners minimizes the misalignment of tabs. The assembly of the test specimen and the angle bracket setup is shown in Figure 3-4.

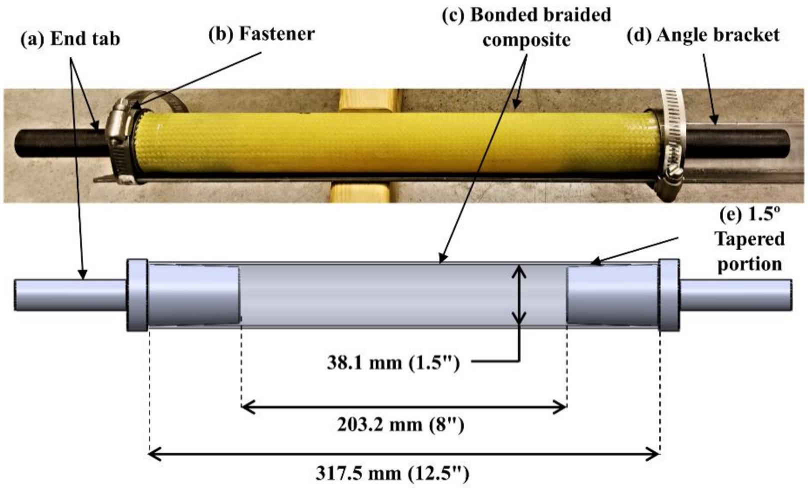

Figure 3-4: Picture and geometrical configuration of TBC test specimen. The figure shows a) end tabs, b) fasteners, c) bonded braided composite, d) angle bracket and e) the 1.5° taped portion of the end tab.

3.2.4 Sample mechanical testing

Carbon fibre, fibreglass, and Aramid braided composite samples were evaluated in tension loading to investigate and compare their strain fields, elastic characteristics, necking behaviour and fracture modes. As there is no specific standard for TBCs for the tensile loading test, ASTM E111 [114] and D3039 [115] standards were used as a guide for performing the experiments and reporting characteristic parameters such as young modules and fracture modes. The axial/torsional test frame (809 MTS Systems Corporation, USA) shown in Figure 3-5 was used to perform mechanical tests. Force was measured using a 100 KN axial load capacity unit (Model number: 319.10, MTS Systems Corporation, USA). Force and displacement data were recorded using the test frame's data acquisition system. The axial load was applied in displacement control mode at a crosshead speed of 1mm/min to the complete failure of specimens. This load rate was chosen according to ASTM D3039 [115] with some modifications so that instead of having specimens fail completely between 1 to 10 min, all specimens experienced their plastic deformation within the aforementioned period. This modification was considered to ensure that deformations occur slow enough so that the measurement technique works correctly.

3.2.5 Deformation measurement

Surface deformation measurements for tests were performed by the Three-Dimensional Digital Image Correlation (3D DIC) technique. 3D DIC allows capturing and tracing braiding patterns and braid yarns during mechanical tests. 3D DIC setup includes two high-resolution cameras (LaVision Image M-lite 5M, LaVision GmbH, Göttingen, Germany) with a resolution of 2464×2056 pixels and a pixel size of 3.45 µm and digital output of 12 bit. The cameras were equipped with 50 mm focal length lenses (NMV-50M23, Navitar, Inc., Rochester, NY). The distance between cameras and specimen was approximately 850 mm. The images were acquired using a commercial software package (DaVis version 10.0.3 StrainMaster, LaVision GmbH, Göttingen, Germany). Two LED panels (Neewer 500 LED Photo Studio Lighting Panel, Shenzhen, China) were used for illuminating specimens while imaging their deformation during loading. According to the sample and camera configuration, a stereo angle of 17° was used. This stereo angle was determined to maximize the usable depth of focus, get an effective field of view, FOV, and also reduce out-of-plane uncertainty according to a guidebook on the DIC measurement technique [106]. The camera setup was designed to have an approximate FOV of 115×94 mm^2 (Figure 3-6). The braids were positioned in the center of both cameras FOV. A sufficient length of braid was captured using this FOV to compensate for large displacements in tensile tests. The image acquisition rate was 1 Hz. The summary of the imaging setup configuration is listed in Table 3-3. The experimental test setup is shown in Figure 3-5. This figure shows the MTS test frame, mounted specimen, stereo cameras, LED lights and the LaVision imaging system.

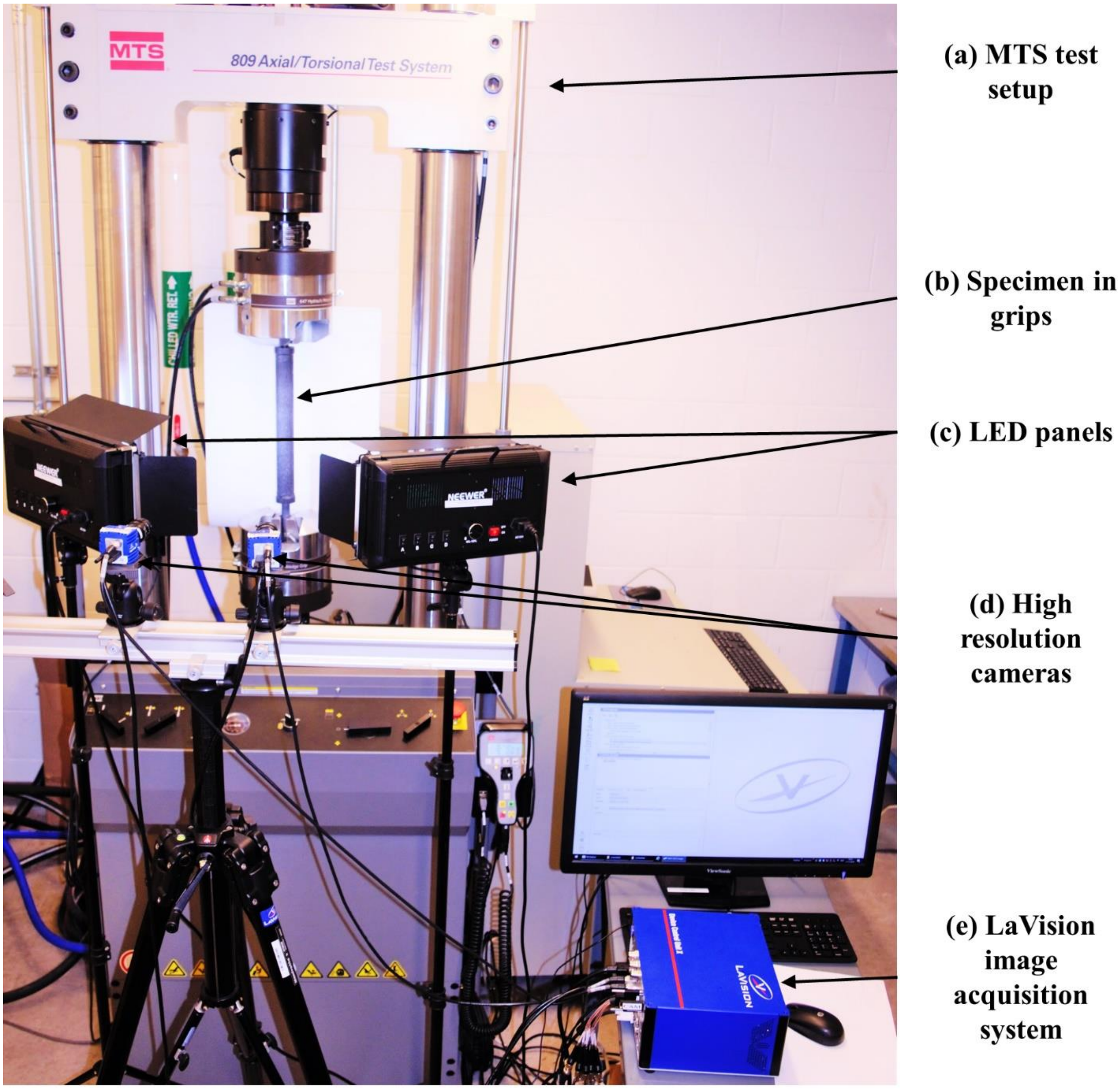

Figure 3-5: Experimental setup configuration including a) MTS test setup, b) specimen on grips, c) LED panels, d) high-resolution cameras, and e) LaVision image acquisition system.

Table 3-3: Image acquisition setting.

Digital image correlation parameters	Settings
Camera Resolution	2464×2056 pixels
Camera Pixel Size	3.45 μm
Digital output	12 bit
Camera Lenses	2X Navitar 50mm lens
Distance Between Cameras and Specimen	850 mm
Stereo Angle of Cameras	17°
Camera Field of View (FOV)	115 × 94 mm^2
Image Acquisition Rate	2 Hz

3.2.6 DIC Sample preparation

High-quality speckle patterns are required to ensure proper DIC measurements. High contract speckles allow using relatively small subset size, which helps to obtain more precise strain fields for samples [110]. A speckling procedure similar to methods used in [14], [22] was followed. Initially, specimens were painted a flat black spray paint (Painter's Touch Flat Black, Rust-Oleum Corp, Concord, On) to minimize the reflection of light on the surface along with ensuring uniform contrast before speckling. After applying the flat black paint, a mixture of white colour (Opaque White, Aztek Airbrushable Acrylic Paint, Testors Corp) and reducer (4012 High-Performance Reducer, Createx) was applied to the samples using an airbrush (H-SET, Paasche Airbrush Company, Chicago, IL). The colour selections were made to optimize contrast on the braid surface. An example painted and speckled braid is illustrated in Figure 3-6. In this figure, the image intensity variation along the white dashed line in transverse direction of speckled braid is shown. The portion of image intensity which corresponds to the region of interest, ROI, of specimen is demonstrated using vertical black dashed lines. This ROI will be used to perform averaging on strain measurements. Figure 3-6 shows that the test samples have sufficient contrast variations that will be suitable for DIC measurement.

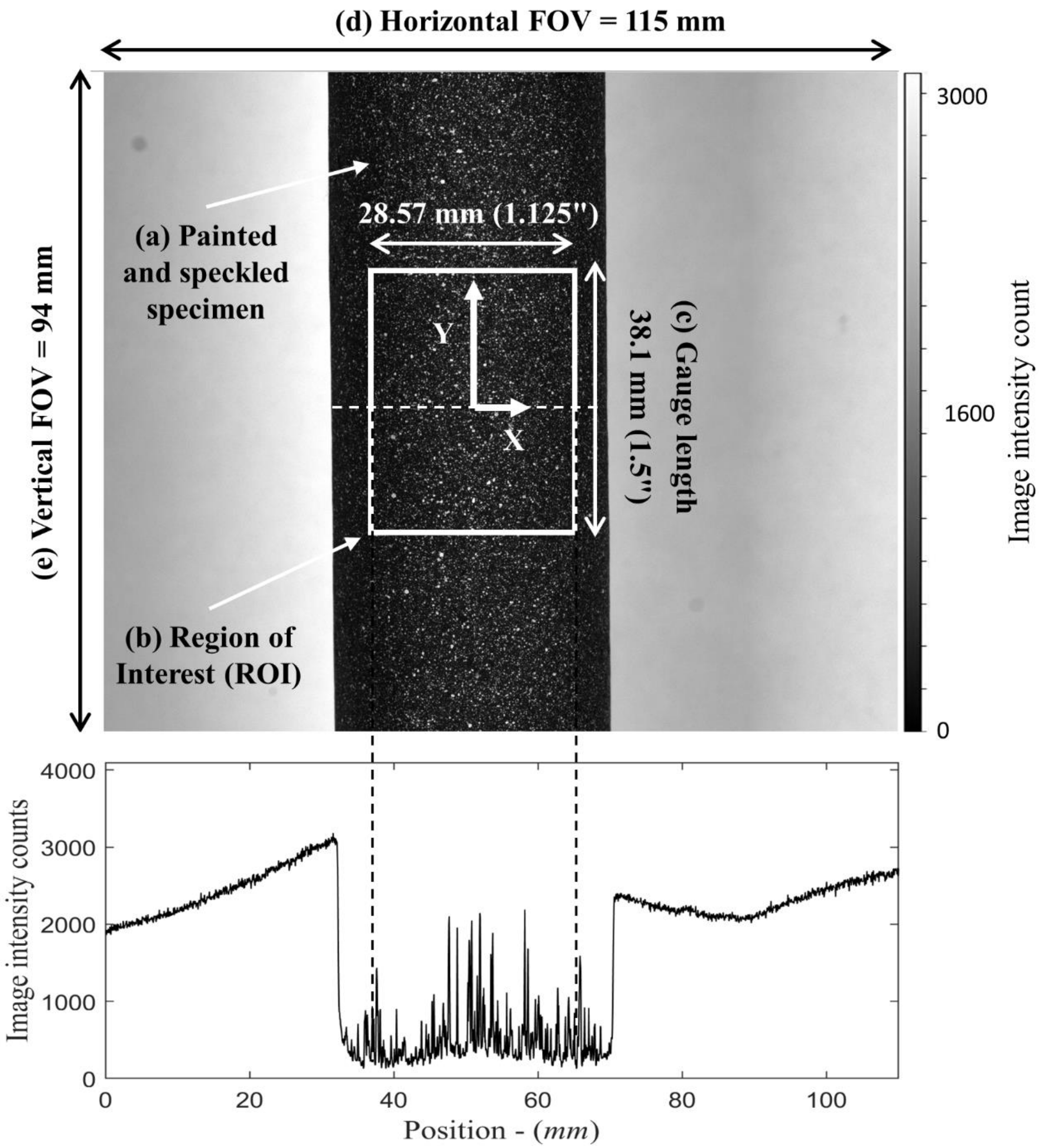

Figure 3-6: A raw image from DIC cameras. This figure shows a) painted and speckled specimen, b) ROI, c) gauge length of braid used for strain measurement, d) horizontal FOV, and e) vertical FOV. The image intensity counts along the transverse direction of the braid is also shown.

3.2.7 3D DIC processing and post-processing

DIC processing of captured images during tensile tests for strain and displacement measurement was completed using a commercial DIC software package (DaVis version 10.0.3 StrainMaster, LaVision GmbH, Gottingen, Germany). To perform 3D DIC, images acquired from both cameras were linked and calibrated using a calibration process. For calibration, a 106×106 mm^2 calibration target (Type 106-10-SSDP, LaVision GmbH, Göttingen, Germany) was placed in the test frame's grips using a holder such that its center would coincide with the center and the front surface of the specimen when the specimen was mounted in the test frame. This way, the center of the braid surface would stay in focus and within the FOV of cameras during test stroke.

A least-square optical flow displacement measurement algorithm was used to drive displacement vector fields (Figure 3-7) using DIC processing software [116]. A subset window size of 21×21 pixels and a step size of 7 pixels were used to perform a correlation between images. Selecting a 38.10×28.57 mm^2 ROI (1.5×1.125 inch^2) and using processed displacement vector fields in the ROI, the averaged longitudinal strain, ϵ_{yy}, and transverse strain, ϵ_{xx}, in a gauge length of 38.10 mm (1.5") (Figure 3-6) were calculated during test stroke. ASTM D3039 was used as a guide to determine the gauge length [115]. According to a study by Naik *et al.* [117], the ROI must be larger than the braid unit cell to produce consistent strain results. The ROI in Figure 3-6 is large enough to ensure bulk strain is measured over multiple unit cells since the average unit cell length and width (Figure 3-3) for all three types of braids are 9.13 mm ± 0.88 mm and 5.27 mm ± 0.03 mm, respectively. The DIC analysis parameters are summarized in Table 3-4.

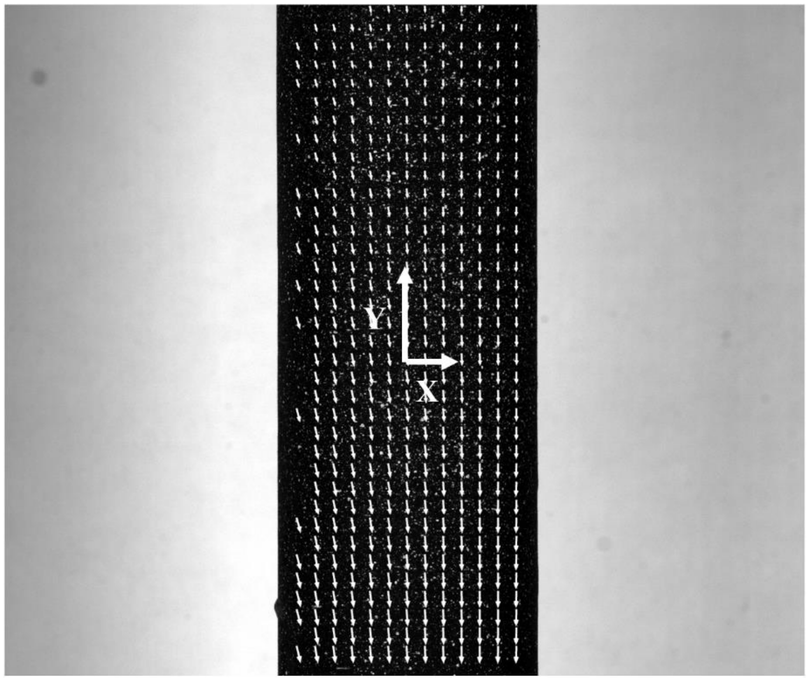

Figure 3-7: Example displacement vector field of a TBC. The vector density has been reduced to 1 in 8 for clarity. The sample coordinate system is shown for calculation of longitudinal, ϵ_{yy}, and transverse, ϵ_{xx}, strains.

Table 3-4. Digital image correlation settings.

DIC parameters	Settings
Image Scale Factor	21 pixels/mm
Correlation Subset Size	21 × 21 pixels
Correlation Step Size	7 pixels
Region of Interest (ROI)	38.10 × 28.57 mm^2 (1.5 × 1.125 inch^2)
Gauge Length	38.10 mm (1.5")

3.3 Results and discussion

3.3.1 Braid geometry analysis

The inner (D_i) and outer (D_o) diameters of manufactured TBCs were physically measured using a high accuracy micrometer. The diameter measurements were used to determine cross-sectional areas of braids. The cross-sectional area (A) is required to determine the braid's axial stress. Braid angle (θ_b) was accurately measured using a high-resolution camera equipped with a macro lens and ImageJ software. Yarn width (W_y) was also optically measured for braid angle measurement. The average value and the standard deviation for inner diameter, outer diameter, braid angle, braid yarn width measurements and calculated cross-sectional area are listed in Table

3-5. Inner diameters of braids were considered as the outer diameter of the mandrel and had minimal variation due to the perfect surface finish of mandrel.

Having densities from Table 3-1 and Table 3-2 and using measured fibre mass (m_f) and matrix mass (m_m) listed in Table 3-5, fibre volume (V_f) and matrix volume (V_m) were calculated using Equations 3-2 and 3-3. In these equations, ρ_f and ρ_m are the fibre and matrix densities, respectively. Using calculated fibre (V_f) and matrix (V_m) volumes, fibre volume fraction (v_F) measurements were performed using Equation 3-4. The averaged fibre volume fraction with its standard deviation for three group of braids is summarized in Table 3-5. According to [2], the fibre volume fraction for typical laminates is between 50% to 70% and can be lower for braided composites. The fibre volume fraction measured for the manufactured braids in this study is lower than 40%, which agrees with the expectations in [2].

$$V_f = \frac{m_f}{\rho_f} \qquad 3\text{-}2$$

$$V_m = \frac{m_m}{\rho_m} \qquad 3\text{-}3$$

$$v_F = \frac{V_f}{V_f + V_m} \qquad 3\text{-}4$$

Table 3-5. Average geometrical properties with ± standard deviations for manufactured braids.

Braid type	Inner diameter $\boldsymbol{D_i}$ (mm)	Outer Diameter $\boldsymbol{D_o}$ (mm)	Cross-sectional area $\boldsymbol{A}$ (mm^2)	Braid angle $\boldsymbol{\theta_b}$ (degree)	Braid yarn width $\boldsymbol{W_y}$ (mm)	Fibre mass $\boldsymbol{m_f}$ (g)	Matrix mass $\boldsymbol{m_m}$ (g)	Fibre volume fraction $\boldsymbol{v_F}$ (%)
Carbon 3K	38.08 ± 0.00	39.08 ± 0.03	60.08 ± 1.60	33.63 ± 0.58	1.50 ± 0.09	12.71 ± 0.00	16.12 ± 1.91	33.47 ± 2.53
Fiberglass	38.08 ± 0.00	38.95 ± 0.13	52.51 ± 7.94	31.55 ± 1.81	1.43 ± 0.04	17.97 ± 0.00	12.84 ± 3.55	38.49 ± 7.15
Aramid (Kevlar 49)	38.08 ± 0.00	39.56 ± 0.12	90.21 ± 7.72	30.95 ± 0.38	1.71 ± 0.12	17.89 ± 0.32	21.03 ± 3.26	39.83 ± 3.55

The outer diameter of braids was also calculated using surface height data extracted from DIC results. A similar approach was performed by Leung *et al.* [118]. Using a circle fitting function [119], five circles were fitted on surface height data to get five outer diameter measurements for each braid. Figure 3-8 shows an example fitted circle on DIC height data. In this figure, the reconstructed surface from DIC data has formed a semicircle and is shown by line (i). Line (ii) in this figure shows the fitted circle on DIC data of line (i). The diameter of this fitted circle was considered as the outer diameter of braid measured from DIC results.

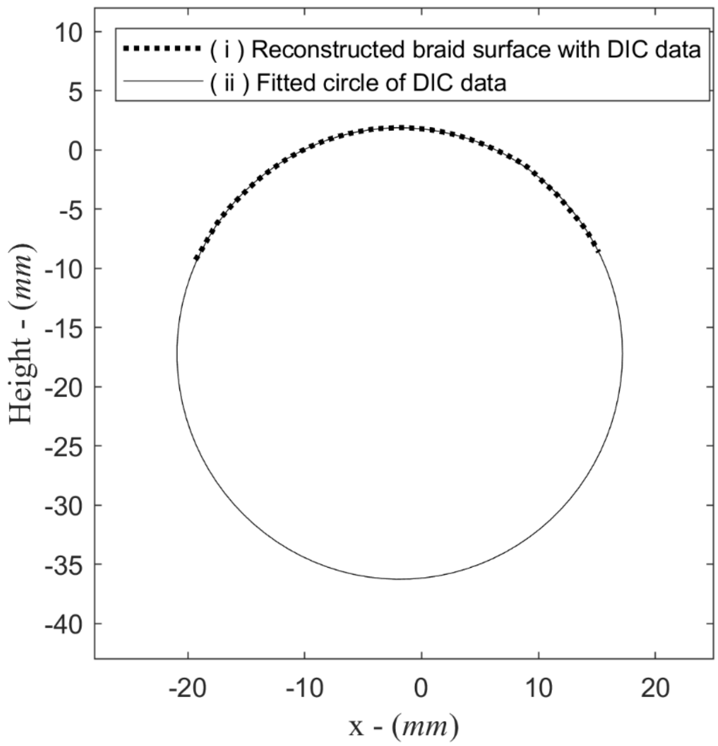

Figure 3-8: An example of outer diameter measurement of the braid using circle fitting on DIC result.

For validating the accuracy of DIC measurements, the fitted outer diameter measurements were compared with the physically measured outer diameter with the micrometer. This comparison indicates that stereo cameras were correctly placed and calibrated and ensures that strain and displacement measurements with DIC technique has high accuracy. A similar comparison for DIC accuracy validation was made in [8]. Table 3-6 shows the comparison of outer diameter between physically and optically measurement techniques. This table demonstrates a good match between the measurements. 1.03% is the maximum difference between physically and fitted outer diameter for the braids. The acceptable agreement between physically measured diameters and the diameters from the fitted circle on DIC height data states that the 3D DIC technique was accurate and well-calibrated for all the experiments; therefore, the resulting strain and displacement values of DIC measurement were reliable. According to Table 3-6, the standard deviation values for diameters of the fitted circles are meaningfully higher than those measured with the micrometer. The main reason is the precision of high-quality images captured with the DIC technique with high-resolution cameras. These images account entirely for the waviness surface of braided composites due to yarn interlacement, while the micrometer cannot reflect the nonhomogeneous surface of the braid. Therefore, extracted height data from 3D DIC measurements show variation due to the nature of braid's surface structure and results in a larger magnitude for standard deviations of fitted diameters than the diameters measured physically.

Table 3-6. Comparison of braid specimen outer diameters measured using physical technique and fitted surface height data of DIC results.

Braid type	Physically measured $\boldsymbol{D_o}$ (mm)	St Dev of physically measured $\boldsymbol{D_o}$ (mm)	$\boldsymbol{D_o}$ of the fitted circle using DIC height data (mm)	St Dev of $\boldsymbol{D_o}$ of the fitted circle using DIC height data (mm)	Difference (%)
Carbon 3K	39.08	0.03	38.28	0.52	1.03
Fiberglass	38.95	0.13	38.34	0.28	0.80
Aramid (Kevlar 49)	39.56	0.12	39.01	0.70	0.75

3.3.2 Longitudinal strain and longitudinal modulus

Full-field strain measurement of tubular braided composites was conducted using the 3D DIC technique. Figure 3-9 represents an example of 2D images of longitudinal strain distributions on the surface of carbon fibre, fibreglass and Aramid braids when experiencing stresses from 40MPa to 250MPa. According to this figure, braids are experiencing inhomogeneous strain distribution due to the interwoven structure of braided composites. Figure 3-9 also indicates that when braids are under higher loads, strain magnitude intensifies illustrated by richer red strain fields. This figure demonstrates the longitudinal strain variations at the 250MPa corresponding to the dark vertical line in the middle of the braid. According to the range of strain variations in this figure, the Aramid specimen has the highest magnitudes of strains, and the carbon fibre sample shows the lowest values for strains. The strain's periods shown in Figure 3-9 corresponds to the period of yarns of the braids. Similar observations were seen in 3D DIC studies on TBCs by Melenka *et al*. [8] and Bossio *et al*. [24].

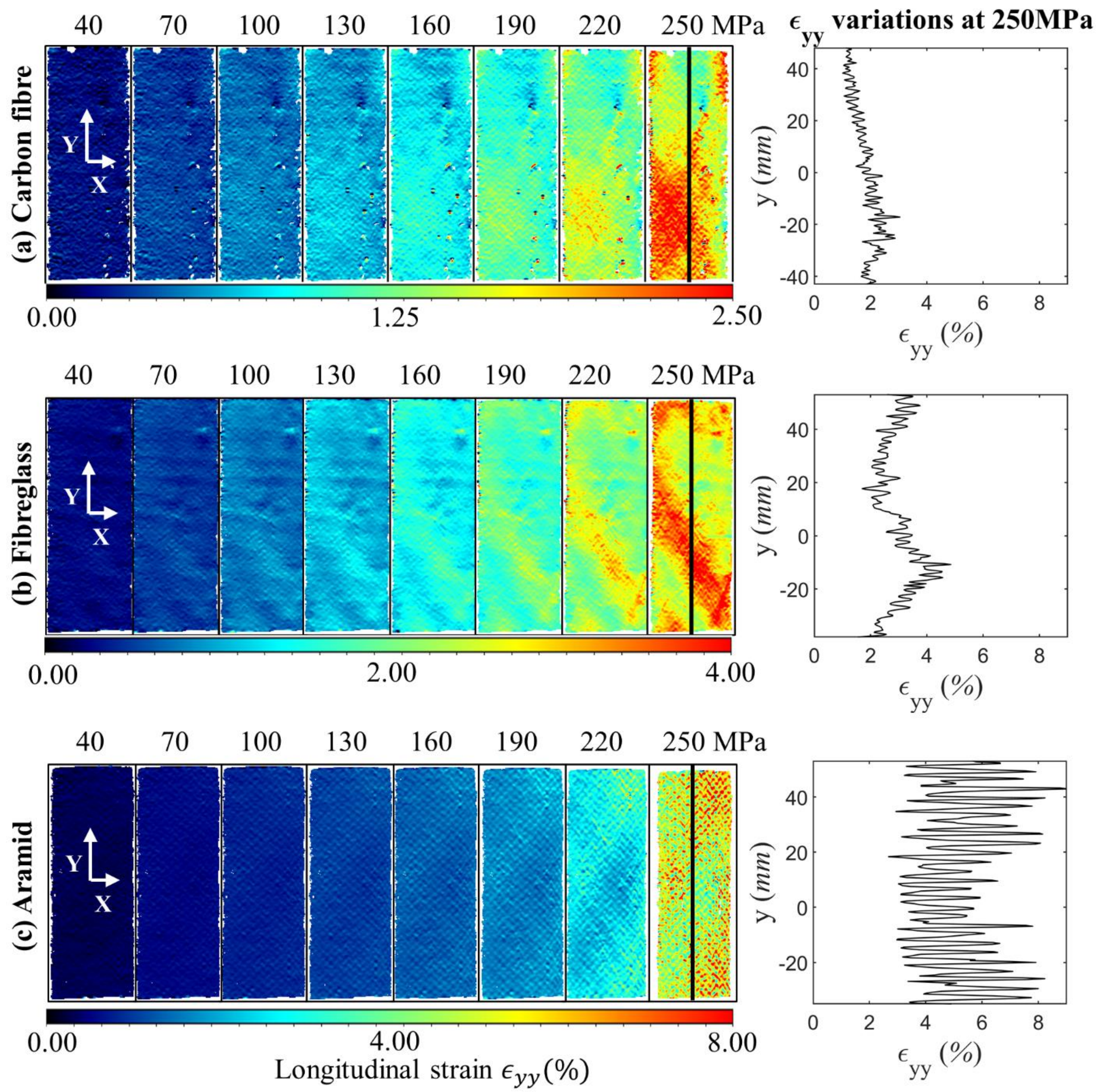

Figure 3-9: Longitudinal strain distribution on three types of braids for the stress range of 40 MPa to 250 MPa with increasing steps of 30 MPa. Sample images show the two-dimensional strain distribution for the tubular braids (a) Carbon fibre (b) Fiberglass (c) Aramid. Longitudinal strain distribution along the middle vertical dark line of sample braids at 250 MPa stress is plotted.

As illustrated in Figure 3-9, there is a significant strain variation on the braid's surface due to the yarn undulations in the braided structure. Therefore, the ROI demonstrated in Figure 3-6 was used to determine an average strain over the surface of the braid. The averaged strain magnitude is used to plot and examine strain curves in this study. This technique is similar to some other studies on 2D braided composites to determine effective strains [8], [14], [108]. The stress-strain curves for all samples tested are shown in Figure 3-10. In this figure, the stress type is axial stress, σ_{yy}, and the strain type is longitudinal strain, ϵ_{yy}. Figure 3-10 shows the full tensile stroke for all braid samples up to failure. According to this figure, all the braids experience elastic deformation at first and then have a smooth transition to the plastic region. This figure also shows that carbon fibre braids have a sharper slope than Aramid and fibreglass braids in the stress-strain plot, and the curves for Aramid and fibreglass braids have some overlaps.

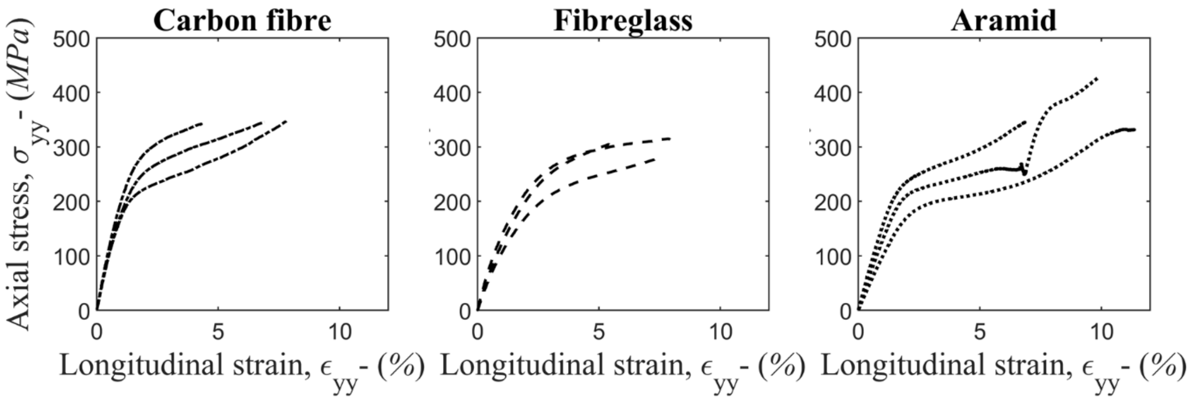

Figure 3-10: Stress-strain curves for for carbon fibre, fibreglass and Aramid TBCs in separate frames. The full stroke of tensile tests is shown for all samples.

Figure 3-11 shows 3D representations of axial strain distributions on the surface of carbon fibre, fibreglass and Aramid braids when experiencing three states of low tensile stresses at 20 MPa, 40MPa and 60MPa. This figure shows three stress steps at the beginning of the testing stroke, where braids are showing excellent linear behaviour in their stress-strain curves shown in Figure 3-10. Figure 3-11 demonstrates that strain fields follow the yarn directions of braids. Figure 3-11 shows that there is negligible localized strain concentration (less than 0.6%) on braids according to strain colour maps, which means for stresses between 20MPa to 60MPa, no failure has occurred in fibre or matrix components of braids.

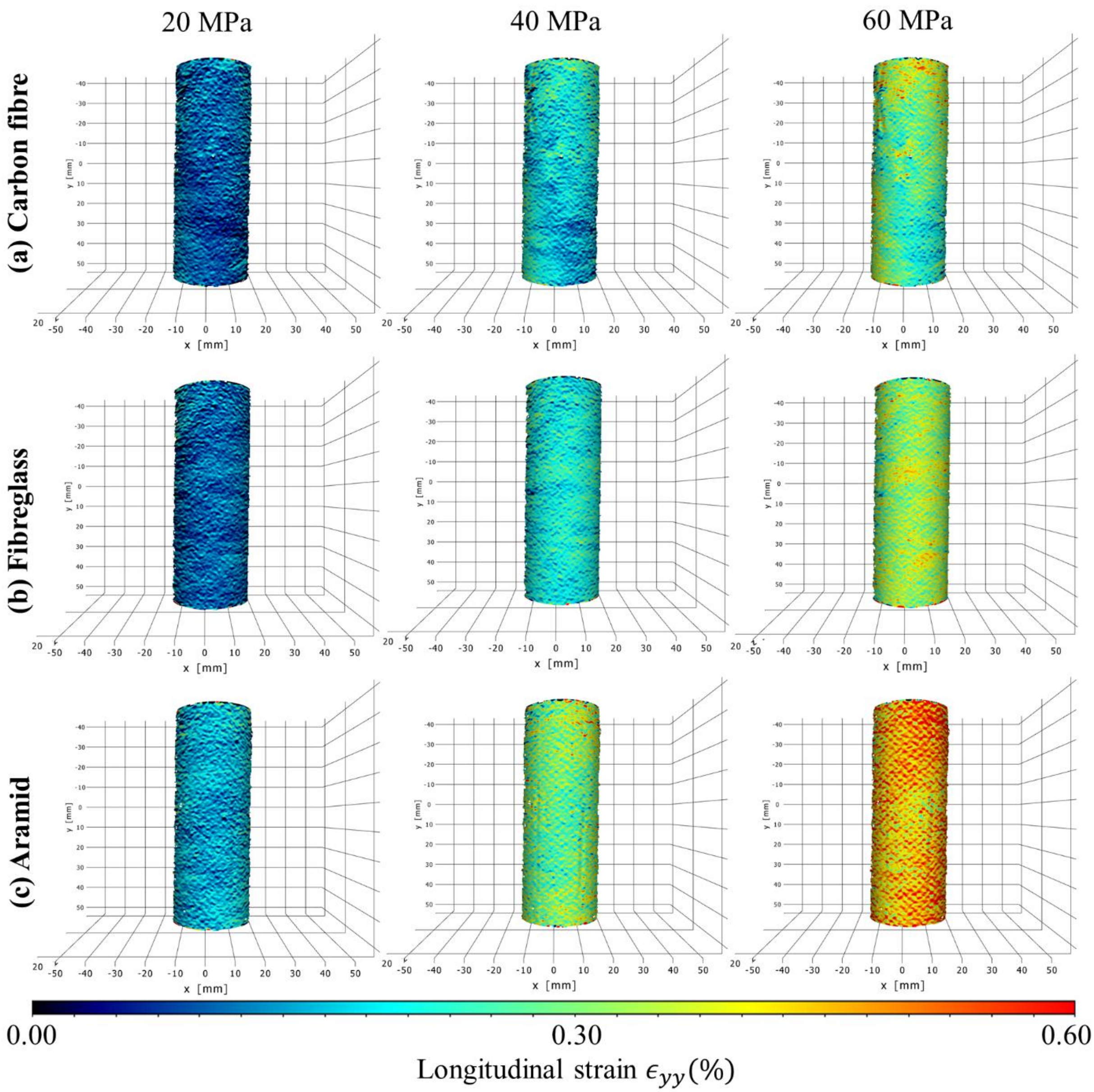

Figure 3-11: 3D representation of longitudinal strain distribution on three types of brads at low-stress states. Sample images show the three-dimensional strain distribution for the tubular braids (a) Carbon fibre (b) Fiberglass (c) Aramid. Sample stress of 20, 40 and 60 MPa are visualized.

The strain behaviour of braids under low-stress states is further discussed using the stress-strain plots of Figure 3-12. The linear region of stress-strain plots of Figure 3-10 is separately shown in Figure 3-12. The stress-strain line for each sample is plotted with high linearity of $R^2 = 0.99$. This figure indicates that for stresses between 20MPa and 60MPa, all the braids completely have elastic behaviour, which agrees with the strain maps demonstrated in Figure 3-11. The strain maps in Figure 3-11 do not show any significant localized strain concentrations. Figure 3-12 indicates that the linear elastic region of the stress-strain plot for carbon fibre and fibreglass braids ends sooner and at significantly lower strains than Aramid braids. Thus, Aramid braids can endure larger strain magnitudes than carbon fibre and fibreglass braids and do not show permanent deformations. This observation matched with strain variation plots in Figure 3-9, which shows much higher axial strain magnitudes for Aramid braids than carbon fibre and fibreglass braids.

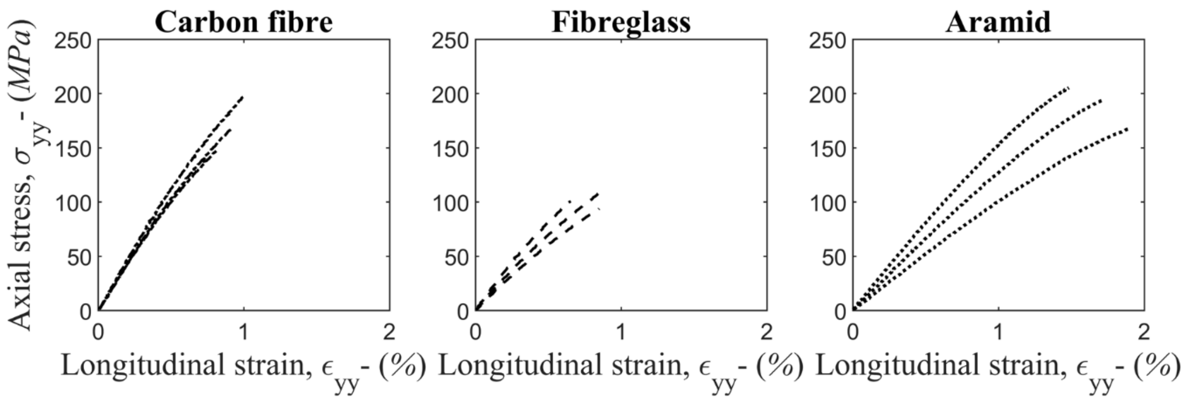

Figure 3-12: Linear region of stress-strain curves for carbon fibre, fibreglass and Aramid TBCs. These curves are used to calculate the longitudinal elastic modulus of different braids.

The stress-strain curves of Figure 3-12 are used to determine the longitudinal elastic moduli for each of the braid samples. The longitudinal elastic modulus for the material is defined as the slope of the linear region of its stress-strain plot. The magnitude of longitudinal elastic moduli for carbon fibre, fibreglass and Aramid braids are 20.00GPa ± 0.95GPa, 13.90GPa ± 2.37GPa and 12.20GPa ± 2.65GPa, respectively. Figure 3-13 demonstrates the relation between braid's fibre type and its longitudinal elastic modulus. The error bars are the standard deviation of each data set. This figure shows that carbon fibre braided composites have significantly higher elastic modulus than Aramid and fibreglass braids. The elastic moduli for Aramid and fibreglass braids are close and with overlapping error bars; however, the elastic modulus is higher for fibreglass samples than Aramid samples. There is no similar experimental study on braided composites to compare longitudinal properties of braids with different materials.

The decreasing modulus trend among these materials with carbon having the highest modulus and Aramid with lowest was also observed by Carey *et al.*[111]. They proposed an analytical model to study the mechanical properties of diamond braided composites and compared their model with some analytical and experimental studied for carbon fibre, fibreglass and Aramid braids. Xu *et al.* generated a finite element method to predict the mechanical properties of biaxial and triaxial braids in different braiding patterns for braids with flat unit cells [120]. They have predicted the longitudinal elastic modulus for carbon fibre and fibreglass braids to be 34.34GPa and 22.3GPa, respectively. The predicted values are for biaxial regular braids with the same braiding angles for braids listed in Table 3-5. The Xu *et al.* results are about 25% higher than the experimental results of this study on carbon fibre and fibreglass. The main reason for this difference can be due to the higher longitudinal modulus of fibre and matrix that were used as the input data for Xu *et al.* model. Comparison of fibre types here is not applicable since the exact type of all fibres is not reported by Xu *et al*. Moreover, their model was designed for braids with a flat unit cell; however, the moduli shown in Figure 3-13 are for tubular cross-section braids. Therefore, the difference between the results of Xu *et al.* model and this research study may be due to different shapes of cross-sections. Melenka *et al.* [121] introduced an analytical model to anticipate the mechanical properties of TBCs. They have suggested that for an Aramid (Kevlar 49) TBC with similar braid angle as of braids in this study the longitudinal elastic modulus is about 13.57GPa, which is quite close to what is already found for the Aramid braids of this experiment. The slight difference can be due to different geometrical parameters used in Melenka *et al.* model, such as the number of yarns, yarns width and braid diameter.

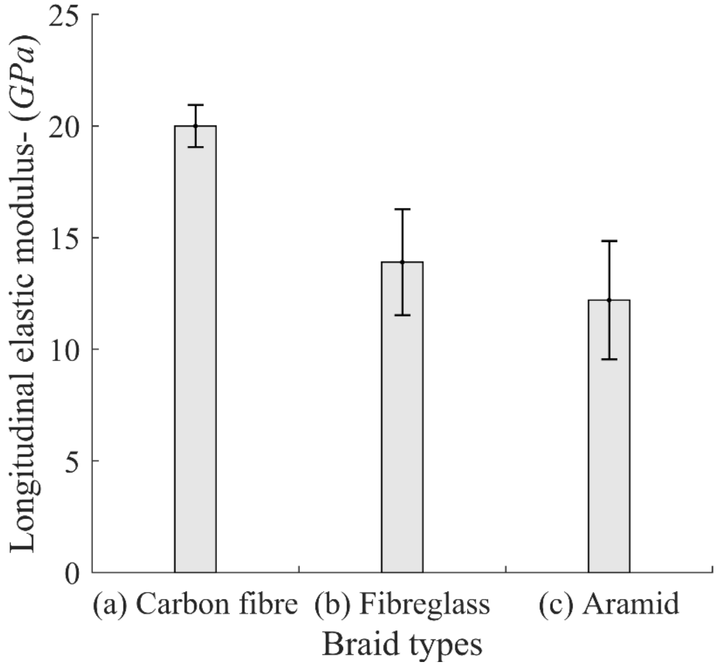

Figure 3-13: Longitudinal elastic modulus for three groups of TBCs, a) carbon fibre, b) fiberglass and c) Aramid.

3.3.3 Transverse strain (ϵ_{xx}) and necking

Similar to the axial strain distributions previously discussed, transverse strains for carbon fibre, fibreglass and Aramid TBCs are examined here. Figure 3-14 represents 2D transverse strain distributions of example braids for stresses between 40MPa to 250MPa. This figure indicates that when loading increases on braids, transverse strain magnitude intensifies, which is illustrated by richer blue shades in strain fields. As the load increases, inhomogeneous stress distribution due to the interwoven structure of braided composites becomes more evident. Figure 3-14 also demonstrates the axial strain variation of the braids at the 250MPa corresponding to the dark horizontal line in the middle of the braid. The strain's period corresponds to the period of yarns of the braids. Similar observations of strain period were seen in a 3D DIC study by Melenka *et al*. [8] on TBCs.

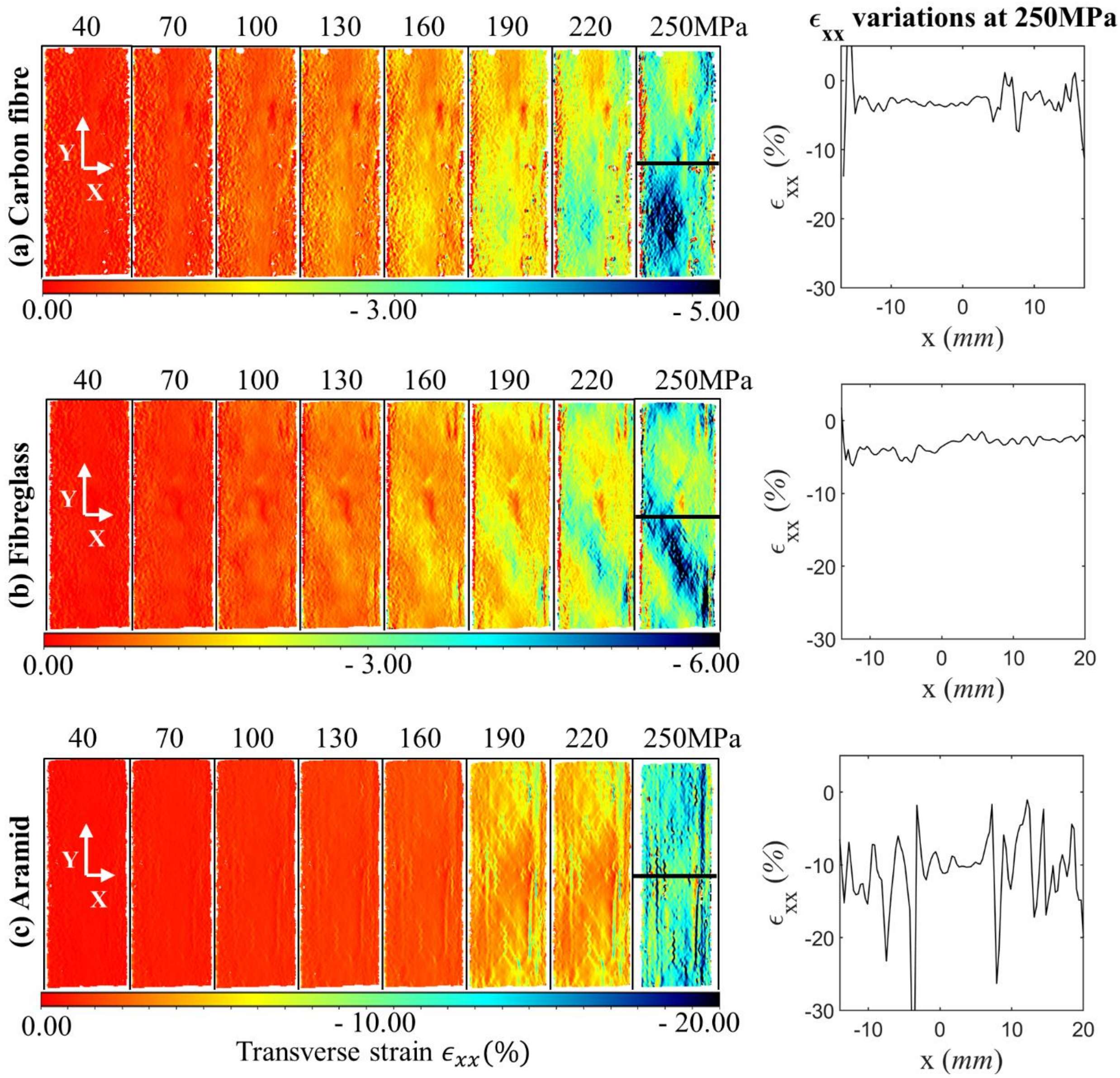

Figure 3-14: Transverse strain distribution on three types of braids for a stress range of 40 MPa to 250 MPa with increasing steps of 30 MPa. Sample images show the two-dimensional strain distribution for the tubular braids (a) Carbon fibre (b) Fiberglass (c) Aramid. Transverse strain distribution along the middle vertical dark line of sample braids at 250 MPa stress is also plotted.

In tensile tests, when loading increases and braided composites experience higher loads, strain concentrations become evident, matrix failure occurs, and specimens begin their necking process [8]. Figure 3-15 demonstrates the necking process of TBCs during tensile loading. In this figure, the surface height of braids corresponds to the horizontal dark line shown in Figure 3-14. The surface height is plotted during different stress stages from the unloaded specimen at 0 MPa, which is the initial curvature of the braid to Ultimate Tensile Stress, σ_{UTS}, at which braids fail. According to Figure 3-15, all three types of braids show minimal necking at 40MPa by having a complete curvature overlap with the unloaded stage. This observation also matches the strain maps of braids in Figure 3-14, which do not show significant transverse strain at 40MPa. At the stress of 190MPa, necking begins and is more evident for Aramid braids rather than carbon fibre and fibreglass specimens. This comparison also agrees with the details demonstrated in Figure 3-14, which shows larger strain values and sudden changes is strain fields for Aramid braids compared to the other two types of braids. Furthermore, stress-strain curves in Figure 3-10 proves this comparison, which shows that Aramid braids are approaching their plastic zone at stresses close to 190 MPa. Increasing load on braids from 190MPa to 250MPa and ultimate tensile stress, necking grows faster than the increase rate before 190MPa. This higher increase rate is due to the plastic deformation of braids, which occurs for loads higher than 190 MPa according to the stress-strain curve in Figure 3-10.

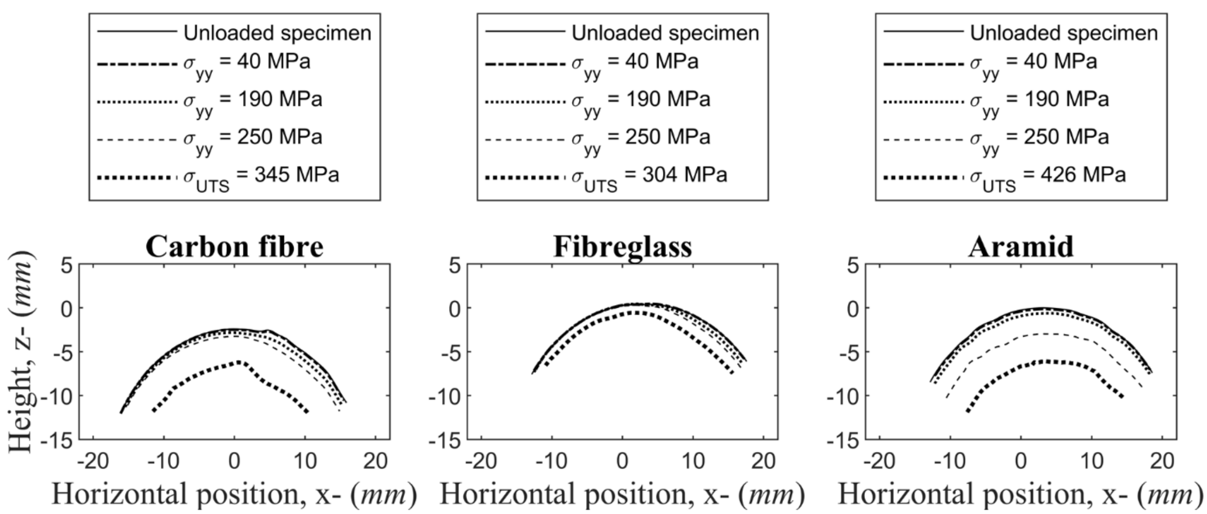

Figure 3-15: Surface profile of three example braids of each fibre type during complete loading stroke. The necking process of samples is shown for carbon fibre, fibreglass and Aramid TBCs.

Similar to Figure 3-11, Figure 3-16 shows 3D representations of transverse strain distribution on the braids when experiencing three states of low tensile stresses at 20MPa, 40 MPa and 60 MPa. This figure shows that transverse strain fields on braids follow the yarn pattern of braids. Similar to the longitudinal strain distribution in Figure 3-11, Figure 3-16 shows that there is no significant transverse strain concentration on braids surface, which means no failure has occurred in composite constituents, and braids are behaving elastically until 60MPa of axial stress.

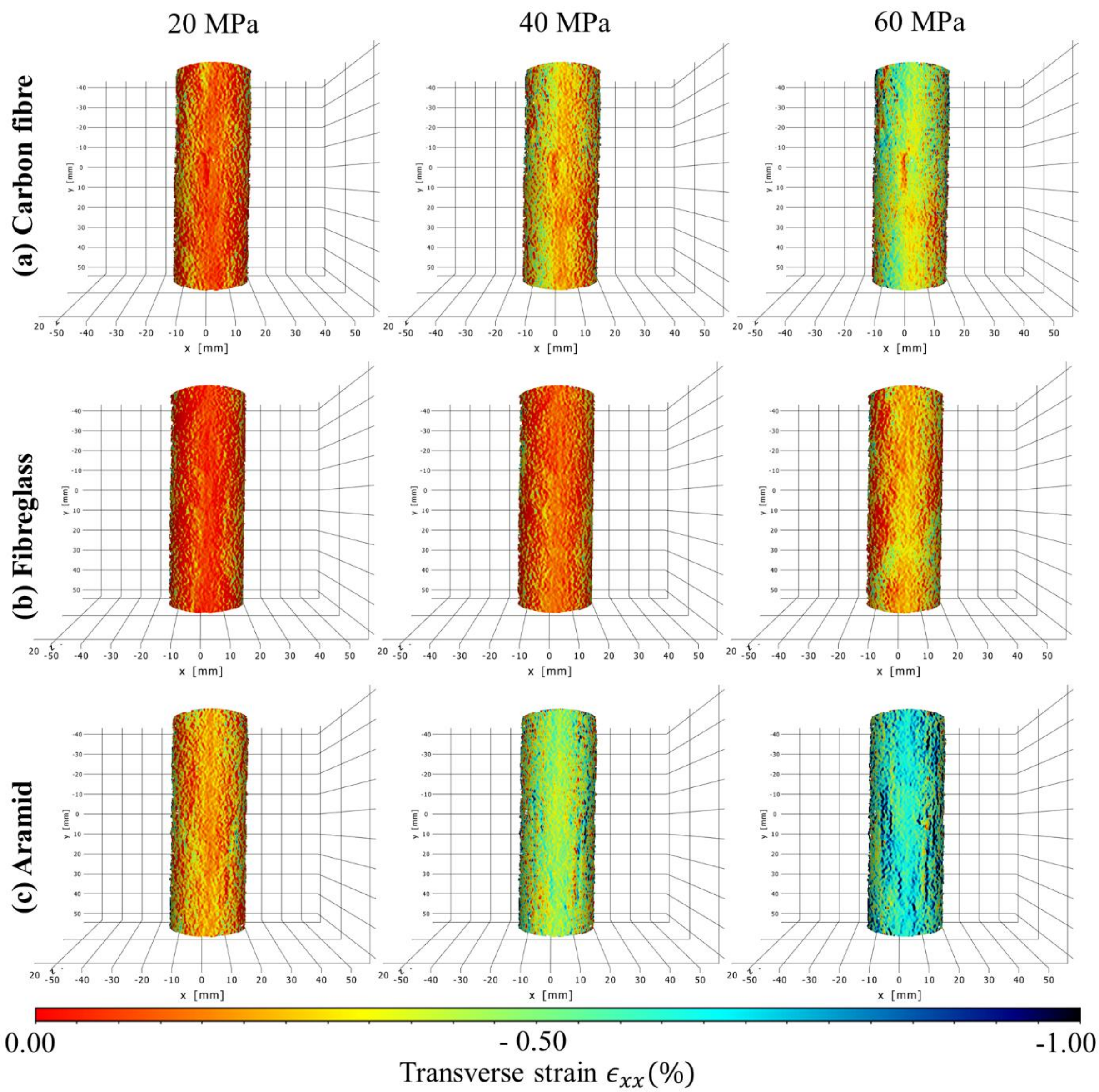

Figure 3-16: 3D representation of transverse strain distribution on three types of braids at low-stress states. Sample images show the three-dimensional strain distribution for the tubular braids (a) Carbon fibre (b) Fiberglass (c) Aramid. Sample stress of 20, 40 and 60 MPa are visualized.

3.3.4 $\epsilon_{xx} - \epsilon_{yy}$ curves and stiffness

The transverse strain versus longitudinal strain curves for all samples are shown in Figure 3-17. This figure is plotted for the elastic zone of the stress-strain curve of samples shown in Figure 3-12. The linear behaviour of the $\epsilon_{xx} - \epsilon_{\mathrm{yy}}$ curves indicate uniform deformation of samples during tensile test strokes for all the braids. A similar conclusion on $\epsilon_{xx} - \epsilon_{\mathrm{yy}}$ plots was stated in [103]. The uniform deformation of all samples indicates uniform epoxy resin impregnation to the fibres. The uniform distribution of matrix in braid preform demonstrates a consistent manufacturing technique was used to produce braids in this study.

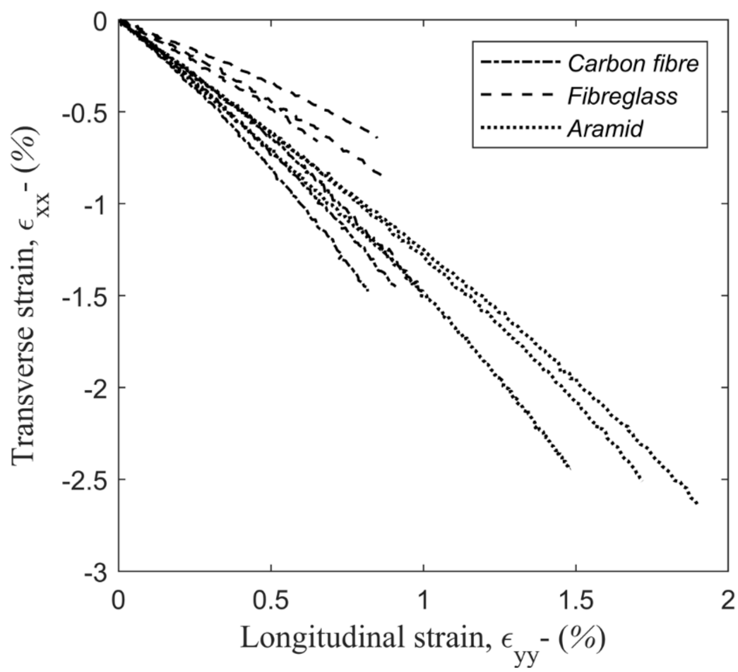

Figure 3-17: $\epsilon_{xx} - \epsilon_{yy}$ curves for carbon fibre, fibreglass and Aramid TBCs.

Figure 3-18 shows the plots of axial load versus crosshead displacement of the test frame for all samples in three different fibres. This figure is plotted for the elastic zone of the stress-strain curve of samples shown in Figure 3-12. Figure 3-18 shows that the load increases almost linearly with displacement for all the braids in the elastic deformation zone. The slope of this curve shows the axial stiffness of manufactured TBCs.

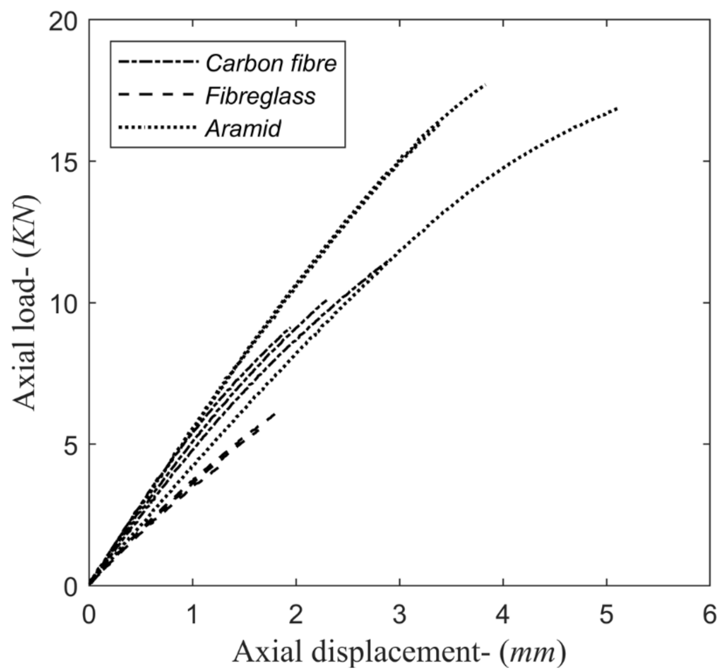

Figure 3-18: Axial load versus crosshead displacement for carbon fibre, fibreglass and Aramid TBCs.

Figure 3-19 shows the axial stiffness of three types of braids. The magnitude of axial stiffness for carbon fibre, fibreglass and Aramid braids are 4.67 KN/mm ± 0.38 KN/mm, 3.51 KN/mm ± 0.05 KN/mm and 4.67 KN/mm ± 0.86 KN/mm, respectively. The carbon fibre and Aramid braids showed almost equal axial stiffness and higher values than fibreglass braids. However, fibreglass braids showed very highly consistent behaviour for their stiffness magnitude.

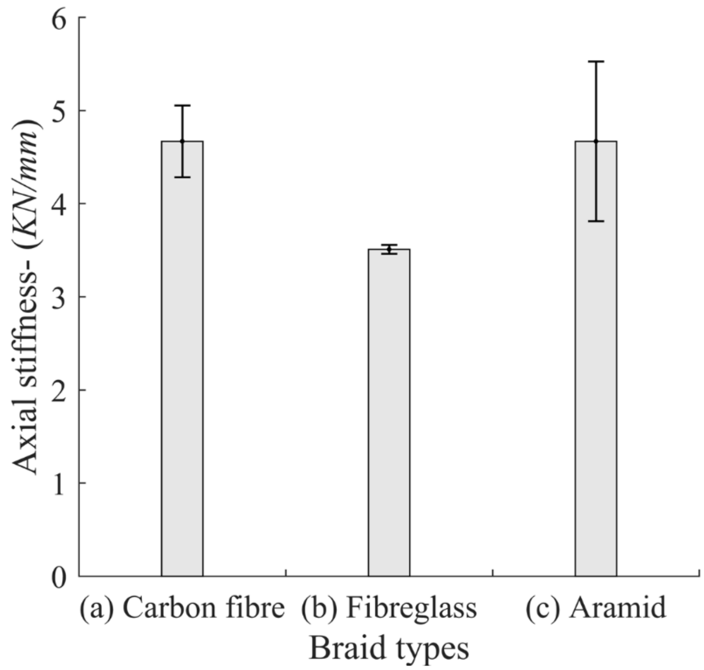

Figure 3-19: Axial stiffness for a) carbon fibre, b) fibreglass, and c) Aramid TBCs.

3.3.5 Failure analysis of TBCs in tension

The ultimate tensile strength, σ_{UTS}, for the three braids is shown and compared in Figure 3-20. The ultimate tensile strength is the stress that each sample failed and fractured into two separate pieces at the end of the test stroke. The magnitude of ultimate tensile strength for carbon fibre, fibreglass and Aramid braids are 344.37 MPa ± 4.48 MPa, 298.66 MPa ± 18.08 MPa and 367.30 MPa ± 51.81 MPa, respectively. Figure 3-20 demonstrate that Aramid braids have the highest ultimate tensile strength compared to carbon fibre and fibreglass braids. UTS for carbon fibre braid is higher than fibreglass braids. According to error bars in Figure 3-20, carbon fibre braids showed consistent values for ultimate tensile strength with minimal variation relative to Aramid and fibreglass ones.

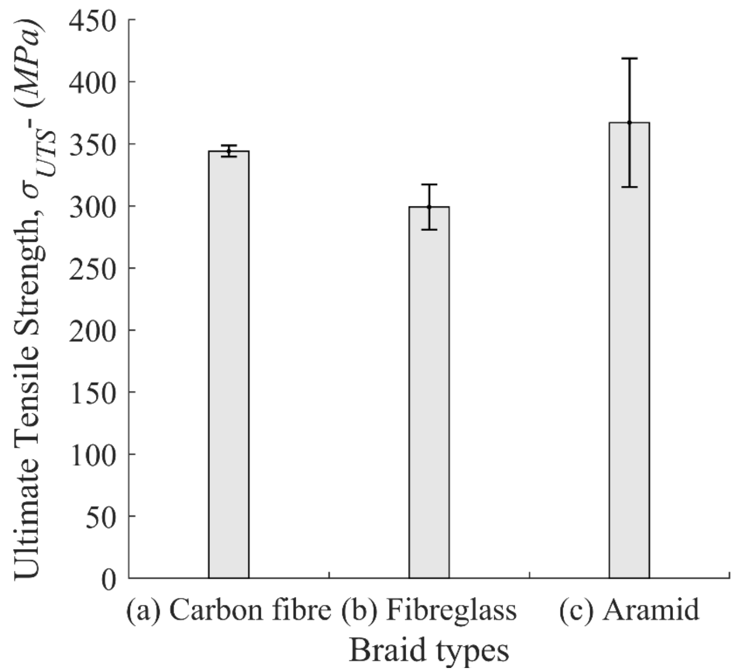

Figure 3-20: Ultimate tensile strength for a) carbon fibre, b) fibreglass, and c) Aramid TBCs.

Figure 3-21 demonstrates example DIC and raw images for carbon fibre, fibreglass and Aramid braids, respectively, at ultimate tensile strength and right after that when the failure occurs. According to these figures, failure occurs at locations where there are high axial strain concentrations. These figures show the significant benefit of the DIC technique that helps to easily measure the failure location and observe the strain concentration on loaded specimens; however, this observation is not possible using conventional measurement techniques such as strain gauges and extensometers. According to raw images shown in these figures, it is difficult to visually determine the exact failure location and fracture surface by examining the raw images alone.

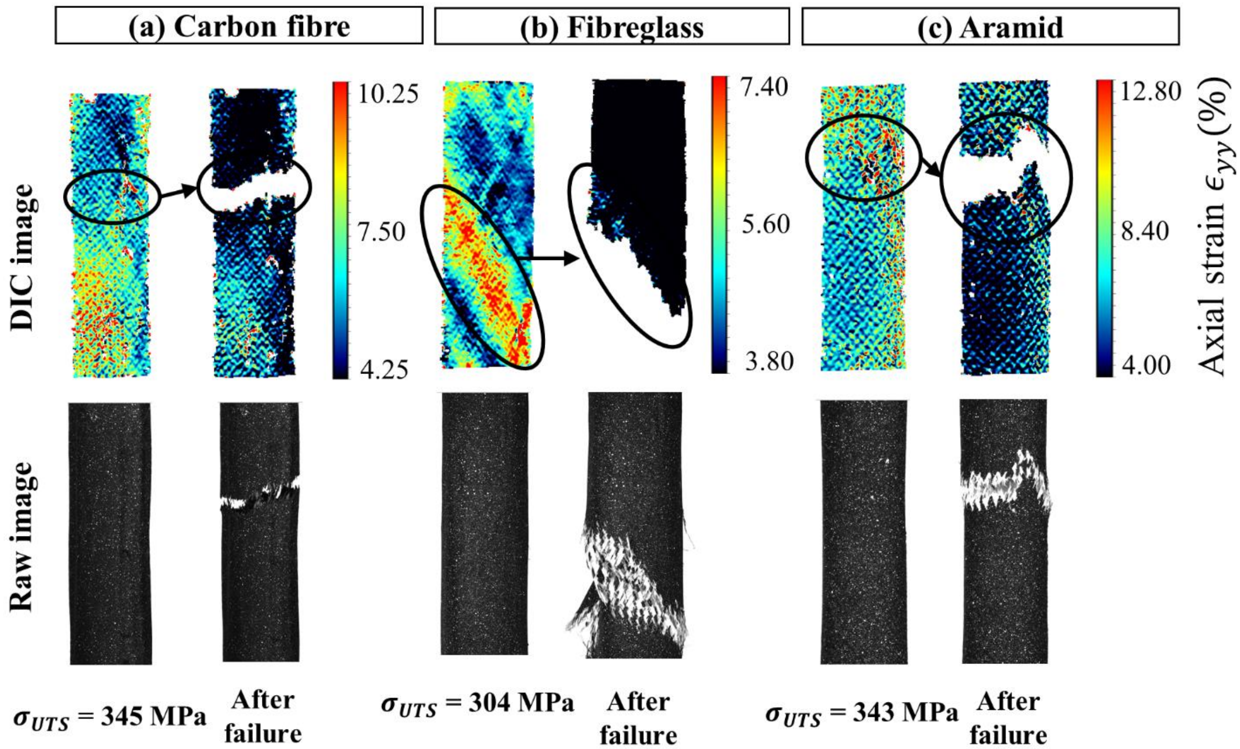

Figure 3-21: Example DIC and raw images for carbon fibre braid right before and after failure. DIC strain fields show the strain concentrations before failure at UTC.

Figure 3-22 shows the failure modes for all the nine carbon fibre, fibreglass and Aramid specimens. The failure codes used for these fractures are determined according to ASTM D3039 [115]. The failure code consists of three letters, the first letter stands for failure type, the second one stands for the failure area, and the last one shows the failure location. Two carbon fibre braids and all the Aramid braids had Lateral failure type. The fibreglass braids had an Angled failure type. All fibreglass and Aramid braids and two carbon fibre braids failed in the Gage area of the specimens and at the Middle location of braids. The other carbon fibre braid failed from the end tab epoxy. Therefore, its failure code is GIT, which means Grip/tab failure type, Inside grip/tab and the Top location of the braid. It is predicted that if the bonding were suitable for this carbon fibre braid, it would have the same LGM failure code as the other two carbon fibre braids. More details on failure codes are provided in [115]. According to mechanics of materials theory, brittle materials are inclined toward lateral failure type in tensile loading and ductile materials have angled failure type. Since axial stiffness is inversely related to ductility of materials, according to Figure 3-19, Fibreglass TBCs are more ductile than carbon fibre and Aramid TBCs. In other words, carbon fibre and Aramid braids have higher stiffness and more brittle characteristic than fibreglass braids. This argument agrees with the failure type of braids discussed in this section as fibre glass braids are showing angled failure type and other braids are showing lateral failure type.

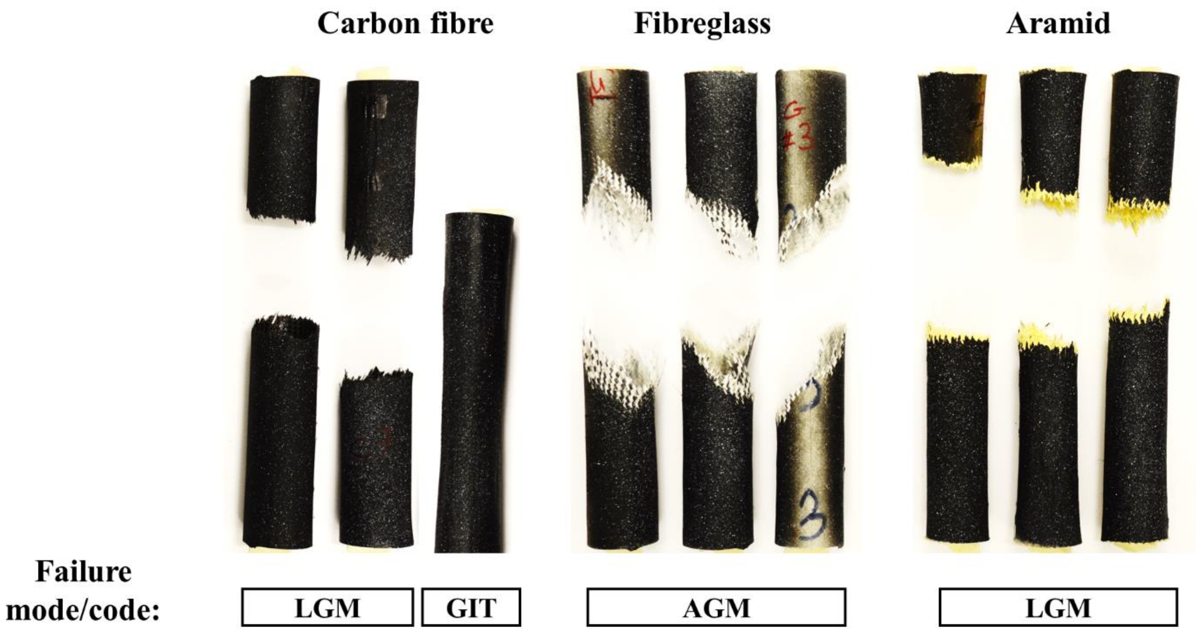

Figure 3-22: Images of all fractured specimens with their failure codes according to ASTM D3039. The failure code consists of three letters, the first letter stands for failure type, the second one stands for the failure area, and the last one shows the failure location. LGM: Lateral, Gage, Middle. GIT: Grip/tab, Inside grip/tab, Top. AGM: Angled, Gage, Middle.

3.4 Conclusions

This study investigated the mechanical behaviour of three different groups of TBCs under tensile loading. Each set of TBCs was produced using a single braid manufacturing technique but with three different fibres: carbon fibre, fibreglass and Aramid. 3D DIC strain measurement technique was used to study strain fields of TBCs and perform the surface reconstruction.

Initially, braid geometry and fibre volume fraction measurements were accurately assessed using physical and optical techniques. The accuracy of the DIC technique was verified by comparing braid outer diameter physical measurements with diameter measurements using DIC data. The maximum difference between measured outer diameters was 1.03% that was in an acceptable range based on literature.

Full-field longitudinal and transverse strain maps generated by the DIC technique were examined for low and high stresses for three different groups of braids. All braids exhibited elastic behaviour in low stresses between 20 to 60MPa by showing linear stress-strain curves and no significant strain concentration on their DIC results. Therefore, 40MPa axial stress can be selected as the tensile stress to preload carbon fibre, fibreglass and Aramid specimens for combined loading experiments in the next chapter. 40MPa tension is a load within the elastic limit of all manufactured TBCs for this research study. When loading exceeded 220MPa for carbon fibre and Aramid braids and 190MPa for fibreglass braids, significant strain concentrations became evident at some locations in DIC strain fields due to matrix failures. Utilizing the DIC measurement technique demonstrated that inhomogeneous strain maps exist in TBCs under loading. Strain patterns approved with the braid's interwoven structure. These observations explain the necessity of full-field strain measurement techniques to assess strain for TBCs.

Using averaged DIC strains, stress-strain curves and $\epsilon_{xx} - \epsilon_{\mathrm{yy}}$ plots were generated. By using the linear region of stress-stain curves, longitudinal elastic moduli were calculated for different braids. The moduli were 20.00 ± 0.95, 12.20 ± 2.65 and 13.90 ± 2.37 GPa for carbon fibre, fibreglass and Aramid braids studied in this work. Braids showed a linear behaviour for the $\epsilon_{xx} - \epsilon_{\mathrm{yy}}$ plots that indicated uniform deformation of all samples under loading. This uniform deformation indicates a consistent braid manufacturing technique was used in this study.

Axial stiffness and ultimate tensile strength for all braids were determined by assessing load and displacement outputs of the test frame. The determined axial stiffnesses were 4.67 ± 0.38, 3.51 ± 0.05 and 4.67 ± 0.86 KN/mm for carbon fibre, fibreglass and Aramid braids. The axial stiffness for carbon and Aramid braids were very close to each other. The magnitude of ultimate tensile strength for carbon fibre, fibreglass and Aramid braids were 344.37 ± 4.48, 298.66 ± 18.08 and 367.30 ± 51.81 MPa, respectively.

By reconstructing surfaces of braids using the DIC technique and plotting the surface profile in the middle of braids, the necking behaviour of different braids was demonstrated. Necking profiles were plotted at different loading states for three groups of braids. Necking occurs at a lower load for Aramid braids and at higher loads for fiber glass.

Finally, the fracture behaviour of TBCs was investigated. The braids all failed at locations where there was evident strain concentration in DIC strain fields. Taking advantage of DIC strain fields, observation of the failure location on braids was quite achievable, whereas it was almost impossible to do so using raw images of braids under loading. By observing fracture surfaces of braids, failure codes were generated using ASTM D3039 guideline. Aramid and most of the carbon fibre braids had a failure code of LGM, and the fibreglass braids were assigned to the AGM failure code.

Chapter 4 Combined loading experiment on tubular braided composites

4.1 Introduction

Composites materials are utilized for their high strength to weight ratio in industries that require high-performance components [2]–[4]. However, conventional composite laminates suffer from relatively low toughness and delamination. Moreover, the laminate manufacturing process is costly and time-consuming [6], [7]. In contrast, braided composites have modified characteristics that overcome technical challenges created by conventional laminated composites. Braided composites are a composition of continuously interlaced fibres in a resin epoxy matrix. Braided preforms are produced with an automated braiding process. The interwoven nature of braided composites results in damage tolerance and structural stability [2], [8]. Utilizing lightweight fibres and benefiting from braiding technology as a time and cost-efficient manufacturing method reduces carbon dioxide emissions and answers the increasing demand for high-performance structures such as jet engine stator vanes, fan blades and shafts [2], [9]–[13].

The braided composites typically are produced in tubular cross-section and can be utilized to fabricate axisymmetric parts. Therefore, the evaluation of braided composites in the tubular configuration is required under loading [14], [15]. 2D braid preforms are formed from the interlacement of yarns around a mandrel with Maypole or radial braiding machines [9], [16]. Regular (2/2) patterns are the most common pattern used for manufacturing braids, which is similar to a twill weave for textile composites, though, in bias direction [18]. Different types of fibres have been used for braided composite manufacturing [2]. The most common fibres for manufacturing braided composites are carbon fibre, fibreglass and Aramid [19].

Braided composites are becoming more widely adopted for industrial applications; therefore, understanding their mechanical behaviour under various kinds of stress states is crucial to avoid premature failure [14]. Independent studies of 2D tubular braided composites (TBCs) under tension and torsion loadings have been investigated by several researchers [7], [8], [20]–[24]. For example, Harte and Fleck investigated fibreglass TBCs to understand and model their deformation and fracture responses in various braiding angles under tensile loading [7]. They found that for TBCs, failure occurs due to fibre fracture for small braid angles, and braid fails because of neck propagation for large braid angles. They used conventional strain gauges to measure deformations.

In another work by Harte and Fleck, they studied a regular fibreglass TBC to explore the failure modes for different braid angles under various types of loadings with a minor focus on combined tension/torsion loading [21]. They used conventional strain gauges to perform measurements without any discussion on strain distribution over the braid. Chai *et al.* conducted a comprehensive study on a carbon fibre TBCs in torsion loading using X-ray computed tomography (CT) imaging to explore the extent of the damage mechanism of braided structure [23]. Intra-tow cracks and inter-tow debonding were observed at a low shear strain of 1.5%. The area fraction of inter-tow debonds was significantly increased for shear strains beyond 1.5%. For shear strains higher than 2.0%, the volume fraction of intra-tow cracks was found to proliferate. Fibre micro-buckling and kink band were observed at shear strains of 2.5% that occurred for stresses over the peak shear stress. Presently, 2D TBCs under tension and torsion loading have been studied individually. There are research works that have investigated other types of composites under simultaneous tension and torsion loading [100], [101]. Yu *et al*. experimentally investigated a needled composite under coupled tension-torsion loading [100]. Amijima *et al.* conducted static and fatigue mechanical tests for woven glass fabric composite under biaxial tension-torsion loading [101]. Braided composite components frequently experience combined tension-torsion loading while in operation; however, few studies have investigated the mechanical properties of braids due to the effect of combined loading.

Deformation measurements of braided composites under loading have been performed using different techniques. Many researchers have used a conventional technique such as strain gauges and extensometers for evaluating deformations [6], [7], [21], [100]. However, recently scholars [98], [102]–[105] have turned into the use of digital image correlation (DIC) as a contact-free full-field measurement technique that does not have the limitation regarding material type and specimen size [106]. This technique is called either 2D DIC if the measurement is performed using a single camera or 3D DIC if multiple cameras do the imaging for measurements. 2D DIC is applicable for full-field strain measurements for flat specimens [107], [108]. For TBCs, 3D DIC is preferred as the braids have wavy surfaces and curved structures; therefore, in-plane and out of plane displacement measurement is required [14]. 3D DIC measurement technique is preferred over conventional discrete measurement methods such as strain gauges since it can process strains over multiple unit cells [8], [20]. Leung *et al.* used 3D DIC to see how nominal diameter and braid angle changes during tensile test stroke by examining full-field unit cell strain and surface reconstruction of Aramid TBCs [20]. According to their investigations, the changes in braid angle and braid radius in the tensile experiment could affect the calculated elastic modulus by about 10%. Melenka *et al.* thoroughly used the 3D DIC technique to examine the effect of braid angle and braid pattern on the mechanical properties of Aramid TBCs under tension and torsion loadings [8]. Their tensile experimental results demonstrated that, for the same braiding pattern, longitudinal elastic modulus and maximum stress values for specimens with smaller braiding angles are significantly higher than of values for larger braiding angles. Moreover, for the same braiding angle, the longitudinal elastic modulus and maximum stress magnitude for regular braiding patterns were higher than the values for braids with diamond patterns. Their torsion experimental results did not show any distinct relation between braid angle and pattern to the shear moduli and maximum shear strength of braids. Bruni-Bossio *et al*. used the 3D DIC technique to study the effect of braid angle on tensile properties of TBCs manufactured by cellulose fibres with bio-based resins [24]. They compared the elastic modulus of their samples to the moduli of similar braids with synthetic materials. They suggested that their manufactured cellulose fibre braids and Ecopoxy resin could be a suitable replacement for E-glass braids for high stiffness to weight ratio applications. 3D DIC technique is also applied for studying TBCs under bending. Can *et al.* conducted a novel study on flexural properties of natural fibre TBCs under a three-point bending load. They used 3D DIC for strain measurements and micro-computed tomography (μCT) for braid structure analysis. Currently, 3D DIC measurements to study TBCs under combined loading has not been performed.

This study aims to investigate the mechanical behaviour of TBCs under combined tension/torsion loading. Mechanical properties of carbon fibre, fibreglass and Aramid TBCs are assessed as a case study. 3D DIC measurement technique is utilized to examine elastic and failure strain fields and buckling behaviour of braids. The failure mechanism of braids is investigated by the plane stress theory of mechanics of material. Stiffness magnitudes are compared for different braids with different types of fibre. The results presented in this case study can be used for evaluating numerical and analytical models for predicting TBCs mechanical behaviour under combined loading.

4.2 Experimental methods

4.2.1 Sample manufacturing

Find related information in the methodology section of Chapter 3.

4.2.2 Specimen geometry measurement

Find related information in the methodology section of Chapter 3.

4.2.3 Mounting specimens on tabs

Find related information in the methodology section of Chapter 3.

4.2.4 Sample mechanical testing

Carbon fibre, fibreglass, and Aramid TBCs were evaluated in combined loading to investigate their strain behaviour, failure mechanism, buckling trend and stiffness characteristic. Three samples were evaluated for each braid type. The axial/torsional test frame (809 MTS Systems Corporation, USA) shown in Figure 3-5 was used to perform mechanical tests. Force and torque data were measured using a 100KN axial load and 1100N-m torque capacity load unit (Model number: 319.10, MTS Systems Corporation, USA). Force, torque, displacement, and rotation data were recorded using the test frame's data acquisition system.

The combined loading test consisted of two loading steps. In the first step, each specimen was axially loaded with a constant rate of 1 KN/min as per [15] to reach 40GPa tension stress. In the second step, the lower crosshead of the test frame begins applying torque load with a constant rotation speed of 0.01°/s until 18° of rotation. In this step, using the load control mode of test frame, 40MPa tensile stress on braids was maintained from the first step. Loading steps are demonstrated in Figure 4-1. The 40MPa pre-stress value was determined by studying the stress-strain curves of pure tension tests on completely similar manufactured TBCs and picking a tensile stress value with a factor of safety of two to ensure that all braid types will be within the uniaxial elastic limit while applying torsional load in the experiment. Preloading samples to the same amount of axial stress rather than axial force that was the method used in [15] allows the comparison of the mechanical response of braids in the combined loading test. Therefore, carbon fibre, fibreglass and Aramid TBCs are compared against each other based on their behaviour in the torsion loading step while each specimen is experiencing identical 40MPa tensile stress.

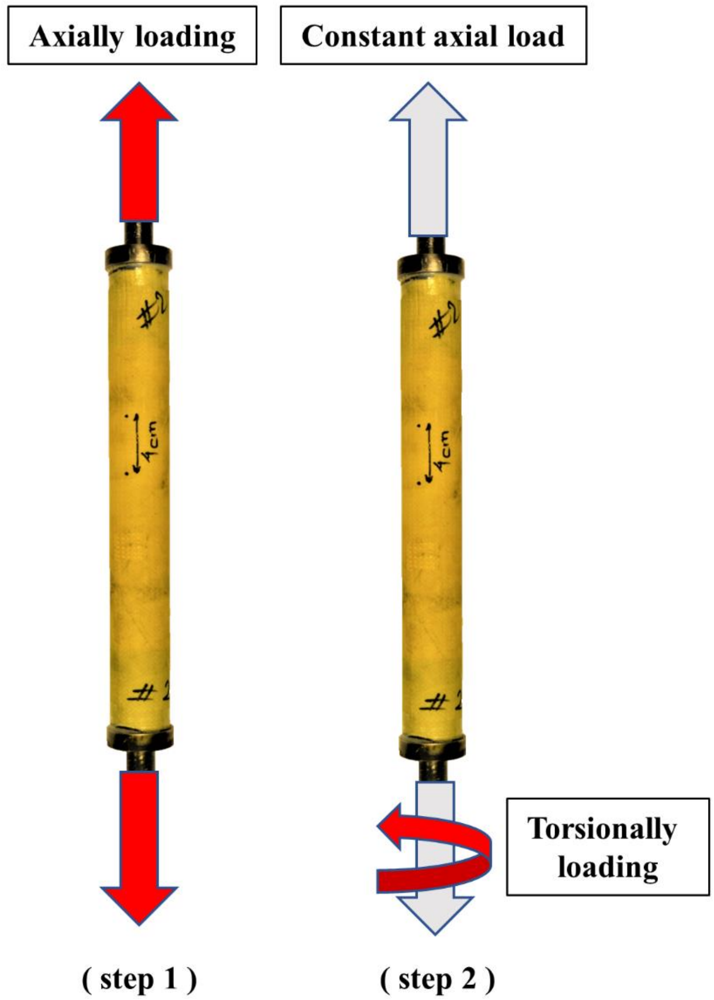

Figure 4-1: Loading steps of combined loading experiment. In step 1, the braid is axially loaded to 40MPa with a rate of 1 KN/min. In step 2, while the braid is under constant 40MPa stress, torque is applied with a crosshead rotation speed of 0.01°/s until 18° of rotation.

4.2.5 Deformation measurement

Deformation measurement configuration used for combined loading experiments is similar to what was used for tensile loading experiments. The summary of the imaging setup configuration is listed in Table 4-1. The image acquisition rate was 1Hz for tensile loading experiments and 2Hz for the combined loading tests. The difference in image acquisition rate is due to different speeds of tests and the time length of the experiments.

Table 4-1: Image acquisition setting.

Digital image correlation parameters	Settings
Camera Resolution	2464×2056 pixels
Camera Pixel Size	3.45 µm
Digital output	12 bit
Camera Lenses	2X Navitar 50mm lens
Distance Between Cameras and Specimen	850 mm
Stereo Angle of Cameras	17°
Camera Field of View (FOV)	115×94 mm^2
Image Acquisition Rate	2 Hz

4.2.6 DIC Sample preparation

Find related information in the methodology section of Chapter 3.

4.2.7 3D DIC processing and post-processing

A least-square optical flow displacement measurement algorithm was used to drive displacement vector fields using DIC processing software [116]. A subset window size of 21×21 pixels and a step size of 7 pixels were used to perform a correlation between images. The DIC analysis parameters are summarized in Table 4-2.

Table 4-2. Digital image correlation settings.

DIC parameters	Settings
Image Scale Factor	21 pixels/mm
Correlation Subset Size	21 × 21 pixels
Correlation Step Size	7 pixels

4.2.8 Principal planes of braid

According to the mechanics of materials theory, since the braids examined in this study are thin-walled tubes and $\sigma_z = \tau_{zx} = \tau_{zy} = 0$, the state of plane stress is assumed to exist in this study [25], [122], although the TBC structure is non-isotropic. According to these assumptions, principal planes and stresses of TBCs under combined loading are investigated in this work.

Figure 4-2-(i) shows a representative element of braid oriented in x-y coordinates under combined tension/torsion loading at point Q. This figure illustrates that the braid element is experiencing positive longitudinal stress in the y-direction, σ_y, which is constant and equal to 40MPa during the rotational step of the combined loading experiment. Figure 4-2-(i) also shows negative shear stress, τ_{xy}. The negative sign of shear stress is due to direction of applied torque from the lower crosshead. Figure 4-2-(ii) shows the same element oriented in principal planes. The principal planes of stresses at point Q are the planes of θ_{P_1} and θ_{P_2} obtained from Equation 4-1.

$$\theta_{P_{1,2}} = \frac{tan^{-1}(\frac{2\tau_{xy}}{\sigma_x - \sigma_y})}{2} \qquad 4\text{-}1$$

The principal planes are 90º apart from each other so that $\theta_{P_2} = \theta_{P_1} + 90°$. These planes contain the faces of the element.

Figure 4-2- (ii) also shows principal stresses, σ_1 and σ_2, which are acting perpendicular to element faces and along with principal directions of 1 and 2. When the representative element is in the orientation of principal planes, only two axial stresses, σ_1 and σ_2, are exerted on the faces of the element. The element experiences no shear stress when it is rotated to principal planes since plane stress condition is dominating. From Equations 4-2 and 4-3, the magnitude and sign of principal stresses along principal directions of 1 and 2 are determined. In these two equations, transverse stress, σ_x, is not included since it is zero at all time as there was no load exerted to the specimen in the horizontal direction.

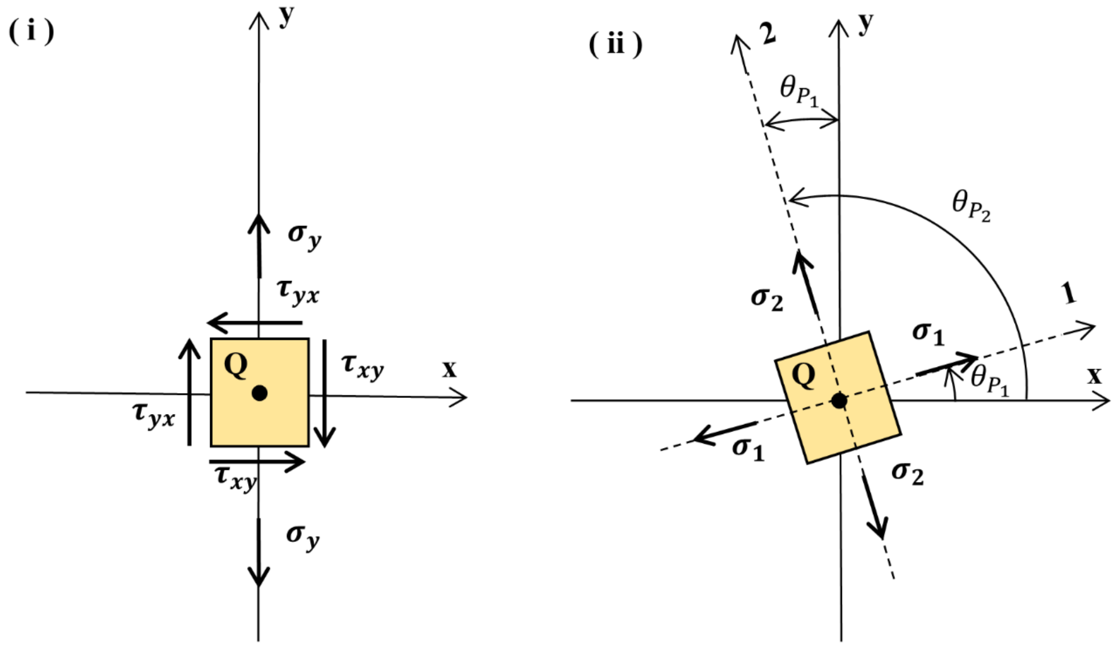

Figure 4-2: Representation of a braid element Q under loading. Figure (i) shows the stresses on the braid element oriented in x-y coordinates. Figure (ii) shows the same element of the figure (i) oriented in principal directions and their corresponding principal stresses.

$$\sigma_1 = \frac{\sigma_y}{2} - \frac{\sigma_y}{2} \cos 2\theta_{P_1} + \tau_{xy} \sin 2\theta_{P_1} \qquad 4\text{-}2$$

$$\sigma_2 = \frac{\sigma_y}{2} + \frac{\sigma_y}{2} \cos 2\theta_{P_1} - \tau_{xy} \sin 2\theta_{P_1} \qquad 4\text{-}3$$

4.3 Result and discussion

4.3.1 Braid geometry analysis

The inner (D_i) and outer (D_o) diameters of manufactured TBCs were physically measured using a high accuracy micrometer. The physical diameter measurements were used to determine stress calculations. Braid angle (θ_b) was accurately measured using a high-resolution camera equipped with a macro lens and ImageJ software. Yarn width (W_y) was also optically measured using a similar technique for braid angle measurement. The average value and the standard deviation (Std Dev) for inner diameter, outer diameter, braid angle, and braid yarn width measurements are listed in Table 4-3. Inner diameters of braids were considered as the outer diameter of the mandrel and had minimal variation due to the perfect surface finish of mandrel. The braid angles for all three groups of manufactured specimens are close to each other, with values of 32.05º ± 0.72º.

Having densities from Table 3-1 and Table 3-2 and using measured fibre mass (m_f) and matrix mass (m_m) listed in Table 4-3, fibre volume, V_f, and matrix volume, V_m, were calculated using Equations 4-4 and 4-5. In these equations, ρ_f and ρ_m are the fibre and matrix densities, respectively. Using calculated fibre (V_f) and matrix (V_m) volumes, fibre volume fraction (v_F) measurements were performed using Equation 4-6. The averaged fibre volume fraction with its standard deviation for three group of braids is summarized in Table 4-3. According to [2], the v_F for typical laminates is between 50% to 70% and can be lower for braided composites. The v_F measured for the manufactured braids in this study are lower than 42% which agrees with the expectations in [2].

$$V_f = \frac{m_f}{\rho_f} \qquad \text{4-4}$$

$$V_m = \frac{m_m}{\rho_m} \qquad \text{4-5}$$

$$v_F = \frac{V_f}{V_f + V_m} \qquad \text{4-6}$$

Table 4-3. Average measured properties with ± standard deviations for manufactured braids.

Braid type	Inner diameter (mm) $\boldsymbol{D_i}$	Outer Diameter (mm) $\boldsymbol{D_o}$	Braid angle (degree) $\boldsymbol{\theta_b}$	Braid yarn width (mm) $\boldsymbol{W_y}$	Fibre mass (g) $\boldsymbol{m_f}$	Matrix mass (g) $\boldsymbol{m_m}$	Fibre volume fraction (%) $\boldsymbol{v_F}$
Carbon 3K	38.08 ± 0.00	39.05 ± 0.04	32.48 ± 0.93	1.53 ± 0.12	12.72 ± 0.01	15.72 ± 1.6	34.03 ± 2.37
Fiberglass	38.08 ± 0.00	39.05 ± 0.06	30.83 ± 1.13	1.40 ± 0.06	17.97 ± 0.01	14.70 ± 1.85	34.72 ± 2.98
Aramid (Kevlar 49)	38.08 ± 0.00	39.67 ± 0.33	32.83 ± 0.11	1.71 ± 0.06	17.67 ± 0.05	19.73 ± 2.54	41.01 ± 3.30

The outer diameter of braids was also calculated using surface height data extracted from DIC results. A similar approach was performed by Leung *et al.* [118]. Using a circle fitting function [119], five circles were fitted on surface height data to get five outer diameter measurements for each braid. Figure 4-3 shows an example fitted circle on DIC height data. In this figure, the reconstructed surface from DIC data has formed a semicircle and is shown by line (i). Line (ii) in this figure shows the fitted circle on DIC data of line (i). The diameter of this fitted circle was considered as the outer diameter of braid measured from DIC results.

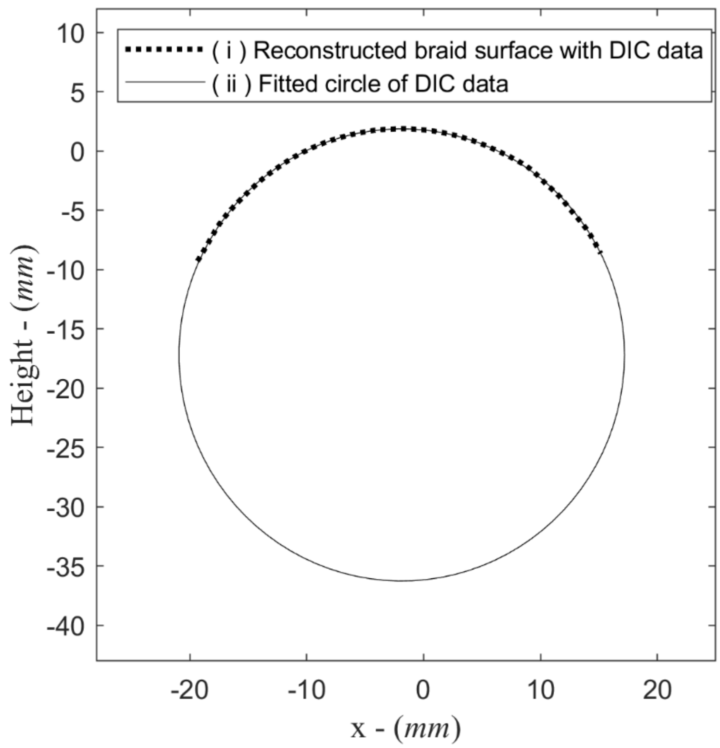

Figure 4-3: An example of outer diameter measurement of the braid using circle fitting on DIC result.

For validating the accuracy of DIC measurements, the fitted outer diameter measurements were compared with physically measured outer diameters with the micrometer. This comparison indicates that stereo cameras were correctly placed and calibrated and ensures that strain and displacement measurements with DIC technique has high accuracy. A similar comparison for DIC accuracy validation was made in [8]. Table 4-4 shows the comparison of outer diameters between physically and optically measurement techniques. This table demonstrates a good match between the measurements. 1.60% is the maximum difference between physically and fitted outer diameter for the braids. The acceptable agreement between physically measured diameters and the diameters from the fitted circle on DIC height data states that the 3D DIC technique was accurate and well-calibrated for all the experiments; therefore, the resulting strain fields of DIC measurement are reliable. According to Table 4-4, the standard deviation values for diameters of the fitted circles are meaningfully higher than those measured with the micrometer. The main reason is the precision of high-quality images captured with the DIC technique with high-resolution cameras. These images fully account for the waviness surface of braided composites due to yarn interlacement, while the micrometer cannot reflect the nonhomogeneous surface of the braid. Therefore, extracted height data from 3D DIC measurements show variation due to the nature of braid's surface structure and results in a larger magnitude for standard deviations of fitted diameters than the diameters measured physically.

Table 4-4. Comparison of braid specimen outer diameters measured using physical technique and fitted surface height data of DIC results.

Braid type	Physically measured $\boldsymbol{D_o}$ (mm)	St Dev of physically measured $\boldsymbol{D_o}$ (mm)	$\boldsymbol{D_o}$ of the fitted circle using DIC height data (mm)	St Dev of $\boldsymbol{D_o}$ of the fitted circle using DIC height data (mm)	Difference (%)
Carbon 3K	39.05	0.04	38.18	0.14	1.12
Fiberglass	39.05	0.06	38.21	0.31	1.08
Aramid (Kevlar 49)	39.67	0.33	38.42	0.12	1.60

4.3.2 Strain behaviour

Nine TBCs (three Aramid, three fibreglass, three carbon) were subjected to combined tension/torsion loading. All the braids were preloaded to 40MPa axial stress. 40MPa tensile stress was a load that all the braids behaved elastically since it was a stress magnitude in the linear region of stress-strain curves of all nine braids. After preloading axially to 40MPa, braids were twisted in rotational control mode that caused shear stress, τ_{xy}, and shear strain, ϵ_{xy}, in braids.

Shear stress on braids was determined using Equation 4-7. In this equation, T is the applied torque on braids measured by the test machine controller, D_i is the inner diameter and D_o is the outer diameter of braids that were measured using a micrometer. Shear stress is plotted versus torsional angle, θ_T, in Figure 4-4 when the torsional angle increases at a constant rate from 0° to 18°. The negative sign of shear stress is due to the direction of applied torque from the lower crosshead. As plots in Figure 4-4 shows, the magnitude of shear stress initially increases linearly in all types of braids as the crosshead is rotating. After a few degrees of rotation from the lower crosshead, the linear region of plots for all braids ends sharply at different magnitudes of shear stress. In this study, the failure of braids in combined loading is considered at the end of the linear region displayed in Figure 4-4 and the maximum shear stress, τ_{max}, is considered the shear stress corresponding to this point. The maximum shear stress for braids under combined loading is compared using bar plots shown in Figure 4-5. In this figure, the error bars are the standard deviation of each data set. The maximum shear stress for carbon fibre, fibreglass and Aramid braids are -48.81MPa ± 10.83MPa, -38.84MPa ± 5.81MPa and -51.16MPa ± 3.06MPa, respectively. The carbon fibre and Aramid braids showed almost equal maximum shear stress and higher magnitudes than fibreglass braids.

$$\tau_{xy} = \frac{32\ T\ D_o}{\pi\ (D_o^4 - D_i^4)} \qquad 4\text{-}7$$

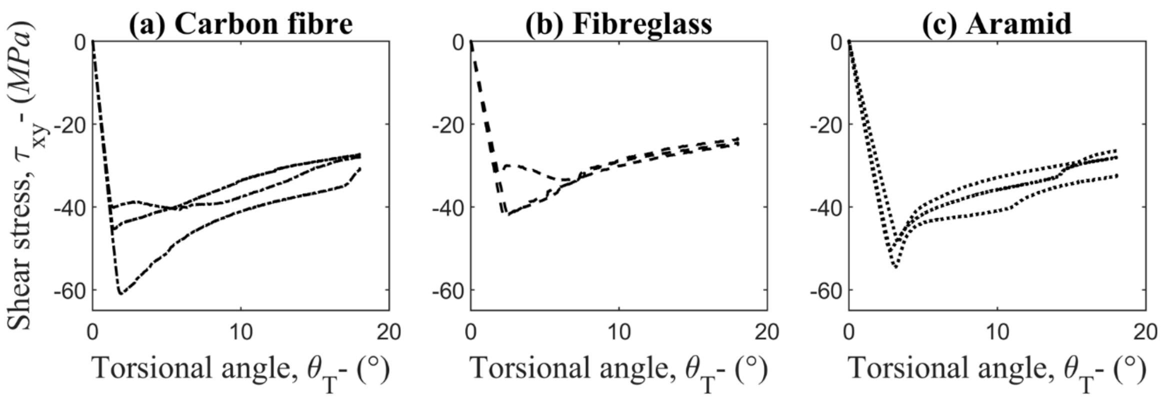

Figure 4-4: The relation between induced shear stress, τ_{xy}, while torsional angle, θ_T, increases on the tubular braids (a) Carbon fibre (b) Fiberglass (c) Aramid. The first sharp drop of these curves is considered as the maximum shear stress, τ_{max}.

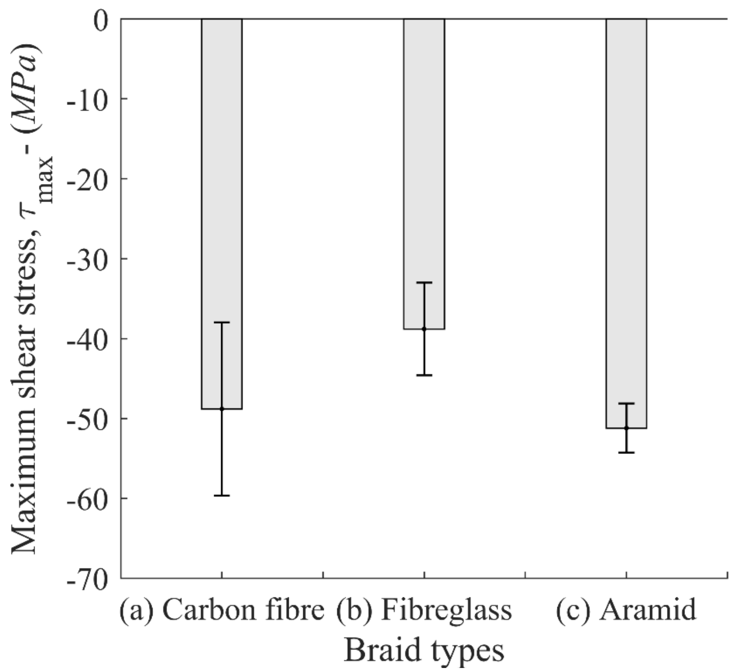

Figure 4-5: Comparison of maximum shear stress, τ_{max}, for tubular braids (a) Carbon fibre (b) Fiberglass (c) Aramid.

The shear strain, ϵ_{xy}, was determined using the equation:

$$\epsilon_{xy} = \epsilon_{yx} = \frac{1}{2}\left(\frac{\partial u}{\partial y} + \frac{\partial v}{\partial x}\right) \qquad 4\text{-}8$$

where u and v represent the displacement vector fields measured using the 3D DIC strain measurement technique in x and y directions, respectively. Figure 4-6 represents example 2D images of shear strain distributions on the surface of carbon fibre, fibreglass and Aramid braids while experiencing combined loading. Figure 4-6- (i) shows the shear strain on braids at every increase of 5MPa in shear stress magnitude beginning from -5MPa to -30MPa for all braids. Figure 4-6- (ii) shows the strain distribution of braids at maximum shear stress (τ_{max}) where braid failure occurs. According to this figure, braids are experiencing non-uniform shear strain distribution due to the undulating structure of braided composites. Figure 4-6 also demonstrates the shear strain variations corresponding to the dark horizontal line in the middle of the braids at maximum shear stress. These strain variations show significant fluctuating strains along the dark line. According to these strain variations, it is observed that the shear strain period corresponds to the period of braid yarns. Similar observations were seen in a 3D DIC study by Melenka *et al.* [8] on TBCs examined in torsion loading.

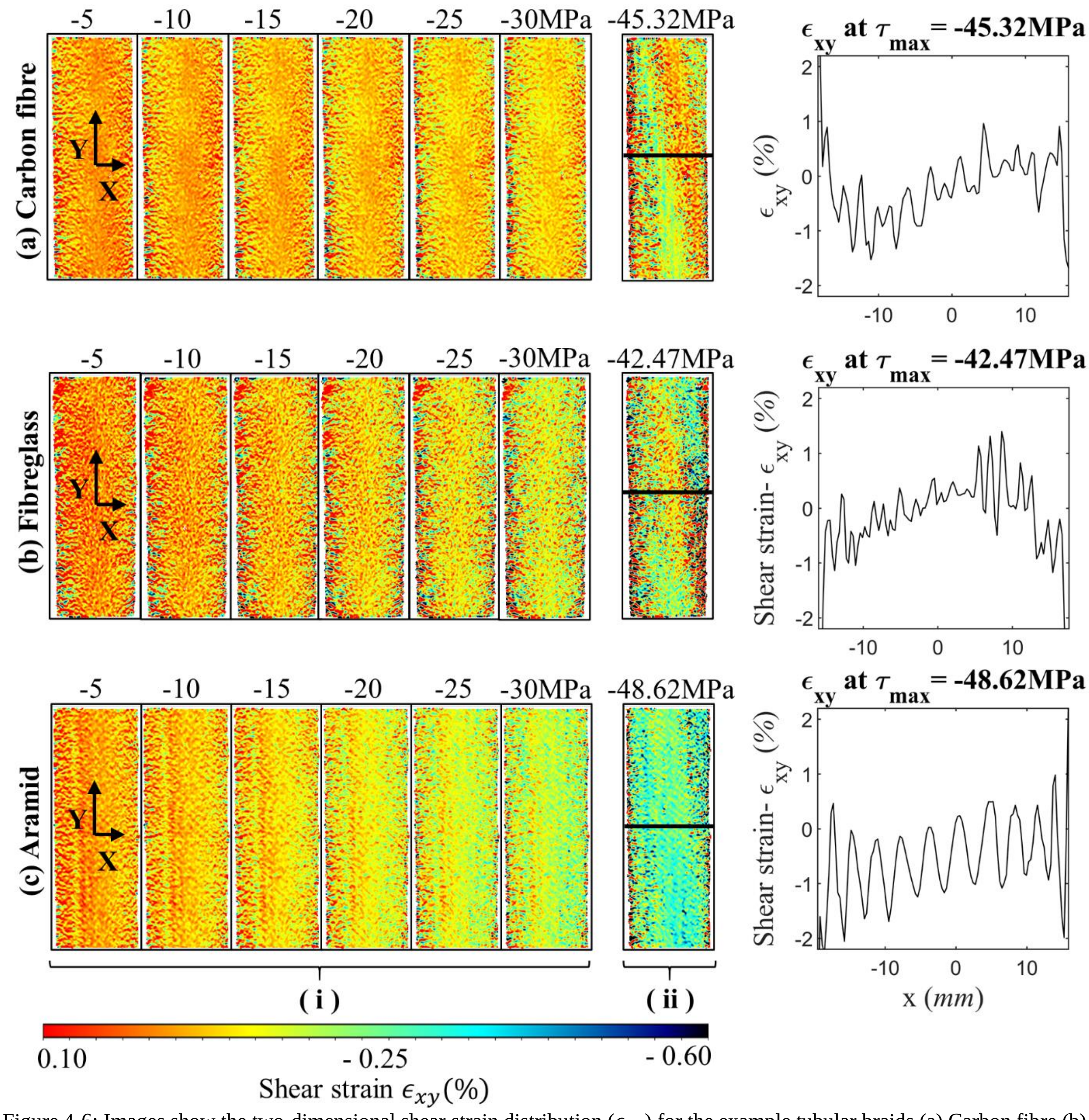

Figure 4-6: Images show the two-dimensional shear strain distribution (ϵ_{xy}) for the example tubular braids (a) Carbon fibre (b) Fiberglass (c) Aramid. i) shows colour map shear strain on braids for stress range of -5 MPa to -30 MPa with increasing steps of -5 MPa. ii) shows colour map shear strain on braids at maximum shear stress (τ_{max}) values. Shear strain distribution at maximum shear stress along the horizontal dark line at the middle of samples is also plotted.

4.3.3 Failure analysis of TBCs in combined loading

Figure 4-7 shows how the first principal plane angle, θ_{P_1}, changes during the rotation of crosshead, θ_T. According to Figure 4-4 and Figure 4-7, the first principal plane angle keeps increasing linearly for different braids as the crosshead is rotating, and shear stress is linearly increasing on braids. Considering Figure 4-4 and Figure 4-7, the linear increase of the first principal plane angle ends when the braid experiences its maximum shear stress. The maximum angle of the first principal plane before the sharp drop of curves in Figure 4-7 is called the maximum principal plane angle, $\theta_{P_{max}}$. It should be reminded that the second principal plane angle (θ_{P_2}) behaves same as the first plane but with a shift of 90°, thus it is not plotted and compared.

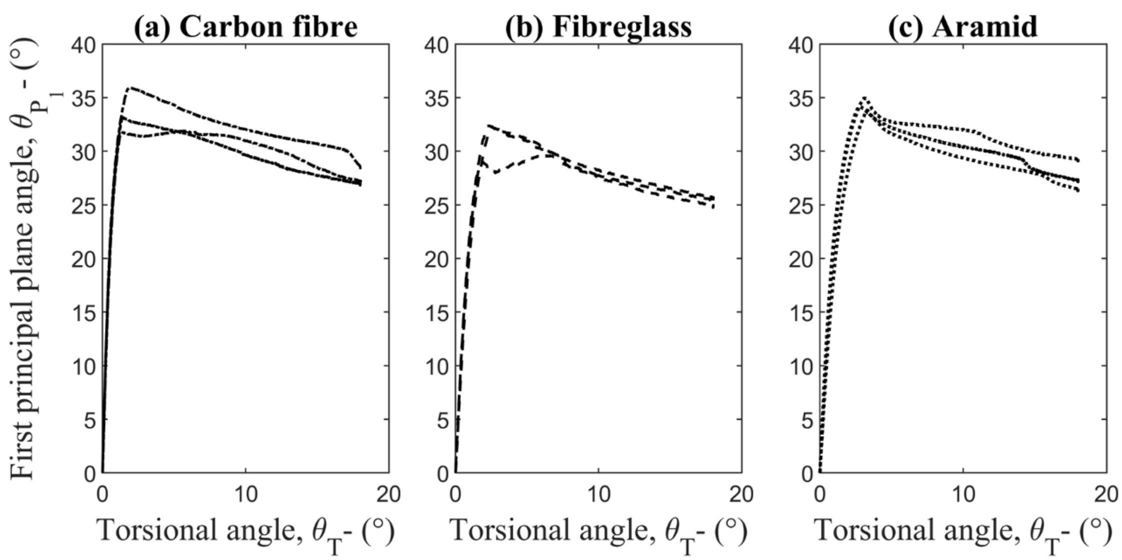

Figure 4-7: Changes in the first principal plane angle (θ_{P1}) while torsional angle increases for the tubular braids (a) Carbon fibre (b) Fiberglass (c) Aramid.

The maximum principal plane angle is compared to the braid angles of TBCs using bar plots in Figure 4-8. The average maximum principal plane angles are 33.60° ± 2.11°, 31.22° ± 1.89° and 34.30° ± 0.58° for carbon fibre, fibreglass and Aramid braids, respectively. Braid angles are listed in Table 4-3 for different groups of braids. According to Figure 4-8, the braid angle of braids is very close, but a few degrees lower than the maximum principal plane angle for all three groups of specimens. To explain this difference, it must be reminded that the braid angle plotted in Figure 4-8, which is the angle between yarn direction and the longitudinal direction of braid, was measured when the braids were in unloaded condition. However, the braid yarns under combined loading are straightened in the preloading stage of the experiment and then tilted for a few degrees when the braids are experiencing their maximum shear stress because of the crosshead rotation. According to Figure 4-7, at the maximum principal plane angle, lower crosshead has rotated 1.60° ± 0.28°, 2.22° ± 0.39° and 3.07° ± 0.25° for carbon fibre, fibreglass and Aramid braids, respectively. This straightening and tilting results in a few degrees increase in the braid angle when the braid is at maximum shear stress under combined loading. This increase in braid angle due to straightening and tilting is overlooked in the comparison made in Figure 4-8 as the braid angles were measured prior to sample loading. Performing braid angle measurement is not possible when braids are under loading because the braids are painted and speckled for DIC measurement purposes. Thus, if the effect of loading on the final orientation of yarns was measured, the new braid angle of loaded braids is anticipated to be almost the same as the maximum principal plane angle, not a few degrees lower than it. Therefore, it can be argued that at $\theta_{P_1} = \theta_{P_{max}}$, θ_{P_1} is equal to θ_b.

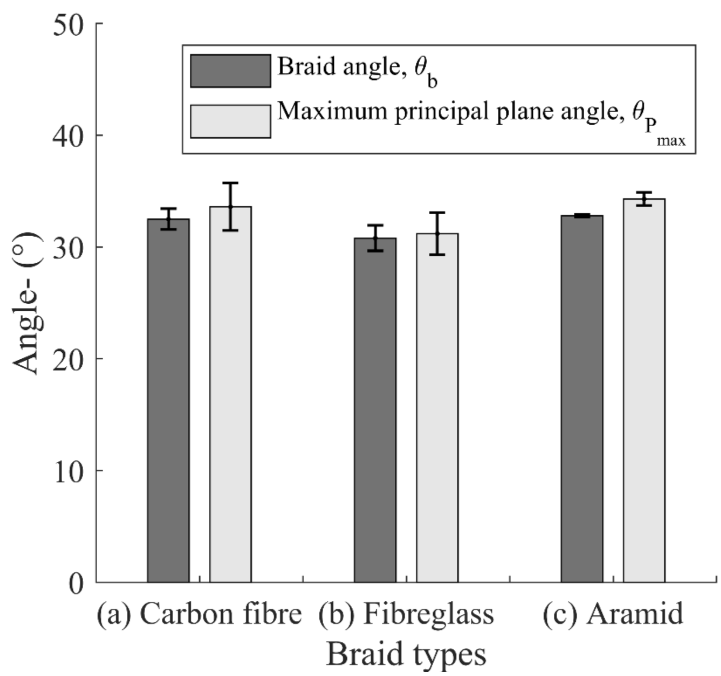

Figure 4-8: Comparison of the braid angle (θ_b) with the maximum principal plane angle (θ_{Pmax}) for the tubular braids (a) Carbon fibre (b) Fiberglass (c) Aramid.

Stresses acting on an example point O on the braid along the principal directions 1 and 2 are shown in Figure 4-9 when the braid is experiencing its maximum shear stress at $\theta_{P_1} = \theta_{P_{max}} = \theta_b$. As shown in this figure, the principal planes are at angles of $\theta_{P_{max}}$ and $\theta_{P_{max}} + 90°$. Figure 4-9 demonstrates the equivalence of the maximum principal plane angle and braid angle. This figure shows that principal planes at $\theta_{P_{max}}$ and $\theta_{P_{max}} + 90°$ are along and perpendicular to yarn direction, respectively. Therefore, the principal stresses are acting perpendicular to the yarns in direction 1 and along the yarns in direction 2 at $\theta_{P_{max}}$ and $\theta_{P_{max}} + 90°$, respectively. Plugging in the $\theta_{P_1} = \theta_{P_{max}}$ in Equations 4-2 and 4-3, the magnitude and direction of principal stresses at $\theta_{P_{max}} = \theta_b$ are determined. Equation 4-2 gives the principal stress in direction 1, σ_1, at principal plane of $\theta_{P_{max}}$ as a compression stress and perpendicular to the braid yarns. Equation 4-3 gives the principal stress in direction 2, σ_2, at principal plane of $\theta_{P_{max}} + 90°$ as a tension stress along the yarn path. The direction of σ_1 and σ_2 on the braid yarns are shown in Figure 4-9. The averaged values of σ_1 and σ_2 for three groups of braids are illustrated with bar plots in Figure 4-10. Compressive principal stresses are -32.86MPa ± 10.05MPa, -23.75MPa ± 5.12MPa and -34.93MPa ± 2.87MPa for carbon fibre, fibreglass and Aramid TBCs, respectively. Tensile principal stresses are 72.84 MPa ± 10.10 MPa, 63.73 MPa ± 5.08 MPa and 74.96 MPa ± 2.82 MPa for carbon fibre, fibreglass and Aramid TBCs, respectively.

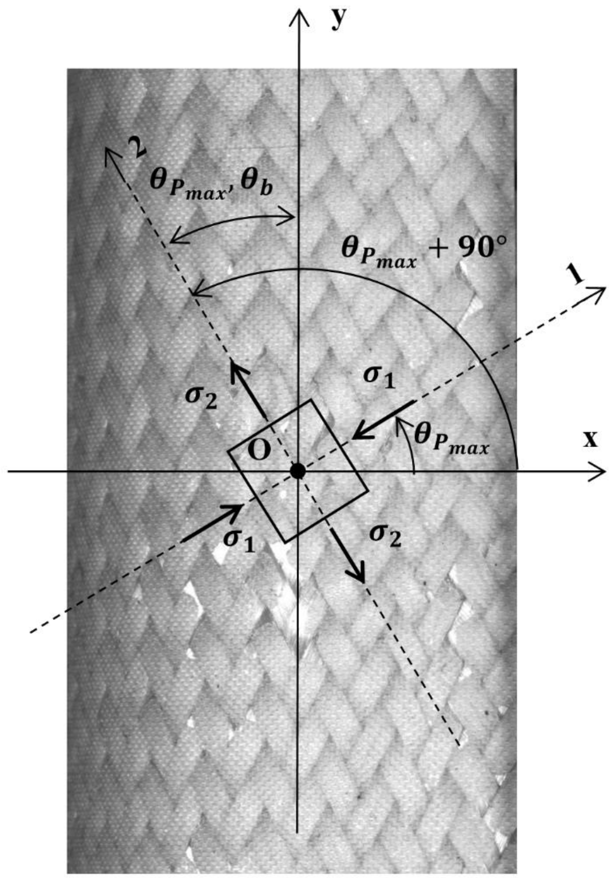

Figure 4-9: Illustration of principal planes and stresses on an example element of the braid at point O while the braid is at its maximum shear stress at $\theta_{P1} = \theta_{Pmax} = \theta_b$.

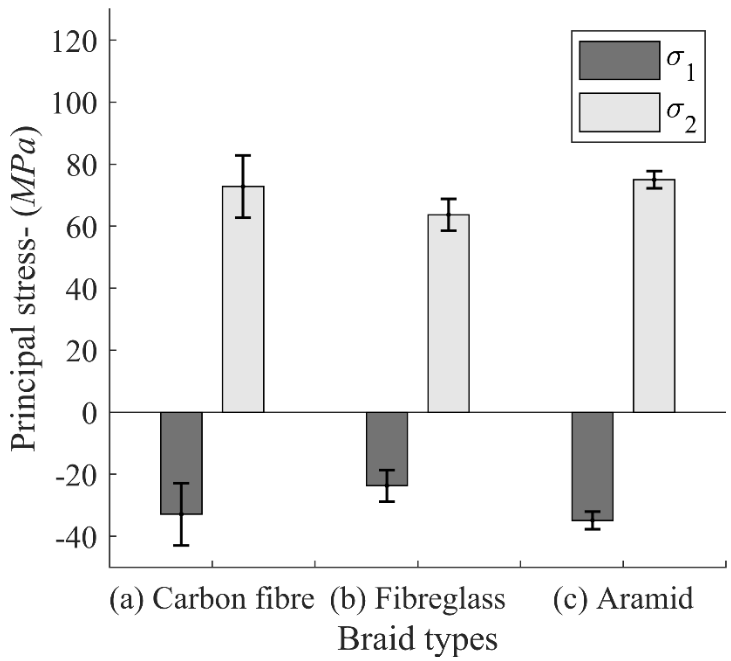

Figure 4-10: Demonstration of principal stresses on braids for the tubular braids (a) Carbon fibre (b) Fiberglass (c) Aramid. Principal stresses in direction 1 are in compression, and in direction 2 are in tension.

Considering the orientation of principal stresses on braid at its maximum principal plane angle and knowing that braid is showing failure behaviour at the same torsional angle corresponding to its maximum principal plane angle (Figure 4-4 and Figure 4-7), it can be argued that braid under combined loading fails when the principal stresses are acting perpendicular and along the braid yarns. This means that when the braid is under combined loading, and plane stress condition exists, braid failure occurs once the principal stresses on braid elements are introducing in planes that are along and perpendicular to braid yarns. In this case, significant matrix failure occurs, and the yarns are compressed and pulled by σ_1 and σ_2, respectively, without any induced shear stress from the matrix on yarns as there is zero shear stress in principal directions. The signs of matrix failure are visible in Figure 4-4 when the linear increase of shear stress on braids stops and drops significantly at the torsional angle where $\theta_{P_{max}} = \theta_b$.

The only similar study who have studied TBCs under combined loading is the paper by Harte and Fleck. However, they had a different analysis focus and used conventional strain gauges for strain measurement purposes. Harte and Fleck analyzed fibreglass TBCs under combined tension-torsion loading to explore their failure on the stress path. Specimens had braid angles of 23°, 40°

and 55°. They applied combined loading by holding a predetermined tensile force on specimen within its uniaxial elastic limit, and then, using the rotation control mode twisted the sample to failure. They found that strain response was almost linear elastic to failure. Furthermore, they realized that the failure mode of braids is highly dependent on the braid angle. For $\theta_b = 55°$, braid failed due to micro buckling; however, for the braid of $\theta_b = 23°$, failure occurred because of fibre fractures. Failure of the braid with $\theta_b = 40°$ was a combination of two previous cases. One set of fibre tows failed in micro buckling, and the tows in bias direction failed due to fibre fracture. Harte and Fleck did not study the principal stresses for braids under combined loading. They were only focused on fibreglass braids and did not use any contact-free measurement technique.

4.3.4 Buckling behaviour of braids

Braids under combined axial/torsional loading showed surface deformation and demonstrated buckling as the torsional angle increased. Figure 4-11 shows example surface height profiles of braids generated using DIC deformation vector fields at three different stages of combined loading. These profiles are plotted along the dark horizontal line in the middle of the braids shown in Figure 4-6. Figure 4-11 shows the braid surface at three stages of the experiment using three types of lines. Line (i) shows the braid while no load is exerted on it. Line (ii) shows the surface of braid when it has reached its maximum shear stress (τ_{max}). Crosshead torsional angle (θ_T) is mentioned at this stage for each braid type. As line (ii) illustrates, at this stage, buckling has slightly begun to propagate in the braid as the surface has deformed a little from its unloaded state. As the torsional angle increases, the buckled surface becomes more evident. To show the progressed buckled profile of braid, line (iii) is plotted. Line (iii) shows the surface profile at a torsional angle of two degrees higher than the state of braid surface showed by line (ii). Two degrees difference was sufficient to show a well-developed buckled surface while still having the braid in the complete focus of cameras without losing correlation.

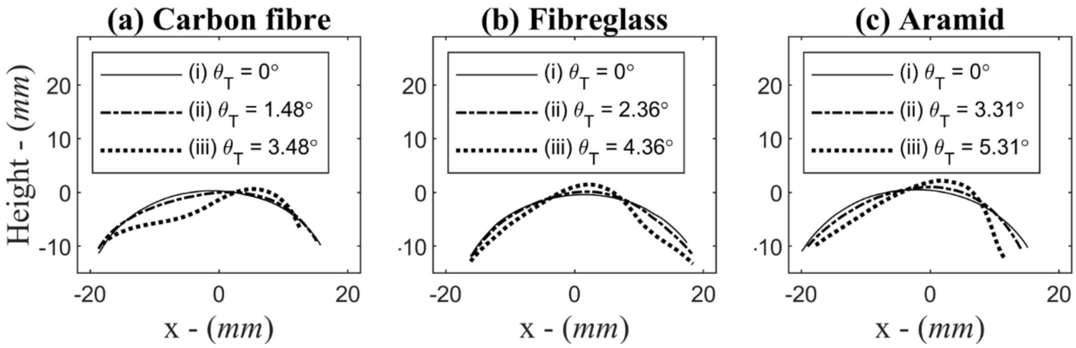

Figure 4-11: Surface height profiles at three loading stages for example tubular braids (a) Carbon fibre (b) Fiberglass (c) Aramid as a demonstration of the buckling process. Line (i) shows the unloaded braid. Line (ii) shows the braids at maximum shear stress (τ_{max}). Line (iii) shows the braid when the torsional angle (θ_T) has increased for two more degrees from the maximum shear stress loading stage so that a progressed buckled surface can be visible.

Example surface of deformed braids in z-direction generated using the DIC technique at maximum shear stress is displayed in Figure 4-12. The richer shades of blue and reds show the braid has displaced negatively and positively in the z-direction, respectively. The displayed surfaces in Figure 4-12 clearly shows that braids have started their buckling process at this stage of loading. Braid surface profiles shown with line (ii) in Figure 4-11 is corresponding to braids shown in Figure 4-12, that the braid is at its maximum shear stress.

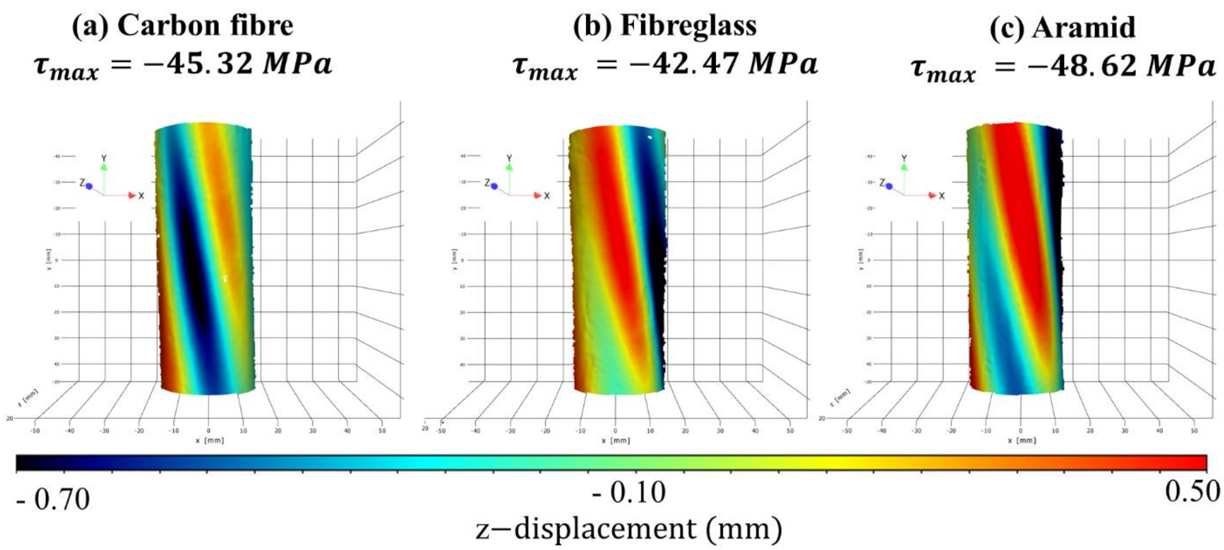

Figure 4-12: Example illustration of deformed braid surface in the z-direction at maximum shear stress (τ_{max}) for the tubular braids (a) Carbon fibre (b) Fiberglass (c) Aramid. According to this figure, the initial buckling of braids at this stage of loading is evident.

Example deformed braids at the end of combined loading experiments at eighteen degrees of crosshead rotation are demonstrated in Figure 4-13. Figure 4-13- (i) evidently shows the braids have buckled significantly at the end of combined loading test stroke. The DIC image of the portion of braid in the FOV of cameras in Figure 4-13- (i) is shown in Figure 4-13- (ii) for different groups of braids. According to this figure, carbon fibre, fibreglass and Aramid braids have shown similar bucking shapes under combined loading. This figure shows the front side of the braids. If we consider buckled shape for the right, left and behind views of the braids identical to their front view, a bucking mode drawn in Figure 4-14 can be generated for all braids. Based on a study on bucking behaviour on thin-walled tubes [123], this is called mode 4 of buckling.

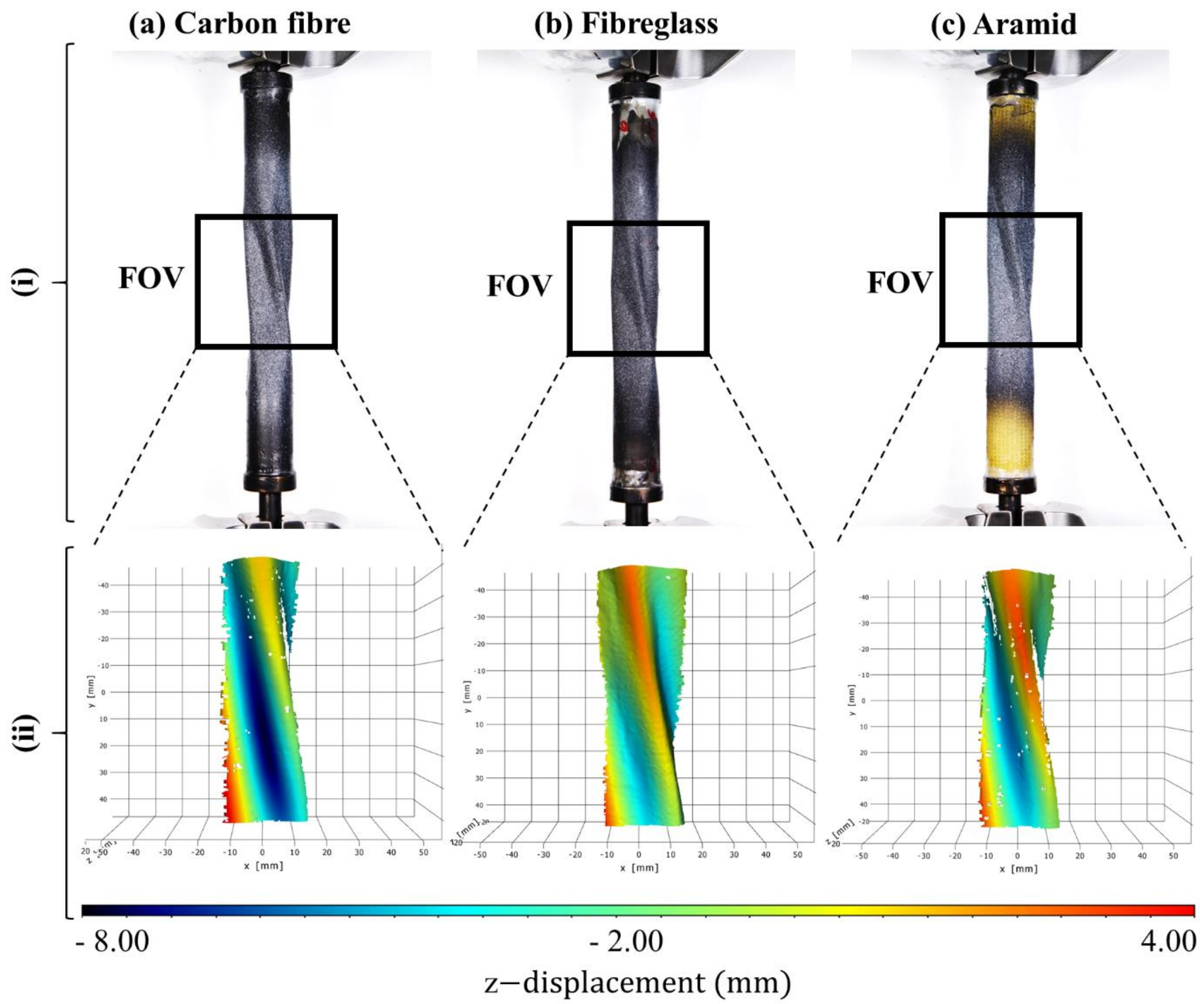

Figure 4-13: Illustration of buckled braids at the end of torsion stroke ($\theta_T = 18°$) for example tubular braids (a) Carbon fibre (b) Fiberglass (c) Aramid. (i) shows the raw images of buckled braids and (ii) shows the DIC generated z-displacement colour maps of the braids in the FOV of cameras.

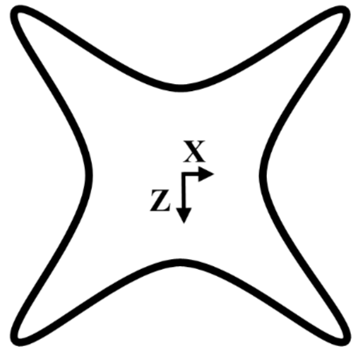

Figure 4-14: Proposed buckled shape for the carbon fibre, fibreglass and Aramid TBCs under combined tension/torsion loading.

4.3.5 Stiffness of braids in combined loading

Torque magnitude versus torsional angle for braids under combined loading is shown in Figure 4-15. As the crosshead rotates at a constant rate, initially torque increases on braids until a point that suddenly drops. This point is called the maximum torque, T_{max}. All the nine samples have shown a pretty linear trend in their torque-torsional angle plot until the maximum torque. The slope of the linear region of Figure 4-15 is defined as the torsional stiffness of braids under combined loading. The torsional stiffness of braids is compared using bar plots shown in Figure 4-16. Carbon fibre braids have the highest torsional stiffness, and the fibreglass braids have the lowest value of stiffness under combined loading.

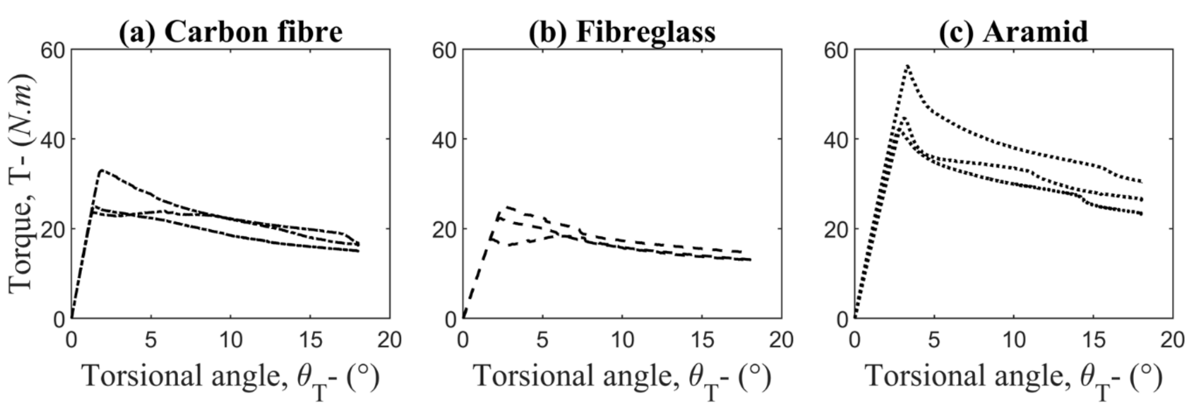

Figure 4-15: Plot of toque versus torsional angle for the tubular braids (a) Carbon fibre (b) Fiberglass (c) Aramid.

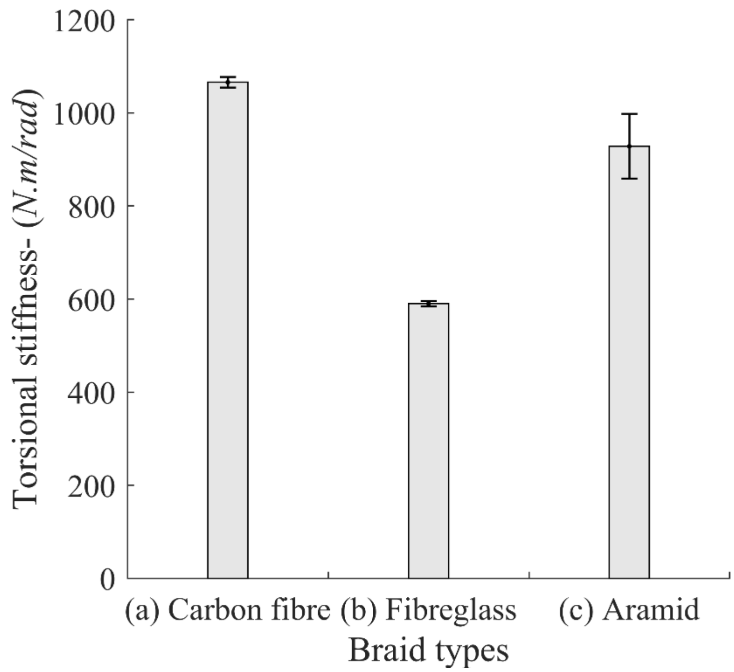

Figure 4-16: Torsional stiffness magnitudes for the tubular braids (a) Carbon fibre (b) Fiberglass (c) Aramid.

4.4 Conclusions

In this chapter, carbon fibre, fibreglass and Aramid TBCs under combined tension/torsion loading were evaluated and compared with each other. For this purpose, braid specimens were preloaded to a specific tensile stress of 40MPa and then torsional load was applied. Contact-free 3D DIC was utilized as the measurement technique.

Primarily, critical geometrical parameters of braids such as braid diameters, braid angle, yarn width, and fibre volume fraction were reported. These parameters were measured using physical and optical techniques. The accuracy of the DIC measurement technique was verified by comparing the diameter of braids that were measured using physical micrometer and DIC technique. The result of the comparison was promising since the maximum difference between diameters measured by two different techniques was 1.60%.

The maximum shear stresses a TBC could endure while experiencing 40MPa tensile stress was determined for different braid fibres. The carbon fibre and Aramid braids showed almost equal maximum shear stress and higher magnitudes than fibreglass braids.

Using the DIC technique, shear strain fields for TBCs were generated in several steps of loading stroke. According to the strain field results, braids have experienced non-uniform shear strain distribution due to the woven structure of braided composites. Furthermore, it was observed that shear strain variations on braids had shown a period that corresponded to the braiding period of TBCs.

The failure behaviours of carbon fibre, fibreglass and Aramid TBCs were investigated and compared with the braid angle of specimens. It was shown that for the TBCs tested in this study when braids are experiencing constant tension stress, and shear stress is increasing on braid, failure occurs at the moment when the principal stresses in braid elements are acting perpendicular and along the braid yarn orientations. At this point, the linear increase of shear stress on braids stopped and dropped sharply, matrix failure occurred, and braid could not endure any more load.

TBCs under combined loading demonstrated buckled surface when the torsional load was increasing on braids. Using the 3D DIC results, the deformed profile of braid was plotted at different loading stages to see how the buckling progresses. According to 3D DIC results, braids initiated their buckling process at the maximum shear stress. Furthermore, based on raw and 3D DIC images of braids at the end of the loading process, a symmetric four corner buckled surface profile for all TBCs was anticipated.

Lastly, by plotting the applied torque versus torsional angle for TBCs under combined tension/torsion, the torsional stiffness of braids was studied and compared. All samples showed a linear trend in their torque-torsional angle plot until the maximum torque where the braids failed. Carbon fibre braids had the highest torsional stiffness, and the fibreglass braids had the lowest value of torsional stiffness under combined loading.

Chapter 5 Conclusions and future work

5.1 Conclusions

This thesis investigated the mechanical properties of the manufactured TBCs under tension and combined tension/torsion loading. Throughout this study, 3D DIC, as a contact-free measurement technique, was utilized to analyze the displacements, strain fields and conduct surface reconstructions of TBCs. Two types of experiments with two different loading types were performed on TBCs: uniaxial tension tests and combined tension/torsion tests

In chapter 3, a comprehensive study was presented to examine and compare TBCs manufactured using a single manufacturing process but using different fibres: carbon fibre, fibreglass and Aramid. In this chapter, elastic and permanent deformation of all three types of braids were studied, and longitudinal elastic moduli were calculated for different braids. According to stress-strain carves generated from 3D DIC outputs and 3D DIC strain distribution maps, a tensile stress magnitude was selected within the elastic limit of three types of braids. The determined stress was used as the preload to run the combined loading experiments shown in Chapter 4. Moreover, in Chapter 3, by studying $\epsilon_{xx} - \epsilon_{\text{yy}}$ plots, the quality of the braid manufacturing technique was assessed. By performing surface reconstruction using 3D DIC results, the necking process of TBCs during tensile test stroke was compared between different braids. Axial stiffness and ultimate tensile strength for all braids were determined by assessing load and displacement outputs of the test frame. The fracture behaviour of TBCs was also investigated, and failure codes were assigned for different braids according to the ASTM D3039, the standard test method for tensile properties of polymer matrix composite materials. By implementing the 3D DIC technique, observation of the failure location on braids was achievable. Results presented in Chapter 3 are unique, and there is no similar study on TBCs to study these mechanical responses between carbon fibre, fibreglass and Aramid braids.

Chapter 4 was focused on examining the mechanical response of carbon fibre, fibreglass and Aramid TBCs under combined tension/torsion loading. For this purpose, braid specimens were preloaded to specific tensile stress within the elastic limit of three types of braids based on tensile experiment results and then the torsional load was applied. Contact-free 3D DIC was utilized as the measurement technique. In this chapter, the shear strain distribution of braids was shown for different braids. The maximum shear stress for all braids was determined and compared for different braids. The failure process on carbon fibre, fibreglass and Aramid TBCs was investigated and compared with the braid angle of specimens. It was shown that for the TBCs tested in this study, when braids are experiencing combined loading, failure occurs when the principal stresses in braid elements are acting perpendicular and along the braid yarn orientations. In Chapter 4, the buckled surface on braids under combined loading was studied using raw images and 3D DIC technique. Moreover, the torsional stiffness of different braids under combined loading was calculated and compared. Combined loading on carbon fibre, fibreglass and Aramid TBCs using 3D DIC technique has never been studied thoroughly like what was presented in Chapter 4. The results and discussion presented in this thesis can be used for evaluating numerical and analytical models for predicting TBCs mechanical behaviour under tensile and combined loading.

5.2 Future Work

This thesis studied the mechanical properties manufactured TBCs under uniaxial and combine tension/torsion loading using the 3D DIC measurement technique was examined. There are still several research gaps in the field of braided composites can be accomplished following this work.

Combined loading is a common loading state that braided structures are subjected to. This thesis was focused on combined tension/torsion loading. Other combination of loadings can be studied such as, combines shear/bending, torsion/bending. Cyclic combined loadings can be another study on TBCs since structural component commonly experience loading/unloading states such as cyclic combined tension/torsion loading.

This thesis considered evaluating combined loading states for braids with a single layer of the preform with a circular cross-section. Structural components that are manufactured using braided composites are not always in a tubular shape. Braided composites with different cross-sections such as square, I beam, and airfoil can be studied under combined loading. Moreover, braided composites with several layers of preforms with different combinations of fibres can be studied under combined loading. The fibre variations can be between each layer of braid or within the layers, for example each layer can be a combination of carbon fibre and Aramid yarns. Hybrid fibres can also be considered to use for braid layers.

This thesis analyzed the failure mechanism under combined loading for TBCs with the same braid angle for different fibre material. Similar failure analysis that was conducted in this thesis can be performed for braids with similar material but varying braid angles. This suggested study can validate the failure analysis presented in this thesis.

Different DIC measurement approaches can be used for studying braided composites under combined loading. For example, the use of macro lenses to examine single unit cells during combined loading can be considered. In this thesis, a 360° view was not captured using DIC cameras. Therefore, the generation of a complete buckled profile of braids was not achievable. Designing a DIC set up to examine the full view of braids under loading can be another way to study braided composites.

In this thesis, TBCs were experimentally investigated under tensile and combined loadings. The analyzed results of these experiments can significantly be used for evaluating the accuracy and reliability of current and future analytical and numerical models studying TBCs with similar structure studied here.

References

[1] "Composites and Plastics Archives - Aerospace Industries Association of Canada : Aerospace Industries Association of Canada." [Online]. Available: https://aiac.ca/product-categories/composites-and-plastics/. [Accessed: 04-Aug-2020].

[2] J. P. Carey, "1 - Introduction to braided composites," in *Handbook of Advances in Braided Composite Materials*, J. P. Carey, Ed. Woodhead Publishing, 2017, pp. 1–21.

[3] J. Carey, A. Fahim, and M. Munro, "Design of braided composite cardiovascular catheters based on required axial, flexural, and torsional rigidities," *J. Biomed. Mater. Res. Part B Appl. Biomater.*, vol. 70B, no. 1, pp. 73–81, 2004.

[4] J. A. [de O. Simões] and A. T. Marques, "Determination of stiffness properties of braided composites for the design of a hip prosthesis," *Compos. Part A Appl. Sci. Manuf.*, vol. 32, no. 5, pp. 655–662, 2001.

[5] "AERO - Boeing 787 from the Ground Up." [Online]. Available: https://www.boeing.com/commercial/aeromagazine/articles/qtr_4_06/article_04_2.html. [Accessed: 04-Aug-2020].

[6] B. Dauda, S. O. Oyadiji, and P. Potluri, "Characterising mechanical properties of braided and woven textile composite beams," *Appl. Compos. Mater.*, vol. 16, no. 1, pp. 15–31, 2009.

[7] A.-M. Harte and N. A. Fleck, "On the mechanics of braided composites in tension," *Eur. J. Mech. - A/Solids*, vol. 19, no. 2, pp. 259–275, 2000.

[8] G. W. Melenka and J. P. Carey, "Experimental analysis of diamond and regular tubular braided composites using three-dimensional digital image correlation," *J. Compos. Mater.*, vol. 51, no. 28, pp. 3887–3907, 2017.

[9] C. Ayranci and J. Carey, "2D braided composites: A review for stiffness critical applications," *Compos. Struct.*, vol. 85, no. 1, pp. 43–58, 2008.

[10] T. Wehrkamp-Richter, R. Hinterhölzl, and S. T. Pinho, "Damage and failure of triaxial braided composites under multi-axial stress states," *Compos. Sci. Technol.*, vol. 150, pp.

32–44, 2017.

[11] L. Gong, X. Gao, H. Yang, Y. Liu, and X. Yao, “Design on the driveshaft of 3D 4-Directional carbon fiber braided composites,” *Compos. Struct.*, vol. 203, pp. 466–473, Nov. 2018.

[12] W. Hao, Z. Huang, L. Zhang, G. Zhao, and Y. Luo, “Study on the torsion behavior of 3-D braided composite shafts,” *Compos. Struct.*, vol. 229, p. 111384, 2019.

[13] G. Zhao, L. Zhang, C. Tang, Y. Zhou, W. Hao, and Y. Luo, “Experimental study on the torsion behavior of a 3D 4-directionally braided composite shaft using DIC and AE,” *Polym. Test.*, vol. 72, pp. 122–131, 2018.

[14] C. Unlusoy and G. W. Melenka, “Flexural testing of cellulose fiber braided composites using three dimensional digital image correlation,” *Compos. Struct.*, vol. 230, no. August, p. 111538, 2019.

[15] G. Yu, X. Gao, and Y. Song, “Experimental investigation of the tension-torsion coupling behavior on needled unidirectional C/SiC composites,” *Mater. Sci. Eng. A*, 2017.

[16] G. W. Melenka *et al.*, “3 - Manufacturing processes for braided composite materials,” in *Handbook of Advances in Braided Composite Materials*, J. P. Carey, Ed. Woodhead Publishing, 2017, pp. 47–153.

[17] T. Alpyildiz, “3D geometrical modelling of tubular braids,” *Text. Res. J.*, vol. 82, no. 5, pp. 443–453, 2012.

[18] S. Nawaz, P. Potluri, M. Gautam, and S. S. Roy, “Study of braid tolpogy and effect of braid pattern on composite properties,” in *ICCM International Conferences on Composite Materials*, 2013, vol. 2013-July, pp. 689–695.

[19] C. Ayranci, D. Romanyk, and J. P. Carey, “Elastic properties of large-open-mesh 2D braided composites: Model predictions and initial experimental findings,” *Polym. Compos.*, vol. 31, no. 12, pp. 2017–2024, Dec. 2010.

[20] C. K. Leung, G. W. Melenka, D. S. Nobes, and J. P. Carey, “The effect on elastic modulus of rigid-matrix tubular composite braid radius and braid angle change under tensile

loading," *Compos. Struct.*, vol. 100, pp. 135–143, 2013.

[21] A.-M. Harte and N. A. Fleck, "Deformation and failure mechanisms of braided composite tubes in compression and torsion," *Acta Mater.*, vol. 48, no. 6, pp. 1259–1271, 2000.

[22] G. W. Melenka and J. P. Carey, "Experimental analysis of diamond and regular tubular braided composites using three-dimensional digital image correlation," *J. Compos. Mater.*, vol. 51, no. 28, pp. 3887–3907, 2017.

[23] Y. Chai *et al.*, "Damage evolution in braided composite tubes under torsion studied by in-situ X-ray computed tomography," *Compos. Sci. Technol.*, vol. 188, p. 107976, 2020.

[24] B. Bruni-Bossio, C. Ayranci, J. P. Carey, T. Omonov, and J. Curtis, "Experimental testing of the tensile elastic properties of cellulose braided composites," *Compos. Part B Eng.*, vol. 166, no. October 2018, pp. 542–548, 2019.

[25] A. K. Kaw, *Mechanics of composite materials*. CRC press, 2005.

[26] A. K. Kaw, *Mechanics of Composite Materials*. CRC Press, 2005.

[27] I. M. Daniel and O. Ishai, *Engineering Mechanics of Composite Materials*. Oxford University Press, 2007.

[28] R. M. Jones, *Mechanics of composite materials [by] Robert M. Jones*. Washington: Scripta Book Co, 1975.

[29] T. J. C. Liu and H. C. Wu, "Fiber direction and stacking sequence design for bicycle frame made of carbon/epoxy composite laminate," *Mater. Des.*, vol. 31, no. 4, pp. 1971–1980, 2010.

[30] J.-H. Byun, "The analytical characterization of 2-D braided textile composites," *Compos. Sci. Technol.*, vol. 60, no. 5, pp. 705–716, 2000.

[31] P. Potluri and A. Manan, "Mechanics of non-orthogonally interlaced textile composites," *Compos. Part A Appl. Sci. Manuf.*, vol. 38, no. 4, pp. 1216–1226, 2007.

[32] P. Tan, L. Tong, and G. P. Steven, "A three-dimensional modelling technique for predicting the linear elastic property of opened-packing woven fabric unit cells," *Compos. Struct.*, vol. 38, no. 1, pp. 261–271, 1997.

[33] X. Ji *et al.*, “Multi-scale simulation and finite-element-assisted computation of elastic properties of braided textile reinforced composites.”

[34] P. Qu, X. Guan, Y. Jia, S. Lou, and J. Nie, “Effective elastic properties and stress distribution of 2D biaxial nonorthogonally braided composites.”

[35] G. Fang and J. Liang, “A review of numerical modeling of three-dimensional braided textile composites,” *J. Compos. Mater.*, vol. 45, no. 23, pp. 2415–2436, 2011.

[36] F. K. Ko, “Braiding,” in *Engineered Materials Handbook*, Metals Park, OH: ASM International, 1987, pp. 519–528.

[37] F. K. Ko, *Handbook of Industrial Braiding*. Atkins and Pearce, 1989.

[38] J. H. van Ravenhorst and R. Akkerman, “Circular braiding take-up speed generation using inverse kinematics,” *Compos. Part A Appl. Sci. Manuf.*, vol. 64, pp. 147–158, 2014.

[39] G. w. Du and P. Popper, “Analysis of a Circular Braiding Process for Complex Shapes,” *J. Text. Inst.*, vol. 85, no. 3, pp. 316–337, 1994.

[40] A. Yokoyama, Z. Maekawa, H. Hamada, S. Ueda, Y. Iwasaki, and H. Kobayashi, “Mechanical properties of FRP (fibre-reinforced plastic) with braided structure. II. Tensile behaviours of tubes,” 1988.

[41] A. Yokoyama, Z. Maekawa, H. Hamada, T. Horino, and S. Ueda, “Mechancal properties of FRP (fibre-reinforced plastic) with braided structure. III. Bending behaviours of tubes,” 1988.

[42] Z. Maekawa, H. Hamada, T. Horino, A. Yokoyama, and Y. Iwasaki, “Mechanical properties of FRP (fabric-reinforced plastics) with braided structure. I. Lateral compressional behaviours of tubes,” 1988.

[43] Z. Maekawa, H. Hamada, A. Yokoyama, H. Kobayashi, A. Fujita, and T. Uozumi, “Flat and Cord Braiding Construction of Reinforcement in Three-Dimensional Composites (4th Report, I-Shape Integrated Beam),” *Nihon Kikai Gakkai Ronbunshu, A Hen/Transactions Japan Soc. Mech. Eng. Part A*, vol. 57, no. 535, pp. 563–568, 1991.

[44] A. Fujita, Z. Maekawa, H. Hamada, M. Matsuda, and T. Matsuo, “Mechanical behavior

and fracture mechanism of thermoplastic composites with commingled yarn," *J. Reinf. Plast. Compos.*, vol. 12, no. 2, pp. 156–172, 1993.

[45] H. Hamada, T. Nakatani, A. Nakai, and K. Kameo, "The crushing performance of a braided I-beam," *Compos. Sci. Technol.*, vol. 59, no. 12, pp. 1881–1890, 1999.

[46] M. Sakaguchi, A. Nakai, H. Hamada, and N. Takeda, "The mechanical properties of unidirectional thermoplastic composites manufactured by a micro-braiding technique," *Compos. Sci. Technol.*, vol. 60, no. 5, pp. 717–722, 2000.

[47] A. Nakai, T. Ohki, N. Takeda, and H. Hamada, "Mechanical properties and micro-fracture behaviors of flat braided composites with a circular hole," *Compos. Struct.*, vol. 52, no. 3–4, pp. 315–322, 2001.

[48] K. Fujihara, Z.-M. Huang, S. Ramakrishna, K. Satknanantham, and H. Hamada, "Performance study of braided carbon/PEEK composite compression bone plates," *Biomaterials*, vol. 24, no. 15, pp. 2661–2667, 2003.

[49] O. A. Khondker, T. Fukui, X. Yang, A. Nakai, and H. Hamada, "Fabrication, processing and tensile properties of weft-knitted hybrid composites combining microbraiding and compression molding techniques," in *Annual Technical Conference - ANTEC, Conference Proceedings*, 2004, vol. 2, pp. 2683–2686.

[50] K. Fujihara, E. Yoshida, A. Nakai, S. Ramakrishna, and H. Hamada, "Influence of micro-structures on bending properties of braided laminated composites," *Compos. Sci. Technol.*, vol. 67, no. 10, pp. 2191–2198, 2007.

[51] Y. Shimizu, K. Hashimoto, T. Uozumi, A. Ohtani, and A. Nakai, "Mechanical properties of thick composite pipes reinforced with multilayer braid," in *ICCM International Conferences on Composite Materials*, 2013, vol. 2013-July.

[52] H. Hamada, K. Kameo, M. Sakaguchi, H. Saito, and M. Iwamoto, "Energy-absorption properties of braided composite rods," *Compos. Sci. Technol.*, vol. 60, no. 5, pp. 723–729, 2000.

[53] P. Potluri, A. Manan, M. Francke, and R. J. Day, "Flexural and torsional behaviour of biaxial and triaxial braided composite structures," *Compos. Struct.*, vol. 75, no. 1–4, pp.

377–386, Sep. 2006.

[54] S. Nawaz, P. Potluri, M. Gautam, and S. S. Roy, “Study of braid tolpogy and effect of braid pattern on composite properties,” in *ICCM International Conferences on Composite Materials*, 2013, vol. 2013-July, pp. 689–695.

[55] B. Dauda, S. O. Oyadiji, and P. Potluri, “Characterising mechanical properties of braided and woven textile composite beams,” *Appl. Compos. Mater.*, vol. 16, no. 1, pp. 15–31, 2009.

[56] M. Gautam, K. B. Katnam, P. Potluri, V. Jha, J. Latto, and N. Dodds, “Hybrid composite tensile armour wires in flexible risers: A multi-scale model,” *Compos. Struct.*, vol. 162, pp. 13–27, 2017.

[57] S. S. Roy, P. Potluri, and C. Soutis, “Tensile Response of Hoop Reinforced Multiaxially Braided Thin Wall Composite Tubes,” *Appl. Compos. Mater.*, vol. 24, no. 2, pp. 397–416, Apr. 2017.

[58] J. Carey, M. Munro, and A. Fahim, “Longitudinal elastic modulus prediction of a 2-D braided fiber composite,” *J. Reinf. Plast. Compos.*, vol. 22, no. 9, pp. 813–831, 2003.

[59] K. Hillermeier, “Textile structural composites. Edited by T- W. Chou and F. KO. Elsevier Science Publishers, Amsterdam 1988. xiii, 480 pp., bound, US $155.25. -ISBN 0-444-42992-1,” *Adv. Mater.*, vol. 1, no. 10, p. 356, 1989.

[60] T. Ishikawa and T.-W. Chou, “Stiffness and strength behaviour of woven fabric composites,” *J. Mater. Sci.*, vol. 17, no. 11, pp. 3211–3220, 1982.

[61] T. Ishikawa and T.-W. Chout, “One-dimensional micromechanical analysis of woven fabric composites,” *AIAA J.*, vol. 21, no. 12, pp. 1714–1721, 1983.

[62] S. V Lomov *et al.*, “Full-field strain measurements for validation of meso-FE analysis of textile composites,” *Compos. Part A Appl. Sci. Manuf.*, vol. 39, no. 8, pp. 1218–1231, 2008.

[63] S. V Lomov *et al.*, “Meso-FE modelling of textile composites: Road map, data flow and algorithms,” *Compos. Sci. Technol.*, vol. 67, no. 9, pp. 1870–1891, 2007.

[64] J.-H. Byun, “The analytical characterization of 2-D braided textile composites,” 2000.

[65] J. W. Deaton, H. B. Dexter, A. Markus, and K. R. Mcdonnell, “EVALUATION OF BRAIDED STIFFENER CONCEPTS FOR TRANSPORT AIRCRAFT WING STRUCTURE APPLICATIONS.”

[66] K. R. Evans and J. P. Carey, “Feasibility of a braided composite for orthopedic bone cast.,” *Open Biomed. Eng. J.*, vol. 7, no. July, pp. 9–17, 2013.

[67] J. D. Hudgins, R.G. ; Muzzy, “Assessment of compressive strength of flexible composite materials for spinal implantation,” *J. Compos. Mater.*, vol. 34, no. 17, pp. 1472–93, 2000.

[68] R. Garryl Hudgins and J. D. Muzzy, “Analytical Stress Model for a Composite Prosthetic Intervertebral Disc.”

[69] D. Branscomb, D. Beale, and R. Broughton, “New Directions in Braiding,” *J. Eng. Fiber. Fabr.*, vol. 8, pp. 11–24, 2013.

[70] P. Potluri, A. Manan, M. Francke, and R. J. Day, “Flexural and torsional behaviour of biaxial and triaxial braided composite structures,” 2006.

[71] S. Rana and R. Fangueiro, *Braided structures and composites: production, properties, mechanics, and technical applications*. 2015.

[72] F. K. Ko, C. M. Pastore, and A. A. Head, *Atkins & Pearce handbook of industrial braiding*. [Covington, Ky.]: [Atkins & Pearce], 1990.

[73] J. P. Carey, G. W. Melenka, A. J. Hunt, and C. Ayranci, “5 - Introduction to braided composite material behavior,” in *Handbook of Advances in Braided Composite Materials*, J. P. Carey, Ed. Woodhead Publishing, 2017, pp. 207–237.

[74] T.-W. Chou, *Microstructural Design of Fiber Composites*. Cambridge University Press, 1992.

[75] R. Kamiya, B. A. Cheeseman, P. Popper, and T.-W. Chou, “Some recent advances in the fabrication and design of three-dimensional textile preforms: a review,” *Compos. Sci. Technol.*, vol. 60, no. 1, pp. 33–47, 2000.

[76] G. W. Melenka, C. M. Pastore, F. K. Ko, and J. P. Carey, “9 - Advances in 2-D and 3-D

braided composite material modeling," in *Handbook of Advances in Braided Composite Materials*, J. P. Carey, Ed. Woodhead Publishing, 2017, pp. 321–363.

[77] W. S. Johnson, J. E. Masters, D. W. Wilson, J. Chen, T. M. McBride, and S. B. Sanchez, "Sensitivity of Mechanical Properties to Braid Misalignment in Triaxial Braid Composite Panels," *J. Compos. Technol. Res. - J Compos TECH RES*, vol. 20, 1998.

[78] G. W. Melenka, M. Ivey, and J. P. Carey, "2 - Working with the braided composite app," in *Handbook of Advances in Braided Composite Materials*, J. P. Carey, Ed. Woodhead Publishing, 2017, pp. 23–43.

[79] G. W. Melenka, E. Lepp, B. K. O. Cheung, and J. P. Carey, "Micro-computed tomography analysis of tubular braided composites," *Compos. Struct.*, vol. 131, pp. 384–396, 2015.

[80] G. W. Melenka and J. P. Carey, "Development of a generalized analytical model for tubular braided-architecture composites," *J. Compos. Mater.*, vol. 51, no. 28, pp. 3861–3875, 2017.

[81] M. Minus and S. Kumar, "The Processing, Properties, and Structure of Carbon Fibers:"

[82] E. Fitzer *et al.*, "Fibers, 5. Synthetic Inorganic," in *Ullmann's Encyclopedia of Industrial Chemistry*, American Cancer Society, 2000.

[83] K. Hillermeier, "Prospects of Aramid as a Substitute for Asbestos," *Text. Res. J.*, vol. 54, no. 9, pp. 575–580, 1984.

[84] Richard A. Armellino, "Lightweight Armor and Method of Fabrication," no. 19, 1976.

[85] M. Ehsani, "Concrete bridges: Repair of concrete bridges with FRP," vol. 10, pp. 14–15, 2006.

[86] M. A. Ivey, J. P. R. Carey, and C. Ayranci, "Braid reinforced polymeric rebar production and characterization," *Int. SAMPE Tech. Conf.*, 2014.

[87] K. R. Evans and J. P. Carey, "Feasibility of a Braided Composite for Orthopedic Bone Cast," *Open Biomed. Eng. J.*, vol. 7, no. 1, pp. 9–17, 2013.

[88] "Braided Carbon Biaxial Sleeve." [Online]. Available: https://s3.amazonaws.com/cdn.fibreglast.com/downloads/00357.pdf. [Accessed: 15-Nov-

2018].

[89] D. Brookstein, “Processing advanced braided composites,” *Adv. Compos. Process. Technol.*, pp. 33–36, 1988.

[90] D. Brookstein, “Structural applications of advanced braided composites,” *Proc. SPE/APC*, vol. 88, pp. 415–424, 1988.

[91] B. S. Kim and T. F. Lehnhoff, “Polymeric Composite Tube Fabrication,” *J. Eng. Mater. Technol.*, vol. 117, no. 2, pp. 235–237, 1995.

[92] G. Li, S. Hedlund, S.-S. Pang, W. Alaywan, J. Eggers, and C. Abadie, “Repair of damaged RC columns using fast curing FRP composites,” *Compos. Part B Eng.*, vol. 34, no. 3, pp. 261–271, 2003.

[93] C. M. Newsom, “Tubular autoclave for curing composite parts,” 1991.

[94] T. Murphey and S. Pellegrino, “A Novel Actuated Composite Tape-Spring for Deployable Structures,” in *45th AIAA/ASME/ASCE/AHS/ASC Structures, Structural Dynamics & Materials Conference*, .

[95] M. Okano, K. Sugimoto, H. Saito, A. Nakai, and H. Hamada, “Effect of the braiding angle on the energy absorption properties of a hybrid braided FRP tube,” *Proc. Inst. Mech. Eng. Part L J. Mater. Des. Appl.*, vol. 219, no. 1, pp. 59–66, 2005.

[96] J. B. Hinves and C. D. Douglas, “The development of a hybrid advanced composite-syntactic foam structural component for use in undersea vehicles,” in *Proceedings of OCEANS ’93*, 1993, pp. III468-III472 vol.3.

[97] T. Uozumi, A. Kito, and T. Yamamoto, “CFRP using braided preforms/RTM process for aircraft applications,” *Adv. Compos. Mater.*, vol. 14, no. 4, pp. 365–383, 2005.

[98] T. Wehrkamp-Richter, R. Hinterhölzl, and S. T. Pinho, “Damage and failure of triaxial braided composites under multi-axial stress states,” *Compos. Sci. Technol.*, vol. 150, pp. 32–44, 2017.

[99] A. Kelkar, J. Tate, J. Whitcomb, and X. Tang, “Performance Evaluation and Modeling of Braided Composites,” in *44th AIAA/ASME/ASCE/AHS/ASC Structures, Structural*

Dynamics, and Materials Conference, .

[100] G. Yu, X. Gao, and Y. Song, “Experimental investigation of the tension-torsion coupling behavior on needled unidirectional C/SiC composites,” *Mater. Sci. Eng. A*, vol. 696, pp. 190–197, 2017.

[101] S. Amijima, T. Fujii, and M. Hamaguchi, “Static and fatigue tests of a woven glass fabric composite under biaxial tension-torsion loading,” *Composites*, vol. 22, no. 4, pp. 281–289, 1991.

[102] B. Pan, L. Yu, Y. Yang, W. Song, and L. Guo, “Full-field transient 3D deformation measurement of 3D braided composite panels during ballistic impact using single-camera high-speed stereo-digital image correlation,” *Compos. Struct.*, vol. 157, pp. 25–32, 2016.

[103] Y. Zheng *et al.*, “Tensile response of carbon-aramid hybrid 3D braided composites,” *Mater. Des.*, vol. 116, pp. 246–252, 2017.

[104] D. Zhang, S. Yu, G. Feng, X. Xiao, Q. Ma, and K. Qian, “Numerical Identification of Meso Length-Effect and Full-Field Edge-Effect of 3D Braided Composites,” *Appl. Compos. Mater.*, vol. 25, pp. 1–22, 2017.

[105] J. Cichosz, T. Wehrkamp-Richter, H. Koerber, R. Hinterhölzl, and P. P. Camanho, “Failure and damage characterization of (±30°) biaxial braided composites under multiaxial stress states,” *Compos. Part A Appl. Sci. Manuf.*, vol. 90, pp. 748–759, 2016.

[106] B. Practices and U. Quanti, *A Good Practices Guide for Digital Image Correlation*, no. January. International Digital Image Correlation Society, 2018.

[107] R. Elhajjar, S. Shams, and D. Kehrl, “Closed form solutions for predicting the elastic behavior of quasi-isotropic triaxially braided composites,” *Compos. Struct.*, vol. 101, pp. 1–8, 2013.

[108] Z. T. Kier, A. Salvi, G. Theis, A. M. Waas, and K. Shahwan, “Estimating mechanical properties of 2D triaxially braided textile composites based on microstructure properties,” *Compos. Part B Eng.*, vol. 68, pp. 288–299, 2015.

[109] T. C. Chu, W. F. Ranson, M. A. Sutton, and W. H. Peters, “Applications of Digital-Image-

Correlation Techniques to Experimental Mechanics," no. September, pp. 232–244, 1985.

[110] M. A. Sutton, J.-J. Orteu, Image, and H. W. Schreier, "Image Correlation for Shape, Motion and Deformation Measurements."

[111] J. Carey, M. Munro, and A. Fahim, "Longitudinal elastic modulus prediction of a 2-D braided fiber composite," *J. Reinf. Plast. Compos.*, vol. 22, no. 9, pp. 813–831, 2003.

[112] C. Ayranci and J. P. Carey, "Experimental validation of a regression-based predictive model for elastic constants of open mesh tubular diamond-braid composites," *Polym. Compos.*, vol. 32, no. 2, pp. 243–251, 2011.

[113] G. W. Melenka, A. J. Hunt, C. M. Pastore, F. K. Ko, and J. P. Carey, "4 - Advanced testing of braided composite materials," in *Handbook of Advances in Braided Composite Materials*, J. P. Carey, Ed. Woodhead Publishing, 2017, pp. 155–204.

[114] "ASTM E111 - 17 Standard Test Method for Young's Modulus, Tangent Modulus, and Chord Modulus." [Online]. Available: https://www.astm.org/Standards/E111.htm. [Accessed: 26-Feb-2020].

[115] D 3039/D3039M ASTM, "Standard Test Method for Tensile Properties of Polymer Matrix Composite Materials," *Annu. B. ASTM Stand.*, vol. 15.03, pp. 105–116, 2000.

[116] LaVision GmbH, "Product-Manual DaVis StrainMaster 10.0 Item-Number(s): 1003017," 2018.

[117] R. A. Naik, P. G. Ifju, and J. E. Masters, "Effect of Fiber Architecture Parameters on Deformation Fields and Elastic Moduli of 2-D Braided Composites," *J. Compos. Mater.*, vol. 28, no. 7, pp. 656–681, 1994.

[118] C. K. Leung, G. W. Melenka, D. S. Nobes, and J. P. Carey, "The effect on elastic modulus of rigid-matrix tubular composite braid radius and braid angle change under tensile loading," *Compos. Struct.*, vol. 100, pp. 135–143, Jun. 2013.

[119] N. Chernov, "Circle Fit (Pratt method)," *MATLAB Central File Exchange. Retrieved April 28, 2020.*, 2020. .

[120] L. Xu, S. J. Kim, C.-H. Ong, and S. K. Ha, "Prediction of material properties of biaxial

and triaxial braided textile composites," *J. Compos. Mater.*, vol. 46, no. 18, pp. 2255–2270, 2012.

[121] G. W. Melenka and J. P. Carey, "Development of a generalized analytical model for tubular braided-architecture composites," *J. Compos. Mater.*, vol. 51, no. 28, pp. 3861–3875, 2017.

[122] F. Beer, E. R. Jr. Johnston, J. DeWolf, and D. Mazurek, *Mechanics of Materials*. McGraw-Hill Education, 2011.

[123] R. Gonçalves and D. Camotim, "Buckling behaviour of thin-walled regular polygonal tubes subjected to bending or torsion," *Thin-Walled Struct.*, vol. 73, pp. 185–197, 2013.

Appendix

This Appendix gives technical information on how to manufacture 317.5mm (12.5") TBCs using an 18" mandrel for this project step by step with pictures. The material used for manufacturing are the ones introduced in section 3.2.1.

1. Cutting Braid sleeves into 15" pieces:
    a. mark the mandrel at 15".

    

    b. Pull the sleeving on the mandrel and stretch it as much as possible. Then, mark 15" by scissors.

    

    c. Take off the braid and then cut it.

    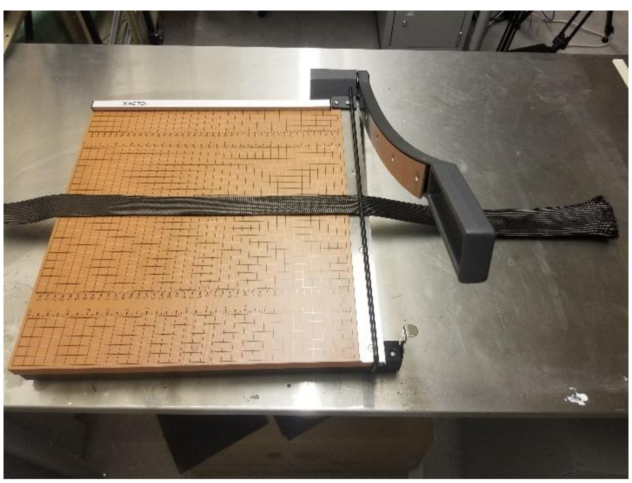

    d. Then the 15" preform ready.

    

2. Weigh the cut preforms (for volume fraction measurement).
3. Cut the release fabric to 14"×5.5" rectangles.
4. Wipe on the mold release onto the mandrels using a lint-free and let it dry. Do this step three times to make sure the mandrel is covered by mold release completely.

5. Cover the end of the mandrel using masking tapes: one inch on each end

6. Pull over the preform onto the mandrels. Place it in the middle of the mandrel (leave 1.5" from each end)
7. Attach ends of the sleeving by green tape. 0.5" of tape on the braid and 0.5inch of tape on the mandrel covered by tape. Cover the rest of the mandrel by another tape. There should not be any free surface on the mandrel.

8. Cover each end by 1" double-sided tapes at the position in the image below (from point 1inch to 2inch and 16inch to 17inch).

9. Mix 100 parts #2000 resin to 27 parts #2060 epoxy hardener by weight (or 3 by 1 by volume). After mixing for one minute, there are fifty-nine minutes left to apply the mixture to the braids. Sixty minutes after mixing resin and hardener, the mixture begins to gel and is useless.

10. Start messaging the resin on the preform until it gets completely wet. Apply the epoxy resin until the braid could not be able to absorb more. Saturate the braid by resin.


11. Take off the cover of two-sided tapes on both ends and rest the mandrel on a stand.

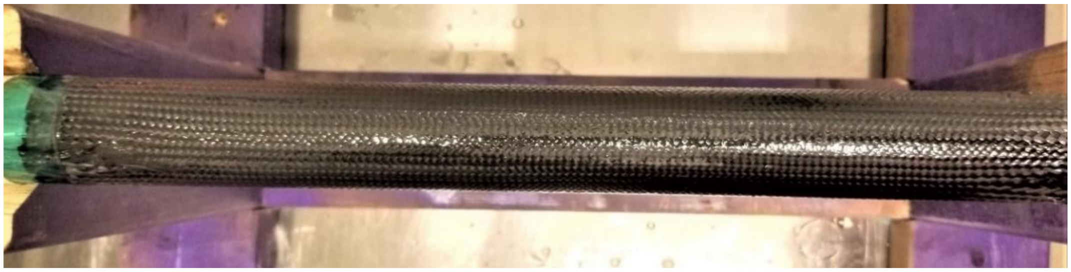

12. Wrap up the release fabric over the braid (make some holes on the fabric if the braid angles are going to be measured at the end).

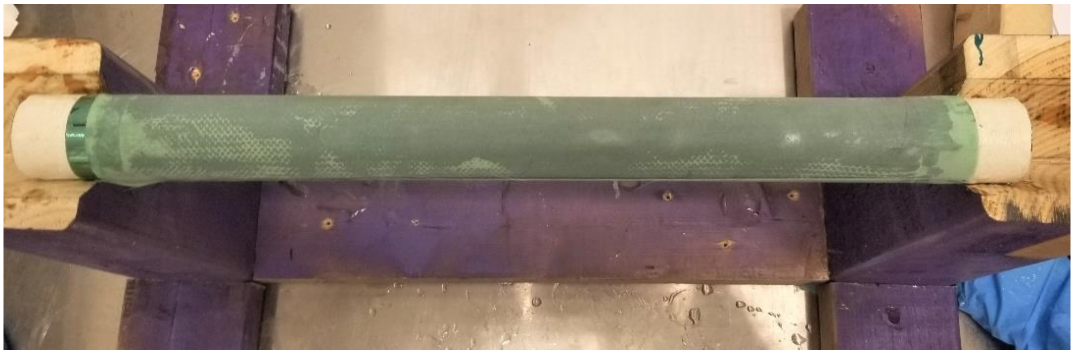

13. Wrap up the heat shrink in a spiral, overlapping it least ½ to ¾ the tape's width. Attach the beginning and end of the shrink tape to the two-sided tapes.

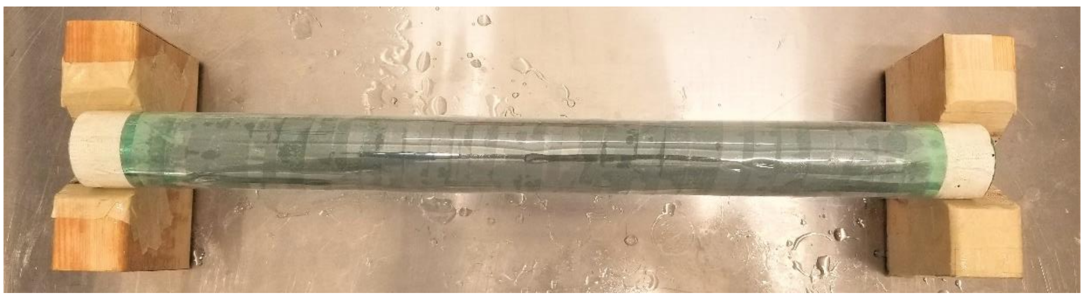

14. (Wear eye protection and thick gloves during this step) Have the mandrel vertically standing, use the heat gun to slowly heat the shrink tape, starting from top to bottom, rotating it for even heating until the tape has fully tightened. Do not hold the heat gun in one spot.

15. Apply heat until the excess resin squeezes out of the shrink tapes.

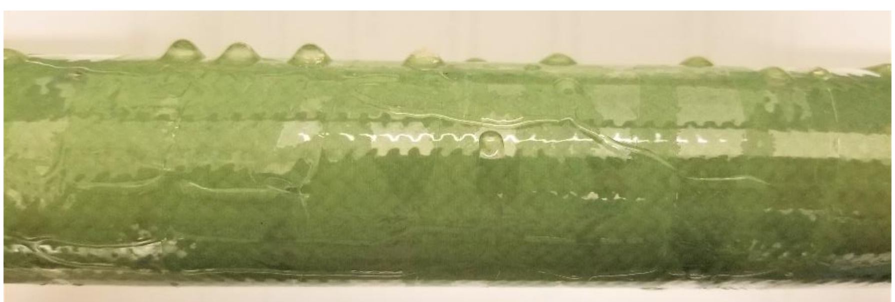

16. After about 24hours, the braids are thoroughly dried and ready to take off the mandrel. Use any necessary equipment to take of the braid, such as a hydraulic pump.
17. Weigh the manufactured braid after taking it off for future volume fraction measurements.